2017

Self-Assembled Architecture of Natural Organic Matter

Cynthia Johnson-Edler
South Dakota State University

SELF-ASSEMBLED ARCHITECTURE OF NATURAL ORGANIC MATTER

BY

CYNTHIA JOHNSON-EDLER

A dissertation submitted in partial fulfillment of the requirements for the

Doctor of Philosophy

Major in Chemistry

South Dakota State University

2017

SELF-ASSEMBLED ARCHITECTURE OF NATURAL ORGANIC MATTER

This dissertation is approved as a credible and independent investigation by a candidate for the Doctor of Philosophy in Chemistry degree and is acceptable for meeting the dissertation requirements for this degree. Acceptance of this does not imply that the conclusions reached by the candidate are necessarily the conclusions of the major department.

James A. Rice Date

Dissertation Advisor

Douglas Raynie Date

Department Head, Chemistry & Biochemistry

Kinchel Doerner Date

Dean, Graduate School

For Dave, Michael, Tye & Elias

ACKNOWLEGEDMENTS

I would like to acknowledge Dr. Jim Rice for all his counseling and guidance throughout the course of this investigation. I would also like to thank Dr. Moustafa Khalaf and Dennis Gibson for their untiring assistance with problem solving, collaboration in the laboratory, and most importantly their friendship. Thank you to Dr. Dan Olds at the Lujan Center for Neutron Research at the Los Alamos National Laboratory, and Dr. William Heller at the Spallation Neutron Source at Oak Ridge National Laboratory, for all their assistance with neutron data analysis and interpretation. I would also like to acknowledge the U.S. Department of Education Graduate Assistance in Areas of National Need (GAANN) and the National Science Foundation (NSF) Grant number 1012648 for partial funding of the research contained herein.

TABLE OF CONTENTS

LIST OF FIGURES

APPENDIX FIGURES LIST

LIST OF TABLES

ABSTRACT

SELF-ASSEMBLED ARCHITECTURE OF NATURAL ORGANIC MATTER

CYNTHIA JOHNSON-EDLER

2017

This investigation focuses on the determination of the architecture of the natural organic matter (NOM) contained within a soft coal-like material, an agricultural soil and a peat material. NOM has been extracted from bulk materials, fractionated, reassembled, then characterized by ^{13}C Solid State NMR, Pulsed-Field Gradient NMR (PFG-NMR), and Small Angle Neutron Scattering (SANS). Interpretation of the data obtained by SANS has established that the majority of the components of NOM are mass fractals in solution and surface fractals in the solid state. Surface-to-volume ratios calculated with PFG-NMR data indicate the NOM components studied have varying disk-like shapes. These components self-assemble to form somewhat spherical assemblies that are more space filling but still retain their mass fractal characteristics. ^{13}C Solid State and PFG-NMR gave evidence that aromaticity increases from the fractionated components that comprise NOM to the final assembly which also includes carbon types containing polar functional groups and aliphatics. It was also determined that NOM shares numerous similarities with asphaltenes and resins extracted from petroleum. The similarities include a hierarchical self-assembly of components with distinctly different chemical characteristics, comparable fractal dimension values, surface-to-volume ratios, and differences in diffusion coefficients dependent upon component.

The model proposed by these findings suggests that the self-assembled architecture of NOM is dependent upon a polyaromatic hydrocarbon ring system with polar functional groups and peripheral alkanes. This architecture is consistent for the three materials studied, indicating that the amount of organic carbon present in a material or the materials geographic origin does not affect how NOM self-assembles in the environment. This assembly is created by a composite consisting of two lower level components, one of which is primarily a lipid and the other is an amphiphile. This composite then interacts with a large upper level component comprised mainly of aromatics with a few aliphatic and polar functional groups. Experimental data suggests that the composite component inserts into the aromatic ring system of the larger component then chemical interactions occurring between the two components causes the final assembly to be smaller than the components from which it is comprised. It is further suggested that this decrease in size is due to functional groups that tend to associate through short range inter/intra-molecular interactions such as van der Waals, π-π interactions, and hydrogen bonding which pull the molecules of the components into closer proximity to one another. Therefore, the proposed model herein is an example of a hierarchical aggregation occurring between distinct components of NOM which retain their similar chemical and physical characteristics regardless of material type.

Chapter 1

INTRODUCTION

1.1 NATURAL ORGANIC MATTER AND CLIMATE CHANGE

This study focuses on the components of Natural Organic Matter (NOM) and how they interact. NOM consists of humic substances and organic molecules that belong to recognizable compound classes (e.g., lipids, carbohydrates, proteins, etc.) found in the soils, water, and sediments of the Earth's surface.[1] These materials are the products mainly arising from; the partial degradation of plant material, biomass from microorganisms, coatings on mineral grains, pyrolytic carbon, organic precipitates, and dissolved organic material in soil water.[2-4,5,6] NOM is defined as naturally occurring biogenic,[7] heterogeneous organic substances that can be characterized as being high molecular weight, refractory, and yellow to black in color. [8] The heterogeneity of this substance enables it to be classified as a mixture that is operationally defined into three distinct fractions (humin, humic acid, and fulvic acid)[9] based on their solubility in aqueous solutions.[8] Humin is insoluble in aqueous solution at any pH; humic acid is soluble in alkaline aqueous solutions but precipitates at or below approximately pH 2; and fulvic acid is soluble at any pH in aqueous solution.

Natural organic matter ultimately is transformed into hydrocarbon fossil fuels through the physiochemical processes of diagenesis, catagenesis, and metagenesis.[10] NOM as discussed here exists in the early stages of diagenesis, a process that begins transforming

organic matter from biological tissue to prepare it for burial and transfer to the geological portion of the carbon cycle.[7] Diagenesis refers to processes that are occurring under relatively low temperature and pressure. A major agent of transformation during early diagenesis is microbial activity.[10] The energy required for this activity is provided by the organic material and produces CO_2, methane, and water.[10] Biopolymers (proteins, carbohydrates) are subjected to microbial decomposition and condensation during this process causing the loss of superficial hydrophilic functional groups (OH & COOH) causing an increase in insolubility. With increased depth and pressure a humin-like material results and continues to undergo condensation and defunctionalization creating newly polycondensed geopolymers which are precursors to kerogen[10] which then continues the transformation toward liquid petroleum and then "wet gas" both of these are accompanied by the production of methane.[10]

The NOM within this diagenetic process constitutes more than four times as much organic carbon as found in the biosphere.[11] As stated, during this natural degradation process NOM releases, methane and CO_2 into the atmosphere. The amount produced is an order of magnitude larger than anthropogenic emissions.[12,13] Consequently, this dictates that NOM has a significant impact on the modulation of the temperature of the Earth's surface.[14,8,15] It has been shown that increasing this pool of carbon improves soil fertility and reduces the amount of anthropogenic CO_2 that is released to the atmosphere.[16] Therefore, the active sequestration of carbon in the soil may be a method to slow the effects of climate change resulting from the burning of fossil fuels and natural

plant biomass degradation. Although these substances represent the bulk of the organic carbon in the global carbon cycle, and perform essential ecological functions[1,17,18] (i.e.

transport and fate of contaminants, metal-binding, water holding capacities, and the stability of soil particle aggregates) the heterogeneity of these materials regardless of the bulk source material from which they originate, makes it difficult to understand why they exhibit such similar efficiencies performing the previously mentioned ecological functions. It is this innate heterogeneity that triggers the interest in the architectural organization of this mixture. Understanding the architecture of NOM may further insights into how its chemical properties may be used to increase carbon residence time within soils. The ability to increase the residence time of carbon in the soil has the potential to affect the Earth's temperature, which in turn will reduce the effects of global climate change.

1.2 CLIMATE CHANGE

The Intergovernmental Panel on Climate Change (IPC) has stated "scientific evidence for warming of the climate is unequivocal".[19] According to Petit[20] and the National Oceanic and Atmospheric Association (NOAA)[21] the level of atmospheric carbon dioxide (CO_2) has cycled from approximately 175-300 ppm for the previous 400,000 years, except for approximately the last 130 years. The historical changes in the levels of CO_2 emitted are attributed to natural climate forcings which include small variations in the shape of the Earth's orbit and its axis rotation (Milankovitch cycles) which occur over thousands of years, a change in the sun's brightness, and large volcanic events that release light-threshold previous held for four hundred millennia. According to data collected by the

Mauna Loa Observatory[22] the CO_2 annually emitted has risen from 0.54 ppm/year in 1959 to 3.05 ppm/year in 2015. The extreme increase in the annual growth rate of CO_2 reflecting particles into the stratosphere.[23] The onset of the industrial revolution in the late 19th century increased the amount of CO_2 emitted from human induced anthropogenic sources causing the levels in the atmosphere to break the 300 ppm over such a short span of time is unprecedented and appears to be directly related to human activity. These anthropogenic forcings are caused by particle pollution (aerosols), which absorb and reflect sunlight, deforestation decreases uptake of CO_2 by vegetation which alters how the Earth's surface reflects and absorbs sunlight, and the rising concentration of atmospheric CO_2 and other greenhouse gases which decreases the planet's ability to radiate heat to space.[23] All of these natural and anthropogenic forcings change the amount of solar energy the planet receives and releases.[19] More specifically, CO_2 causes the Earth's energy budget to careen out of balance by absorbing thermal infrared energy radiated from the surface rather than allowing it to escape into space. This occurs because CO_2 absorbs radiation in the region of the energy spectrum were other gases such as water vapor do not. Water vapor absorbs many wavelength of infrared energy and is almost transparent to others. It is this transparency that leaves a "window" for the atmosphere to cool the Earth's surface. One of these water vapor windows occurs between 8-14 micrometers.[23] and CO_2 is a strong absorber of thermal infrared energy from 12-18 micrometers.[24] Although this window is very small the thermal energy is century partially closes one of the Earth's atmospheric windows. This partial closure causes the Earth to retain more thermal energy than it releases, and over time results in an

increase in average global surface temperatures. Surface temperature reconstructions absorbed by these gases it is then re-emitted in all directions, so roughly half of the energy absorbed is trapped and travels back to the Earth's surface[7]. This means that the increase in atmospheric CO_2 that has been occurring over a little more than the last have shown that the Earth has warmed since 1880[25] with most of this occurring since the 1970's. Although the early part of this century saw a decline in the solar output of the sun, surface temperatures continue to rise.[26] More alarmingly, the 20 warmest years have occurred since 1981, with all 10 of the hottest years taking place within the last 12 years.[27] The ocean does have the ability to absorb the additional thermal energy which makes the onset of the effects of climate change occur gradually, however the ocean cannot stop a change from occurring.[28] If the concentration of greenhouse gases stabilizes then the Earth's climate will equilibrate, although the average temperature will still be higher than before the Industrial Revolution.

The effects of climate change have become startling in recent decades. As previously mentioned the ocean absorbs a vast amount of the excess radiation that has been trapped by the increase in CO_2. In fact, the acidity of the oceans waters that results from the absorption of atmospheric CO_2 has increased by ~ 30% since the beginning of the Industrial Revolution.[29,30] The additional CO_2 has increased the temperature of the top 700 meters of ocean an average of 0.168 °C since 1969. This increase in ocean temperatures and the rise in atmospheric temperatures has caused the decline in the extent and thickness of Artic sea ice,[31] the Greenland and Antarctic ice sheets to shrink,[32] and glaciers to retreat all over the world.[33] The combination of these things has caused global sea levels to rise ~ 17 cm in the last century.[34] More compelling is the fact that the rate in

the sea level rise in the last decade is double that of the last century.[34] The change in the Earth's climate has also influenced the weather around the globe, with number of record high temperature, rain fall, and extreme weather events like tornados and hurricanes steadily increasing since 1950.[35]

While the ocean has the capacity to absorb excess CO_2 the negative effects of this absorption are plain to see. For this reason, investigations into using the soil to store carbon (what has become known as "carbon sequestration") are vital to try and minimize the effects of the rapid increase in CO_2 levels in the atmosphere. The methods for sequestering atmospheric CO_2 fall into two major categories: abiotic and biotic. Abiotic sequestration is based on physical and chemical reactions and engineering techniques that do not the interaction of living organisms like plants or microbes. These methods have a large capacity for carbon sequestration, but are expensive and have the possibility of CO_2 leakage back into the atmosphere. In contrast, biotic sequestration is more cost effective but has a limited capacity to retain carbon in the soil. The ability to understand the most basic chemical interactions that are occurring in the soil, more specifically the mechanisms that produce NOM in the soil, will allow the development of methods to increase the soil's ability to sequester carbon.

1.3 HISTORICAL MODELS OF NOM

It is understood that NOM is the by-product created from the degradation of plant and microbial tissue in the environment.[9] For many years NOM was thought to consist of a discreet material, such as a polymer.[36,9] However, more recent research has indicated that while it might contain polymeric or macromolecular material, it is much more complex than has been previously understood. This progression of research has led to the development of two types of models: (1) the polymer models and then to (2) the molecular aggregate models. The polymer models arise from the belief that the components of NOM are the products of secondary synthesis reactions from the degradation products and are deemed as being polymeric species with chemical characteristics distinctly different from the starting material[36] resulting in mixtures of highly cross-linked polymers of differing molecular weights. This lead to the belief in the possibility that the structure of the three humic substances (humin, humic acid, and fulvic acid) could be generalized by a classical structural diagram of covalently bonded functional groups similar to the represented chemical structure of lignin. The solubility differences seen in the different humic substances would then be the result of varying molecular weight and charge densities. In contrast, the molecular aggregate models stem from the inclusion of partially degraded products of plant polymers and remnants of microbial components held together by non-covalent bonds.[37,38] The debate between these two types of models has somewhat waned in recent years with most researchers

agreeing that the heterogeneity consistently demonstrated by the materials does not support polymer models due to the lack of a common "building block" conformation required for such molecules.

In addition to the general movement toward the molecular aggregate models the latest research has shown that NOM is a self-assembling material comprised of components of differing chemical composition.[39] These components include humic acid (HA_0), a highly aromatic non-amphiphilic component (HA_1), a lipid-like component (L_1), and an amphiphilic component (HA_2) that self-assemble via a hierarchical aggregation process.[39] This self-assembly process is related to the affinities of certain functional groups of the components of the humic materials themselves. These functional groups tend to associate through inter/intra-molecular interactions[40] which reinforces the probability that the molecular aggregation model is an adequate representation of what may be occurring in the environment.

Studies have shown that NOM is a mixture of a limited number of chemically distinct components of relatively low molecular weight that aggregate in solution.[41,42] Wershaw proposed that these substances consist of a hierarchy of structural elements[43] wherein the lowest level components are phenols, quinoid, and benzene carboxylic acid groups linked together with covalent bonds to form small particles with molecular weights of a few thousand or less. Wershaw also proposed that higher level NOM components consist of aggregates of amphiphiles with acidic functionality intrinsically stabilized by

non-covalent weak forces such as dispersive hydrophobic interactions (e.g. van der Waals, π-π and CH-π bonding) and hydrogen bonds.[44,45] This is attributed to the fact that the fractionation procedure applied to soil NOM (described in Chapter 2.2) does not disrupt covalent bonds, (i.e. carbon-carbon, ether, and ester) meaning NOM must self-assemble via bonds that are relatively weak.[44] Accordingly, the strength of these interactions is dependent upon the types of functional groups found within the assembly. The non-covalent aggregation of these small particles occurs as a function of pH to form the higher level assemblies and is also dependent upon oxidation state of the lower level components and metal ions present within the system.[43] Strong associations are formed in the environment due to the hydrophobic effect[46] which has been shown to induce aggregation on mineral surfaces and in solution.[47] Some methods employed to explore the presence of hydrophobic domains within NOM include fluorescence quenching using naphthalene, which demonstrated the presence of hydrophobic domains within humic acid.[48] Similarly, the diffusion of dichloromethane into NOM showed micro-regions of differing polarity.[49] The existence of hydrophobic domains was also illustrated by ^{19}F NMR by measuring the relaxation rate of atrazine in a 10% humic acid solution using both hydrophobic and hydrophilic paramagnetic probes.[50] ^{19}F was also used to investigate the sorptive uptake of hexafluorobenzene onto whole and lipid extracted peat soils. This study demonstrated that the sorption of hexafluorobenzene was rapid and directly proportional to lipid content.[51] Many other methods; adsorption isotherms,[52] ^{13}C and wide-angle x-ray scattering (WAXS)[53] have been used to demonstrate the presence of

hydrophobic domains in NOM in association with one another further supporting a model of aggregation of smaller molecules containing varying functional groups.

The depolymerization and oxidation reactions that occur during the enzymatic degradation of the biopolymers mentioned in Chapter 1.2 has been shown to produce amphiphiles.[37] As such, they will spontaneously aggregate in the most thermodynamically stable configuration in aqueous systems with the hydrophilic portion in contact with the water phase or polar groups on the surfaces of minerals, and the hydrophobic portion towards the interior of the assembly away from the aqueous phase.[54] These ordered aggregates then self-assemble[39] and constitute the humus in soils and sediments.[37] In general, amphiphilic aggregates have been shown to exist as micelles, bilayer membranes, liquid crystals, and vesicles. [55,56] Guetzloff and Rice[57] demonstrated that humic acid forms micelles in alkaline aqueous solutions at concentrations above 7.2 g/L, and Wershaw[37] stated "In soils and sediments, humus ordered aggregates most likely exist as bilayer membranes coating mineral grains and as micelles in solution."

The study of biological membranes has led to the majority of information gathered regarding the characteristics of membranes, micelles and other ordered structures comprised of amphiphiles. Tanford[46] has shown that when certain lipids are present in aqueous solution bilayer membranes form spontaneously. However, lipids are not the only type of material that may exist in the interior of a micelle or a membrane. The hydrophobic interior may consist of structures possessing functional groups that hydrogen bond to other polar groups to form hydrophobic aggregates.[56]

For example, Mazer et al. demonstrated that sterol portions of bile salts can enter the interior of bile salt-lipid micelles by aggregation due to the formation of hydrogen bonds.[58]

Multi-component systems have shown that membranes and micelles also form when more than one type of amphiphile is present within a system.[59] Due to the polydispersity of NOM the presence of more than one type of amphiphile is highly likely. However, it is also possible that aggregation is occurring due to hydrogen bonding of polar groups (hydroxyls) that are evenly spaced along partially degraded carbohydrate components of plant tissue. Plant pectins and gums form gels in this way.[60] Tannins have been shown to hydrogen bond with proteins, uronic acids, pectin, hemicellulose, and cellulose.[61,62] This gives the possibility of geometries other than spherical micelles (cylindrical, ellipsoidal etc.) if more than one component is present within an assembly.

The existence of amphiphiles and components that contain hydroxyls is well documented in NOM. It has also been determined that humic acid forms micelles and other complex aggregates, however the hierarchy that exists in these systems begins at a lower level than that of complex membranes and micelles. As stated before lower level components of these systems are phenols, quinoid, and benzene carboxylic acid groups linked together with covalent bonds to form small particles with molecular weights of a few thousand or less.[43] Although it has been shown that humic acid self-assembles, neither the interactions and conditions that drive this self-assembly nor the architecture of the

assemblies have been determined. Consequently, the need to look at yet another model becomes necessary.

1.4 ASPHALTENES AND RESINS

Natural organic matter is a precursor to humic coals[7] which are formed through the process of peatification followed by coalification, that is divided into biochemical and a geochemical stages. The main activities during peatification are biological and are synonymous with the process of diagenesis described in Chapter 1.2. The early stages of coalification are also biological with the further loss of oxygen containing functional groups, causing a concentration of carbon and hydrogen. The final organic rich products of the early stages of coalification are referred to as brown coal (sub-bituminous) which have no carbohydrates and contain 50-70% carbon and 5-7% hydrogen.[7] Biological activities cease in the later stages of coalification and the transformations occurring therein are generated by increases in temperature and somewhat in pressure, which can be equated with catagenesis.[7] Sub-bituminous coal is then transformed into high-volatile bituminous coal (commonly called a hard coal) by a further reduction in oxygen content that does not affect the aryl oxygen content, suggesting the condensation of phenols to aryl esters or dibenzofuran-like structures.[63] During this time structural aromaticity increases,[64] and significant decarboxylation occurs.[65] The boundary between brown and hard coals can be approximated as the diagenetic/catagenetic boundary.[7]

Diagenesis of organic plant material gives rise to NOM which in time becomes coal.

Similarly, the same processes occur in the environment with petroleum based products. Petroleum describes naturally occurring liquid (i.e. oil) and gaseous hydrocarbon deposits. [7] Bitumen is a term applied to naturally occurring solid or liquid hydrocarbon deposits and exhibits some characteristic synonymous with NOM. This material has been extensively studied by the fossil fuel industry in an attempt to understand the components of which it is comprised. The components of bitumen (asphaltenes, resins, and hydrocarbons) like NOM are operational defined by their solubility. While the components of NOM are defined by their solubility in aqueous solvents as a function of pH, asphaltenes and resins are soluble in organic solvents as a function of aromatic/aliphatic nature of the solvent system. Asphaltenes are highly aromatic with aliphatic and acyclic substituents and are soluble in aromatic organic solvents like toluene, but precipitate in aliphatic solvents. Whereas resins are hydrocarbon chains which are soluble in solvents such as *n*-heptane. Asphaltenes, similar to NOM, have an innate ability to self-assemble.[66,67,68] They have been the focus of countless studies in the petroleum industry because of their negative impact on the exploration, production, and refining of oil. In exploration they may alter the flow phase of a reservoir; in production they may plug the wellbore; in transportation they may precipitate, and eventually clog pipelines; in refining they decrease final yields.[69] For these reasons they have been studied in an effort to determine their structure and method of self-assembly. Again, like NOM many models have been proposed to determine the conditions required for self-assembly to take place in order to mitigate the negative impacts seen by the

petroleum industry. One of these is the Yen-Mullins model[70,71] also known as the modified Yen model. Yen[72] provided a hierarchical picture of asphaltenes then relates that hierarchy to self-assembling components of differing length scales.[73] This model has been further modified by Mullins[70] and focuses on an asphaltenes architecture consisting of a single, moderately large polyaromatic hydrocarbon ring system with peripheral alkanes which forms nanoaggregates with aggregations numbers of approximately six. The interior consists of a single disordered stack surrounded with peripheral alkanes. These nanoaggregates then form clusters with aggregations numbers of approximately eight.

Natural organic matter and bitumen are naturally occurring materials created through the geochemical processes of the Earth. Both comprise components that are operational defined by their solubility characteristics. In addition, these materials form aggregates through self-assembly, therefore, it is reasonable to conceive that the self-assembled architecture of these two materials may indeed be similar.

1.5 HYPOTHESIS

NOM consists of composites that have a defined structural architecture that is independent of source material type.

This dissertation focuses on the inter-/intra-molecular interactions that drive the self-assembly process of the humic acid component of NOM to develop an architectural model of the humic acid assembly for three NOM source material types. More specifically this will be assessed by:

1. Pulsed Field Gradient (PFG) NMR
    a. Determination of diffusion coefficients will determine the relative size of the components of interest.
    b. Changes in the chemical shifts seen in fractionated components when compared to the final authentic and methylated HA_0 and L_0 will provide information regarding the intra/inter-molecular interactions occurring during self-assembly.
2. Small Angle Neutron Scattering (SANS)
    a. Determination of fractal dimension will provide insight into the space-filling characteristics of the components and assemblies
    b. Form factor analysis will give approximate shape for each component and the final assembled HA_0.
3. A model of the architecture of NOM will be proposed by applying the above findings.

The dissertation has 6 chapters. Chapter 2 is a detailed account of the extraction and analytical methods used for NOM materials studied. Chapter 3 contains bulk sample characterization results and Chapter 4 contains a description of the determinations of diffusion coefficients and an interpretation of chemical shift data obtained by pulsed field gradient NMR. Chapter 5 provides information concerning fractal dimension, and form factors calculated using SANS. Chapter 6 proposes an architectural model developed and conclusions reached by analysis of all data obtained and speculates upon future work.

Chapter 2

Materials and Methods

2.1 DESCRIPTION OF BULK NOM SOURCE MATERIALS

Humic acid (HA_0) was isolated from the International Humic Substances Society Leonardite (BS104L), Elliott Silt Loam soil (BS102M), and Pahokee Peat (BS103P) bulk reference materials using a traditional alkaline extraction method.[36] The IHSS Leonardite is produced by the natural oxidation of exposed lignite. It is a low grade coal collected from the Gascoyne Mine in Bowman County, North Dakota.[74] This material was chosen due to its distinct carbon-type distribution that consists of primarily aliphatic (0-50 ppm) and aromatic (108-150) carbon types.[75] Elliott Silt Loam soil is typical of the fertile prairie soils found in the United States. It consists of very deep somewhat poorly drained soils on moraines and till plains. This material was obtained from an undisturbed area on the grounds of the Joliet Army Ammunition Plant near Joliet, Illinois.[74] Pahokee peat is a typical agricultural peat soil found in the Florida Everglades. It forms from the organic deposits of fresh water marshes and consists of poorly drained soils that are 36-51 inches thick over limestone. This material was obtained from the University of Florida Belle Glade Research Station.[74] Elliott Silt Loam soil and Pahokee peat were chosen because they have a carbon-type distribution consisting of aliphatic, O-alkyl (50-100 ppm), aromatic and carboxylic resonances (160-190 ppm).[76,75]

2.2 FRACTIONATION METHODS

Bulk materials are extracted using the traditional alkaline extraction method.[36] Which

requires stirring/shaking the bulk material for 24 hours with 0.5 M NaOH. Samples are then centrifuged and the supernatant is acidified with HCl to precipitate the humic acid. Another centrifugation separates the humic acid and fulvic acid supernatant. The supernatant containing the fulvic acid is discarded while the precipitated humic acid is dried. The samples without additional extraction are referred to as HA_0. A portion of each dried HA_0 sample is then further extracted using the fractionation method shown in Figure 2.[77]

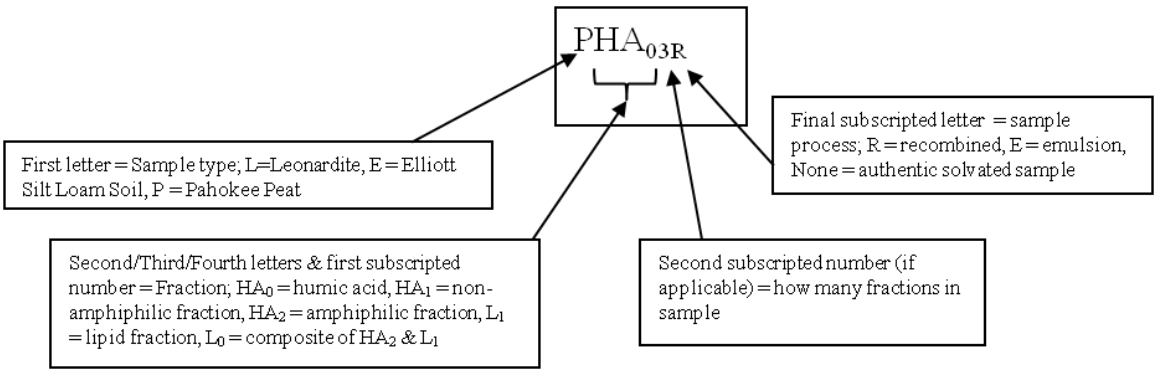

Figure 1. Sample description legend

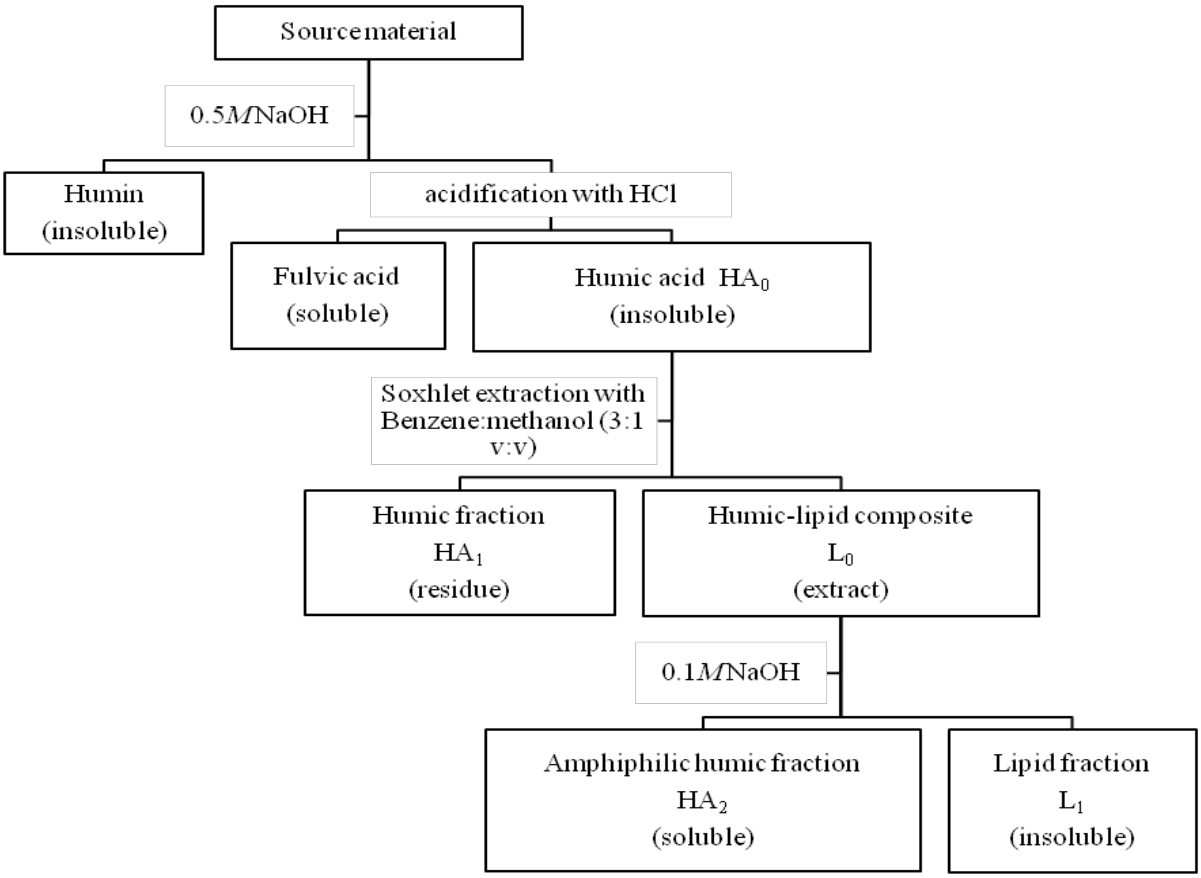

Figure 2. Representation of extraction methods used to fractionate HA_0 into its components (HA_1, HA_2, L_0, and L_1) from all samples materials studied. Adapted from Khalaf *et al. Soil Biol. & Biochem* **2014**, 73, 96-105.

The lipid-like composite L_0 and a humic-like component HA_1 were obtained from HA_0 by Soxhlet extraction using a benzene:methanol azeotrope (3:1 v/v).[77] The ratio of HA_1:L_0 which comprised the HA_0 assembly varies dependent upon the material type, with the distributions of these components for Leonardite, Elliott Silt Loam, and Pahokee peat being 70:30, 90:10, and 80:20 (weight%), respectively. The L_0 component is a composite that can be further fractionated into HA_2 and L_1 using an additional alkaline extraction step.[77] The ratios of HA_2:L_1 from this fractionation are 70:30, 70:30, and 65:35 (weight %), for Leonardite, Elliott Silt loam, and Pahokee peat, respectively.

2.3 CATION EXCHANGE OF HUMIC ACID-LIKE FRACTIONS

The HA_0, HA_1, and HA_2 components of each material type were converted to the hydrogen form via cation exchange using Dowex® 50W-X H+ 20-50 mesh resin to ensure metals which may interfere with NMR had been removed from samples. Humic acid like samples (HA_0, HA_1 & HA_2 of all three materials; ~ 0.1 g) were dissolved in 100 mL of NaOH (0.1 M). A solution of 6 M HCl is passed through the column followed by distilled water until effluent pH ~ 6 - 7. The sample is then passed through the column followed again by distilled water. The pH of the effluent is monitored to determine the sample cutoff point. Once the effluent again reaches a pH of ~ 6 - 7 the sample is then dried and weighed to determine recovery. The column is regenerated by passing 6M HCl through prior to introducing the next sample.

2.4 TOTAL ORGANIC CARBON (TOC)

The total organic carbon mass balance was determined using a Shimadzu TOC-VSCN total organic carbon analyzer with a SSM-5000 Solid Sampling Module. This instrument catalytically oxidizes organic matter under a flow of CO_2-free air then detects the amount of CO_2 produced via infrared adsorption. The mass balance data will be used to calculate the abundance of each fraction in the starting material. This information is necessary in order to prepare mixtures of the fractionated materials to be reassembled that accurately represent the same chemical composition of the authentic materials found in the environment.

Table 1. Total organic carbon mass balance percentages for individual components of materials studied

	TOC%		TOC%		TOC%
Leonardite		**Elliott Silt Loam Soil**		**Pahokee peat**	
***HA_0**	56.0	***HA_0**	48.5	***HA_0**	50.8
HA_1	58.5	**HA_1**	73.6	**HA_1**	75.0
HA_2	12.4	**HA_2**	6.3	**HA_2**	6.1
L_0	22.8	**L_0**	18.1	**L_0**	17.5
L_1	6.1	**L_1**	2.3	**L_1**	0.42

***** The HA_0 values are only the experimentally TOC values. The values for the remaining components are the TOC mass balance for the materials studied.

2.5 PULSED FIELD GRADIENT (PFG)-NMR

Diffusion coefficients (D) acquired by PFG-NMR use a pulse gradient which allows the movement of molecules to be spatially measured due to the motion of a molecule being

affected by its nearest neighbors.[78] This allows the determination of D values that provide information regarding the inter-/intra-molecular interactions of a multi-component system. Translational diffusion is especially important when studying molecular interactions because reacting species must collide before they can interact.[79] PFG-NMR determines the D values by measuring the attenuation of a signal resulting from the de-phasing of nuclear spins due to the combination of the translational motion of the spins of the molecules and the application of well-defined gradient pulses.[80] The NMR signal intensity (*I*) is attenuated depending upon the diffusion time, gradient strength, and pulse length. The impact of these variables on ***I*** is described by

$$I = I_0 \; e^{-D\gamma^2 g^2 \delta^2 (\Delta - \partial|3)} \qquad (1)$$

where ***I*** is the observed intensity, $\boldsymbol{I_0}$ is the reference intensity (unattenuated signal intensity), **D** is the diffusion coefficient, $\boldsymbol{\gamma}$ is the gyromagnetic ratio of the observed nucleus, ***g*** is the gradient strength, $\boldsymbol{\delta}$ is the length of the gradient pulse and $\boldsymbol{\Delta}$ is the diffusion time.

All samples were dissolved in either D_2O or D_6-benzene: D_4-methanol (3:1 v/v) to a concentration of 4 g/L and then filtered using a Whatman® 0.45µm Glass Microfiber Filter (GMF) to ensure undissolved particles which may interfere with the NMR analysis had been removed. Deuterated NMR solvents D_2O (99.8% D), CD_3OD (99.6 % D), and NaOD (40% wt solution in D_2O, 99+ atom % D) were purchased from Acros Organics,

C_6D_6 (99.96 % D), KOH (≥ 85%), diethyl ether (≥ 99.7%) , absolute ethanol (200 proof), and DIAZALD® used for methylation of HA_0 and L_0 fractions using an established procedure[81] described in Chapter 2.4.1 were purchased from Sigma Aldrich. All NMR solvents were used as received.

Solution-state ^1H NMR spectra were collected using a Bruker Avance 600 MHz NMR spectrometer with a 5-mm inverse ^1H-^{13}C-^{15}N TXI probe using 16 scans and a delay of 2 seconds between pulses. PFG-NMR data were obtained at 295 K using a Bipolar-Pulse Pair Longitudinal-Eddy-current -Delay (BPPLED) sequence from the standard Bruker library.[82] Scans (512-2000 depending on the signal to noise of the sample) were collected using 1.75 - 2.25 msec sine-shaped gradient pulses (3.5 - 4.5 msec per bipolar pulse pair) in 24 increments from ~7-330 $mT \cdot m^{-1}$ with a diffusion time range of 75-180 msec at 295 K. The diffusion time and gradient length where optimized to achieve 95% suppression of the attenuated signal at the maximum gradient strength. Suppression of the D_2O signal was used for samples dissolved in D_2O in combination with the BPPLED pulse sequence and power levels were optimize for maximum suppression of the solvent. Diffusion coefficients were evaluated using the T_1/T_2 relaxation software included the standard Bruker TopSpin® software package. Diffusion-ordered spectroscopy (DOSY) spectra were then generated to directly correlate the diffusion coefficients to the proton chemical shift in a two-dimensional plot.

2.5.1 METHYLATION OF HA_0 AND L_0 FRACTIONS

Samples were methylated using diazomethane. Diazomethane potassium hydroxide (0.4 g) was dissolved in 0.8 mL of ultrapure water, and then mixed with 2.5 mL of absolute ethanol in a glass reaction vessel with constant stirring (at ~ 40ºC) of a Sigma Aldrich DIAZALD® Kit. N-Methyl-N-nitroso-p-toluenesulfonamide, (DIAZALD®; 2 g for HA_0's and 4 g for L0's) was dissolved in 20 mL of diethyl ether (99.7%) and added drop wise to the reaction vessel. Yellow diazomethane gas was then condensed and collected in a receiving round bottom flask with stirring that contains the sample to be methylated. Methylation continued until the solvents in reaction vessel were colorless, indicating the complete transformation of DIAZALD® into diazomethane gas. Methylated samples were then stirred overnight and dried for seven days to ensure complete solvent evaporation.

2.6 SMALL-ANGLE NEUTRON SCATTERING

Small-angle neutron scattering (SANS) measurements were performed at Oak Ridge National Laboratory's (ORNL) Spallation Neutron Source (SNS) beam line 6 Extended Q-Range Small-Angle Neutron Scattering Diffractometer (EQ-SANS), and the contrast match experiments were carried out on the Low-Q Diffractometer (LQD) at the Lujan Center at the **L**os **A**lamos **N**eutron **S**cience **CE**nter (LANSCE) in Los Alamos NM, which is part of the **L**os **A**lamos **N**ational **L**aboratory (LANL). Both accelerators operate in time of flight mode receiving neutrons from a spallation target using mercury[83] and tungsten targets,[84] respectively.

SANS experiments measure the intensity of scattering in terms of the coherent macroscopic scattering cross section ($d\Sigma/d\Omega$) as a function of the scattering vector (*q)*

$$q = \frac{4\pi}{\lambda}\sin\frac{\theta}{2} \qquad (2)$$

where λ is the wavelength of the incident radiation and the θ is the scattering angle. The scattering cross section of polydisperse anisotropic particles can be described by the "decoupling approximation"[85,86]

$$\frac{d\Sigma}{d\Omega}(q) = I_{(q)} = N_p P^2_{(q)} S_{(q)} \qquad (3)$$

Where N_p is the average number density of scattering particles and may also be written as Φ/V_p, where V_p is the average volume of one particle and Φ is the volume fraction.

$P^2_{(q)}$ includes the form factor, $F_{(q)}$, describing the architecture of the particles which includes the shape, size, and polydispersity, and the contrast term $\Delta\rho$.[2] The contrast term $\Delta\rho^2$ includes ρ and ρ_0 which are the scattering length densities of the particles and the solvent, respectively. $S_{(q)}$ is the structure factor which gives information regarding interactions between particles assuming size and orientation are uncorrelated with the position of the particles.[85] For dilute systems the Guinier region (at scales larger than the typical size of the particles) interactions are very short range and the S(q) is equal to unity.[87] Consequently for a two component system like most for those studied herein the expression becomes

$$I(q) = \Phi(1-\Phi)\Delta^2 V_p P(q) S(q) \qquad (4)$$

Further examination of the scattering intensity distribution function is the application of an approximation for particle size and shape characterization. The P(q) can be approximated by the radius of gyration (R_g) using a Guinier plot, which gives

$$I(q) = I_o e^{-q^2 \frac{Rg^2}{3}} \qquad (5)$$

equation 5 is used to plot the logarithm of I(q) versus q^2 to obtain the radius of gyration, which is essentially the size of the particle of interest, but more specifically it is the distribution of the mass of an object around an axis. Although a Guinier plot can be used to evaluate the R_g value it does not however supply any information regarding particle shape. Therefore, the presumption of a specific particle shape is hard to establish in order to fit the scattering data to any specific model. Because of their fractal nature, determination of the fractal dimension (***D***) for all components must occur early in the data analysis process. The power law exponent of the slope of a plot of ***I(q)*** versus ***q*** conveniently gives the fractal dimension of a particle. Once the ***D*** value is established the R_g and ***D*** values are used to calculate surface-to-volume (S/V) ratios to ascertain a general shape for the particles of interest.

2.6.1 CONTRAST MATCHING SAMPLE PREPARATION

Prior to conducting any scattering analysis contrast matching of the particles in hydrogenated/deuterated solvents must be completed. This involves the manipulation of the hydrogenated/deuterated solvent ratios to match the scattering length density of one component in a multi-component system which ultimately causes the matched component

of the system to disappear. This allows the investigation of a specific component without interference from other components within the system. The scattering length densities of hydrogen (pH = -0.374 x 10^{-12} cm) and deuterium (pD = 0.667 x10^{-12} cm) are vastly different which allows changes in the hydrogen:deuterium ratio to be easily observed and contrast match information to be acquired. Authentic Leonardite HA_2, L_1, and authentic and emulsified L_0 fractions were dissolved in benzene:methanol (3:1, v:v) with varying total hydrogen:deuterium (H:D) ratios to determine contrast match values. Sample composition and hydrogen:deuterium ratios are given in Table 1. Emulsions containing HA_2, L_1 to produce L_0 were prepared using a procedure developed by Chilom *et al*.[88]

Table 2. Contrast Match Determination Ratios

Sample	Hydrogen:Deuterium (H:D) ratio
HA_2	55/45
	45/55
	35/65
L_1	95/5
	85/15
	75/25
$L_{0\ (Authentic)}$	85/15
	45/55
$L_{0\ (emulsion)}$	85/15
	45/55

2.6.2 FORM AND STRUCTURE SAMPLE PREPARATION

All samples are prepared in 1g/L stock solutions. HA_0 and HA_1 are dissolved in deuterium oxide (D_2O):H_2O (50:50, v:v) and pH is adjusted to 9 with sodium deuteroxide (NaOD). HA_2, L_0 and L_1 are dissolved in benzene (D_6:methanol-D_4 (C_6D_6:CD_3OD) (3:1 v/v)). Experimentally determined hydrogen:deuterium (H:D) ratios are used for combining the components for analysis. The H:D ratio's for HA_2 and the lipid-like components of L_1 and L_0 are 50:50 and 85:15, respectively. Once samples are dissolved they are sonicated for one hour then mixed constantly for 48 hours. All stock solutions are then filtered using a Whatman® GFM 45µm filter to remove any remaining particles. The samples are then mixed to create the samples outlined in Table 3. Mixing of samples is dependent upon the natural abundance of the fractions for each material in the environment as determined by mass:balance ratios calculated during the extraction process described in Chapter 2.2. After mixing for natural abundance, emulsions for each sample are created by mixing one mL of sample with three mL of acidic H_20, and two mL of benzene:methanol azeotrope (3:1 v:v).[17] Emulsion samples are then vortexed for one minute and allowed to sit for 24 hours. The pH of all samples were maintained at ~ 5, authentic and emulsion samples were then layered onto one-inch quartz disks and dried in a desiccator.

Table 3. Form and Structure Factor Neutron Scattering Samples

Authentic					
Contains	**Name**	**Contains**	**Name**	**Contains**	**Name**
Leonardite		**Elliott Silt Loam**		**Pahokee Peat**	
HA_0	LHA_0	HA_0	EHA_0	HA_0	PHA_0
L_0	LL_0	L_0	EL_0	L_0	PL_0
HA_1	LHA_1	HA_1	EHA_1	HA_1	PHA_1
HA_2	LHA_2	HA_2	EHA_2	HA_2	PHA_2
L_1	LL_1	L_1	EL_1	L_1	PL_1
$HA_1 + L_0$	LHA_{02}	$HA_1 + L_0$	EHA_{02}	$HA_1 + L_0$	PHA_{02}
$HA_2 + L_1 + HA_1$	LHA_{03}	$HA_2 + L_1 + HA_1$	EHA_{03}	$HA_2 + L_1 + HA_1$	PHA_{03}
$HA_2 + L_1$	LL_{02}	$HA_2 + L_1$	EL_{02}	$HA_2 + L_1$	PL_{02}
Labeled					
$L_1 + HA_2 +$ PBA*	LL_{012B}	$L_1 + HA_2 +$ PBA*	EL_{012B}	$L_1 + HA_2 +$ PBA*	PL_{012B}
$L_1 + HA_2 +$ PAD**	LL_{012A}	$L_1 + HA_2 +$ PAD**	EL_{012A}	$L_1 + HA_2 +$ PAD**	PL_{012A}
HA_1+L_0+PBA*	LHA_{010B}	HA_1+L_0+PBA*	EHA_{010B}	HA_1+L_0+PBA*	PHA_{010B}
HA_1+L_0+PAD**	LHA_{010A}	HA_1+L_0+PAD**	EHA_{010A}	HA_1+L_0+PAD**	PHA_{010A}

* Deuterated Phenyl Butyric acid; ** Deuterated Palmitic acid

Thin layer thicknesses of the samples are shown in Table 4 in Section were calculated using

$$\frac{m}{A/\rho} \qquad (6)$$

where m is the amount of material deposited on the disk (mg), A is the area of the material deposit (mm^2), and ρ is the density of the liquid ($mg \cdot mm^{-3}$). The density used to calculate film thicknesses is the mean ρ value for H_2O and D_2O, and Benzene:methanol (3:1, v:v), for HA_0, HA_1, and HA_2, L_0 and L_1, respectively.

Table 4. Calculated Film Thickness Values

Sample*	Film Thickness (nm)	Sample*	Film Thickness (nm)	Sample*	Film Thickness (nm)	Labeled Samples (emulsions)	Film Thickness (nm)
LHA_0E	857	EHA_0E	1197	PHA_0E	644	LL_{02B}	447
LHA_0	251	EHA_0	362	PHA_0	274	LL_{02A}	911
LHA_1E	644	EHA_1E	857	PHA_1E	857	LHA_{010B}	794
LHA_1	447	EHA_1	274	PHA_1	362	LHA_{010A}	911
LHA_2E	911	EHA_2E	1476	PHA_2E	911	EL_{02B}	2205
LHA_2	286	EHA_2	286	PHA_2	338	EL_{02A}	447
LL_0E	911	EL_0E	2791	PL_0E	551	EHA_{010B}	794
LL_0	286	EL_0	286	PL_0	286	EHA_{010A}	911
LL_1E	1786	EL_1E	1240	PL_1E	618	PL_{02B}	794
LL_1	286	EL_1	1057	PL_1	405	PL_{02A}	1240
$LHA_{02}E$	857	$EHA_{02}E$	447	$PHA_{02}E$	857	PHA_{010B}	1786
$LHA_{02}R$	401	$EHA_{02}R$	644	$PHA_{02}R$	644	PHA_{010A}	1240
$LL_{02}E$	911	$EL_{02}E$	1786	$PL_{02}E$	1057		
$LL_{02}R$	447	$EL_{02}R$	286	$PL_{02}R$	338		

* E indicates emulsion; R indicates recombined

Chapter 3

Bulk Sample Characterization Results

3.1 SOLID STATE ^{13}C NMR

Differences in carbon type within NOM are commonly used as a "finger print" for identifying the source materials by ^{13}C [77,39,75] and ^{1}H NMR methods. Solid-state ^{13}C **D**irect **P**olarization **M**agic-**A**ngle **S**pinning (DPMAS) sequences were where used and corrected for incomplete relaxation by factors measured using a **C**ross **P**olarization **S**pin-lattice relaxation time experiment in combination with **TO**tal **S**ideband **S**uppression (CP/T_1-TOSS)[89] to qualitatively examine all components used in this study. The CP/T_1-TOSS sequence was used to measure the relaxation time T_1^c for each component to determine the most effective recycle delay. The distribution of organic carbon was calculated by integration of chemical shift regions as follows: 0 - 50 ppm, aliphatic carbon; 50 -108 ppm, carbohydrate carbon; 108 - 162, aromatic carbon; and 162-202, carboxyl carbon using standard Bruker® software. Calculated carbon-type distribution percentages for all materials studied are given in Tables 5-7. Figures 3-5 display the solid state ^{13}C NMR DPMAS spectra for all components of the Leonardite, Elliott Silt Loam Soil, and Pahokee Peat, respectively.

Table 5. Integrated Carbon (%) Obtained from DPMAS NMR Spectra - Leonardite

Chemical shift range (ppm)	HA_0	HA_1	HA_2	L_0	L_1
0-50	11.84	6.31	16.79	20.60	64.05
50-108	15.74	10.91	19.00	20.07	14.41
108-162	64.52	69.4	56.20	50.90	19.96
162-202	7.90	13.38	8.01	8.43	1.58

Table 6. Integrated Carbon (%) Obtained from DPMAS NMR Spectra - Elliott Silt Loam Soil

Chemical shift range (ppm)	HA_0	HA_1	HA_2	L_0	L_1
0-50	17.78	15.22	19.28	19.99	34.58
50-108	28.84	29.00	22.51	23.85	23.45
108-162	43.30	44.14	53.26	32.44	25.37
162-202	10.08	11.64	4.97	23.72	16.60

Table 7. Integrated Carbon (%) Obtained from DPMAS NMR Spectra - Pahokee Peat

Chemical shift range (ppm)	HA_0	HA_1	HA_2	L_0	L_1
0-50	6.20	11.07	14.35	14.40	68.51
50-108	19.74	18.37	21.21	25.50	15.08
108-162	55.69	53.56	53.92	47.16	13.28
162-202	18.37	17.00	10.52	12.94	3.13

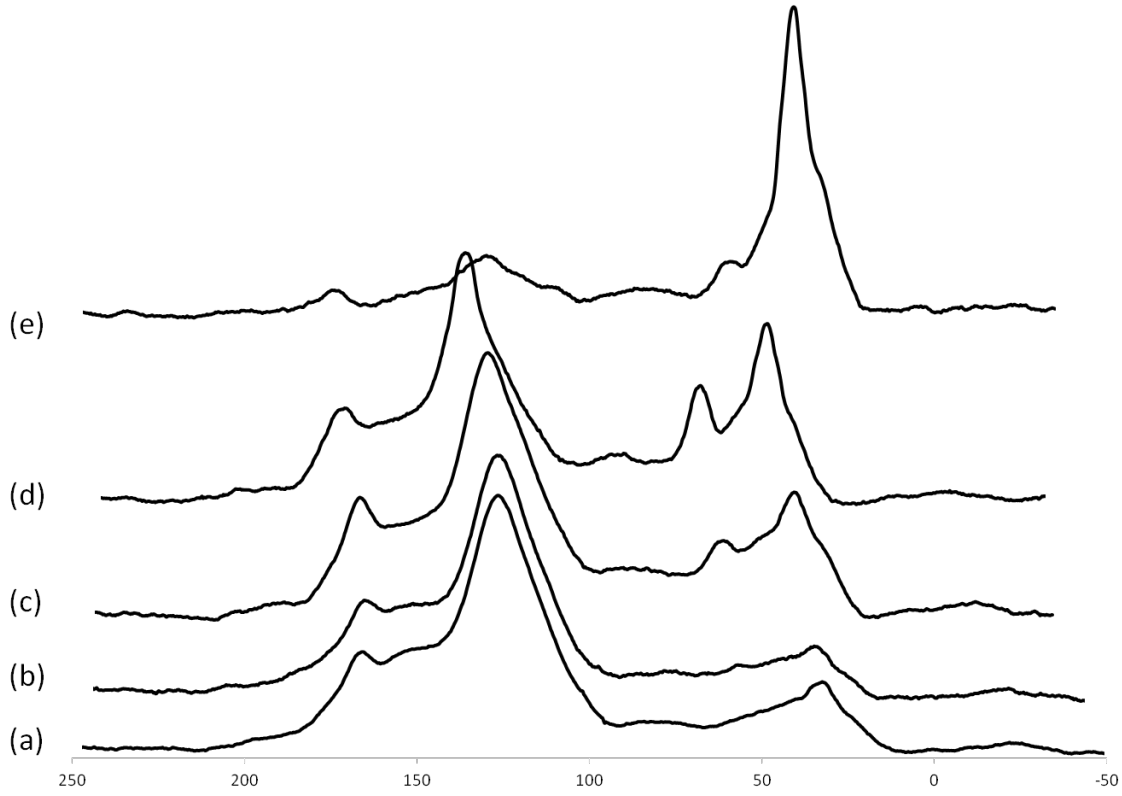

Figure 3. Solid State ^{13}C NMR of Leonardite HA_0 (a), HA_1 (b), HA_2 (c), L_0 (d), and L_1 (e).

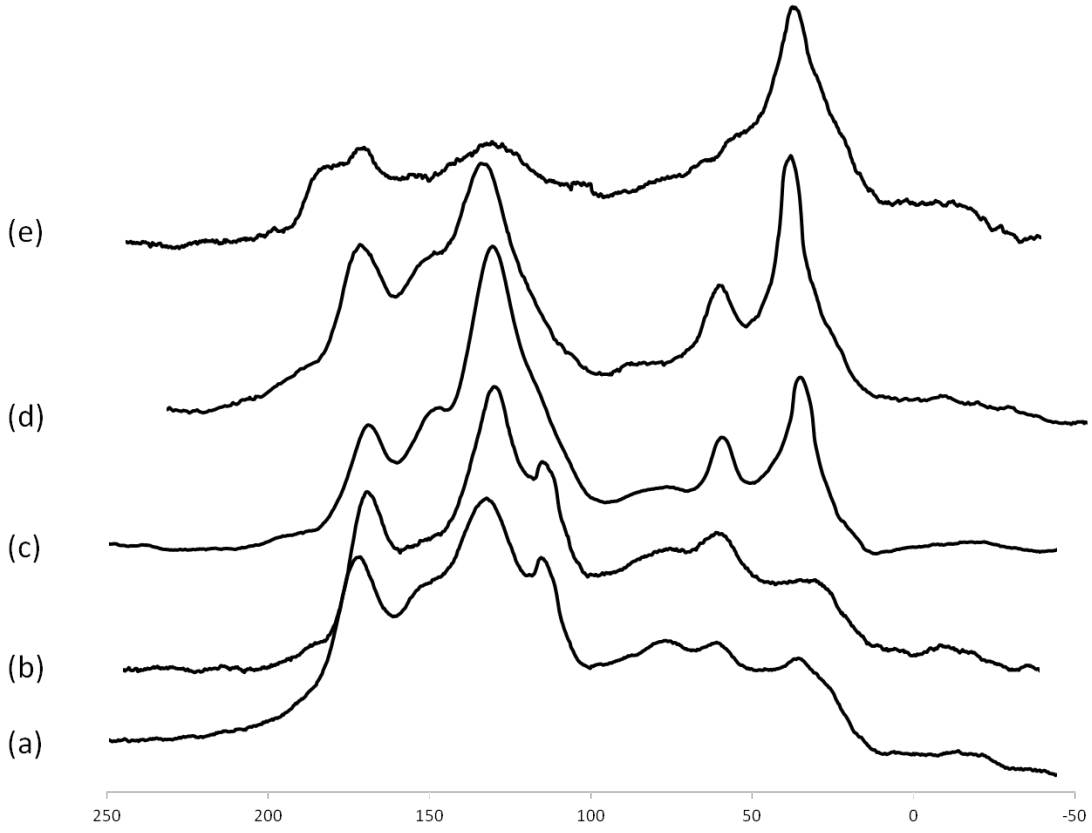

Figure 4. Solid State ^{13}C NMR of Elliott Silt Loam HA_0 (a), HA_1 (b), HA_2 (c), L_0 (d), and L_1 (e).

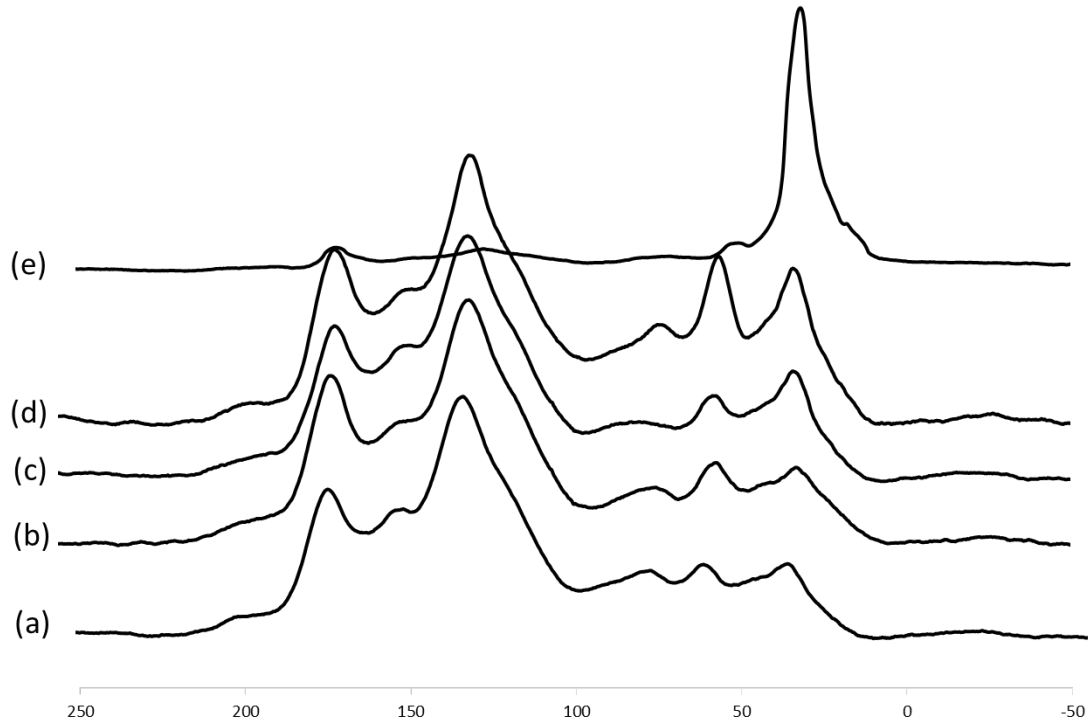

Figure 5. Solid State ^{13}C NMR of Pahokee Peat HA_0 (a), HA_1 (b), HA_2 (c), L_0 (d), and L_1 (e).

CHAPTER 4

PULSED FIELD GRADIENT NMR DETERMINATION OF THE DIFFUSION COEFFICIENTS OF THE COMPONENTS OF NATURAL ORGANIC MATTER (NOM)

4.1 INTRODUCTION

Pulsed Field Gradient (PFG) NMR was used to generate Diffusion Ordered Spectroscopy (DOSY) spectra to investigate the physical and chemical characteristics of fractionated NOM obtained from the IHSS Leonardite, Elliot Silt Loam soil, and Pahokee Peat reference materials. Diffusion coefficients (D) were determined for authentic humic acid (HA_0), methylated HA_0, the non-amphiphilic humic acid-like (HA_1), lipid-like (L_1), strongly amphiphilic (HA_2) components, and the composite of HA_2 and L_1 referred to as L_0. Chemical shift data reveal a largely aliphatic nature with minimal amounts of aromatics and carboxylic shifts in L_1, HA_2 and L_0 with higher D values than those seen for the corresponding HA_1 and HA_0. The lower D values and differences seen in the HA_0 and HA_1 components suggest that HA_2, L_1 and L_0 are smaller and chemically self-assemble to form HA_0. The assembled HA_0 was determined to be smaller than its HA_1 component indicating that the interactions of HA_1 and L_0 that create the final assembly are short-ranged. This indicates that the self-assembly of HA_0 is not simply the association of smaller molecules to create a larger assembly, but interactions create an

assembly that is chemically and physically distinct from the fractions of which is it comprised. Natural organic matter is the primary reservoir for organic carbon on the earth's surface, representing as much as an order of magnitude more organic carbon that the that in the biosphere.[11] It is a persistent form of organic carbon with diagenetic residence times in unconsolidated soils and sediments ranging from hundreds to more than a thousand years.[7,12] The study of the composition of natural organic matter (NOM) provides the opportunity to more fully understand its persistence which aids in the ability to enhance carbon sequestration in these enviroments as means of amelerioating carbon-dioxide induced climate change.

Natural organic matter is classified into fractions depending on their solubility in aqueous solution as a function of pH, (Chapter 1.3) the fraction investigated here is referred to as humic acid (HA_0), which is soluble in alkaline aqueous solution but precipitates in acidic conditions. These materials are extremely heterogeneous in nature with a variety of reactive functional groups such as carboxylic and phenolic, and aromatic carbon types. It has been suggested that this heterogeneity explains NOM's ability to resist enzymatic breakdown by bacteria.[90] To accommodate this heterogeniety it has been proposed that NOM is a self-assembled material that may be fractionated into operationally defined components[77] that are themselves innately complex. These components include HA_0, a highly aromatic non-amphiphilic component (HA_1), a lipid-like component (L_1), and an amphiphilic component (HA_2) that self-assemble via a hierarchical process.[77] The HA_2 and L_1 components assemble to form a composite referred to as L_0.[77]

Figure 2 in Section 2.2 summarizes this organizational hierarchy. These components are referred to as the "lower hierarchical level of HA_0". Subsequently, the L_0 composite and the HA_1 component interact to create HA_0. The inter-/intra-molecular interactions drive this self-assembly process are poorly understood. They can be examined using solution diffusion coefficients (D) and chemical shift data collected using pulsed field gradient (PFG) NMR which is the focus of this portion of this investigation.

Diffusion coefficients acquired by PFG NMR use a pulsed magnetic field gradient which allows the movement of molecules to be spatially resolved because the motion of a molecule is affected by its nearest neighbors.[78] The determination of D values using PFG NMR provides information regarding the inter-/intra-molecular interactions of a multi-component system. Translational diffusion is especially important when studying chemical interactions because reacting species must collide before they react.[79] PFG NMR determines the D values by measuring the attenuation of a signal resulting from the de-phasing of nuclear spins due to the combination of the translational motion of the spins of the molecules and the application of well-defined gradient pulses.[80] The NMR signal intensity (***I***) is attenuated depending upon the diffusion time, gradient strength, and pulse length. The impact of these variables on I is described by is described by Equation 1 in Chapter 2.4.

Pulse-field gradient NMR has been used to analyze the D values of complex mixtures,[91] such as SDS micelle-peptide association,[92] and ashpahltenes.[93] The D values of the components of NOM have also been investigated by a number of other analytical techniques.

Flow field-flow fractionation (FIFFF) [94] determined diffusivity values of Suwannee River humic acid in varying ionic strength solutions to range from 4.5 - 5.8 x 10^{-9} ($m^2 \cdot s^{-1}$), for UV-Vis and fluorescence detectors, respectively. Dynamic light scattering (DLS)[95] of a peat humic acid solvated in water and also in sodium chloride solutions of varying concentrations established extremely small values for D (from 2 - 9 x 10^{-11} $m^2 \cdot s^{-1}$) and concluded that the particles where large macromolecular fragments or aggregates of smaller species. Fluorescence correlation spectroscopy (FCS)[96] determined a D value range of 2 - 3 x 10^{-10} ($m^2 \cdot s^{-1}$) for Suwannee River humic acid with values decreasing slightly with decreasing pH.

Previous studies using PFG NMR[97] have determined that D values of an oak forest humic substance correlate to small molecular weight species of carbohydrates, aromatics, amino acids, and aliphatic components.[97] The carbohydrates of the NOM material in this study were determined to be the largest component, having fragments of 3 - 8 sugar units ~(600 - 1,500 Da),[97] while the D values established for the aliphatic components were consistent with monomers, dimers, trimers, and tetramers of C_{16} and C_{18} fatty esters.[97] The D values of Suwannee River fulvic acid have been studied using PFG NMR[98] concluding that the aliphatic and aromatic portions of fulvic acid assemblies extracted from numerous material types were the largest components consistently having D values lower than carbon types in other areas of the spectra evaluated. This method has also been used to determine the diffusion coefficicents of whole soil and fulvic acid extracts obtained from the surface horizon of an oak forest soil,[99] dissolved NOM in natural

waters,[100] and Suwannee River fulvic acid.[96] The computer program CONTIN[101,102] has been used to analyze PFG NMR data from several standard humic and fulvic acids samples obtained from the International Humic Substances Society (IHSS)[74] to demonstrate the polydispersitiy of these samples and how the diffusion coefficients vary with functional group composition of the individual sampoles.[103] No matter what method is used the varying diffusivities of NOM make it apparent that it is a heterogeneous material.

However, the diffusivities of the components that comprise the humic acid portion of NOM (i.e., HA_0) have not yet been studied. To understand the process of self-assembly a close look at the diffusivity and chemical shifts of HA_0, and its components is required to determine what types of inter/intra-molecular interactions are influencing its architecture. Data obtained from PFG NMR has been used to generate DOSY spectra to determine the D values and examine the possible interactions occurring between the HA_2 and L_1 components, the L_0 composite, and the HA_1 and L_0 composite which interact to for HA_0. These spectra aid in understanding the differences in the diffusivities of the aliphatic, carbohydrate, and aromatic carbon types of the components, by directing correlating the D value to the proton chemical shift in a two-dimensional plot. The entire NMR spectrum of each component is taken into account when calculating the D value. This gives a mean D value for the entire assembly rather than specific chemical shift regions as previously done.[97, 98] This established the sizes of the components relative to each other, and allows the types of inter-/intra-molecular interactions that may direct the self-assembly process to be investigated.

4.2 MATERIALS AND METHODS

HA_0 was isolated from the International Humic Substances Society Leonardite (BS104L), Elliott Silt Loam soil (BS102M), and Pahokee Peat (BS103P) bulk reference materials (Chapter 2.1) using a traditional alkaline extraction method as described in Chapter 2.2. The HA_0, HA_1, and HA_2 components of each material type were converted to the hydrogen form via cation exchange using Dowex® 50W-X H^+ resin to ensure metals which may interfere with NMR had been removed from samples (Chapter 2.4). To establish the types of inter-/intra-molecular interactions that may be occurring the HA_0 and L_0 components of each material type were methylated with diazomethane using the established procedure described in Chapter 2.4.1.[81] All samples were dissolved in either deuterium oxide (D_2O) or benzeneD_6:methanol-D_4 (C_6D_6:CD_3OD (3:1 v/v)) to a concentration of 4 g/L and then filtered using a Whatman® 0.45µm Glass Microfiber Filter (GMF) to ensure large particles which may interfere with NMR analysis had been removed. Deuterated NMR solvents D_2O (99.8% D), CD_3OD (99.6 % D), and NaOD (40% wt solution in D_2O, 99+ atom % D) were purchased from Acros Organics, C_6D_6 (99.96 % D) and DIAZALD (2 M in diethyl ether) used for methylation were purchased from Sigma Aldrich. All NMR solvents were used as received.

Solution-state ^1H NMR spectra were collected using a Bruker Avance 600 MHz NMR spectrometer fitted with a 5-mm inverse ^1H-^{13}C-^{15}N TXI probe. ^1H spectra were acquired using 16 scans and a delay of 2 seconds between pulses. PFG NMR data were obtained at 295K using a Bipolar-Pulse Pair Longitudinal-Eddy-current -Delay (BPPLED) sequence from the standard Bruker library.[82]

Scans (512-2000 depending on the signal to noise of the sample) were collected using 1.75 - 2.25 ms sine-shaped gradient pulses (3.5- 4.5 ms per bipolar pulse pair) in 24 increments from ~7-330 $mT \cdot m^{-1}$ with a diffusion time range of 75-180 ms at 295 K. The diffusion time and gradient length where optimized to achieve 95% suppression of the attenuated signal at the maximum gradient strength. Suppression of the D_2O signal was used in combination with the BPPLED pulse sequence and power levels were optimized for maximum suppression of the solvent. Diffusion coefficients were evaluated using the T_1/T_2 relaxation software included the standard Bruker TopSpin® software package. DOSY spectra were collected to directly correlate the diffusion coefficients to the proton chemical shift in a two dimensional plot. The D values obtained were used to calculate the hydrodynamic radius (R_H) for all authentic components. The hydrodynamic radius is indicative of the apparent size of the dynamic hydrated/solvated particle, and is defined as the radius of an equivalent hard sphere diffusing at the same rate as the molecule under observation which was determined using the Stokes-Einstein equation,

$$D = \frac{kT}{6\pi n R_H} \qquad (7)$$

where $\boldsymbol{k}$ is the Boltzman constant, $\boldsymbol{T}$ is the temperature in Kelvin , $\boldsymbol{\eta}$ is the solvent viscosity, and $\boldsymbol{D}$ is the diffusion coefficient.

4.3 RESULTS AND DISCUSSION

Table 8 lists the D values of all the NOM components studied. The calculated R_H values are shown in Table 9.

Table 8 . Diffusion Coefficients x 10^{-10} (m^2*s^{-1}) obtained from PFG NMR experiments. Numbers in parentheses indicate standard deviation.

	Leonardite	Elliott Silt Loam	Pahokee Peat
HA_0	4.334 ± (0.082)	1.998 ± (0.002)	2.600 ± (0.001)
HA_{0Me}	4.184 ± (0.095)	7.239 ± (0.004)	8.216 ± (0.012)
HA_1	2.204 ± (0.067)	1.617 ± (0.062)	2.587 ± (0.025)
L_0	16.88 ± (0.050)	2.091 ± (0.017)	8.761 ± (0.054)
L_{0Me}	6.246 ± (0.102)	8.283 ± (0.053)	7.496 ± (0.023)
HA_2	5.506 ± (0.075)	125.8 ± (0.078)	9.898 ± (0.057)
L_1	8.859 ± (0.039)	19.71 ± (0.019)	4.386 ± (0.014)

Table 9. Hydrodynamic radii (Å) calculated using the Diffusion Coefficients obtained from PFG NMR experiments for authentic components studied.

	Leonardite	Elliott Silt Loam	Pahokee Peat
HA_0	48.507	105.221	80.858
HA_1	95.386	130.013	81.265
L_0	12.454	100.541	23.996
HA_2	38.182	10.671	21.240
L_1	23.731	10.666	47.932

The inverse relationship between D values and particle size signifies that a particle with a larger D value is more readily able to diffuse into a solvent than a particle with a smaller D value. Conversely, components/particles with smaller D values are larger than those with relatively larger D values.[82] These data indicate that the non-amphiphilic HA_1 component, with the lowest calculated D values and the highest R_H values, is the component with the largest relative size regardless of material type.

Pahokee Peat

The DOSY spectra of the lower level components HA_2 and L_1 and the L_0 composite for Pahokee Peat are overlaid and shown in Figure 6 (DOSY spectra for individual components HA_2, L_1 and L_0 are located in the Appendix, Figures A.1, A.2 and A.3, respectively).

The amphiphilic HA_2 component has a wide resonance in the unsaturated aliphatic region (3.8 - 5.2 ppm) indicating the possible presence of numerous types of esters and C=C containing groups. When HA_2 interacts with L_1 the spectrum of resulting L_0 composite shows an up-field shift to the ester, and ether shift range between 3.0 - 4.2 ppm. The appearance of resonances in the unsaturated and saturated aliphatic regions is perhaps the result of the hydrophic effect, π-π bonding of saturated carbon, and the conjugated C=C systems, respectively. There is also a considerable size difference between L_0 and its components.

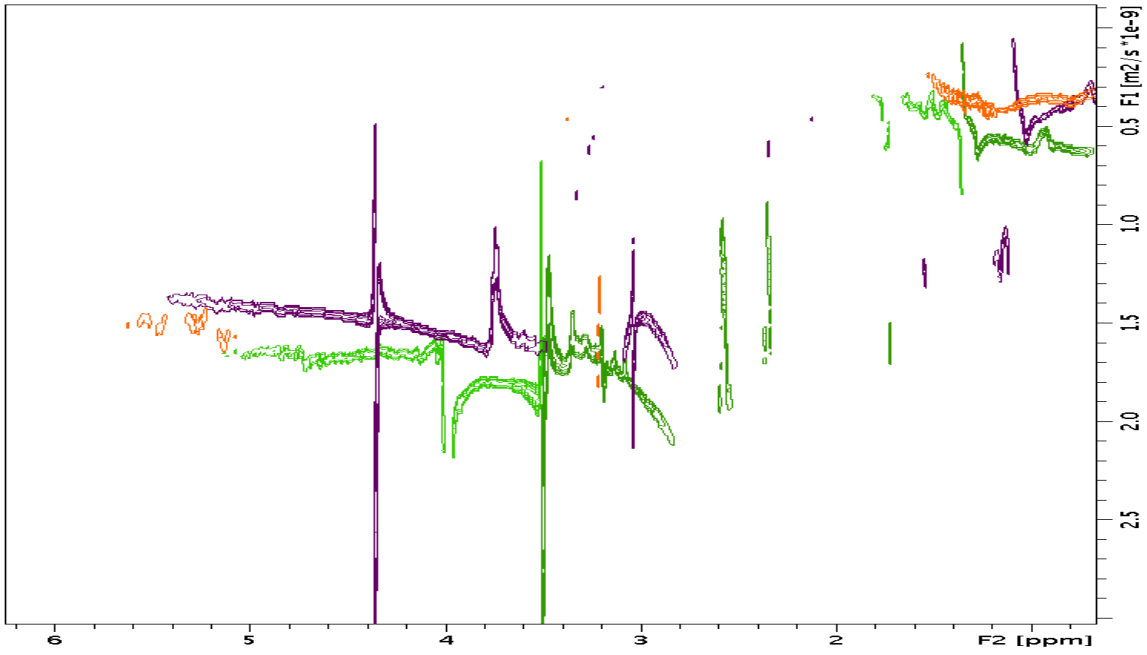

Figure 6. DOSY spectrum of L_0, HA_2, and L_1 for Pahokee Peat

Diffusion coefficients and R_H values in Tables 8 and 9, repectively, both indicate that the L_0 composite ($D = 8.761 \pm 0.054 \times 10^{-10}$ $m^2 \cdot s^{-1}$) is 50% smaller than the L_1 components

($D = 4.386 \pm 0.014 \times 10^{-10}$ $m^2 \cdot s^{-1}$), and 12% larger than the HA_2 component ($D = 9.898 \pm 0.057 \times 10^{-10}$ $m^2 \cdot s^{-1}$) which constitutes 80% of the entire L_0 assembly. This reduction in overall size of the L_0 composite when compared to its components suggests the L_1 component may be drawn into the HA_2 components by the hydrophobic effect between saturated aliphatic components bringing the components of the assembly closer together and resulting in a more compact L_0 composite. The diffusivity of L_0 is decreased futher with the interaction of L_0 with HA_1 to form HA_0. The spectrum of authentic Pahokee Peat HA_0 in Figure 7 compared to its components HA_1 and L_0 indicates that these interactions are occurring between the primarily aliphatic region of L_0 and the aliphatic and aromatic regions of HA_1. (Individual spectra of Pahokee Peat HA_0, and HA_1, are located in the Appendix, Figures A.4,and A.5, respectively).

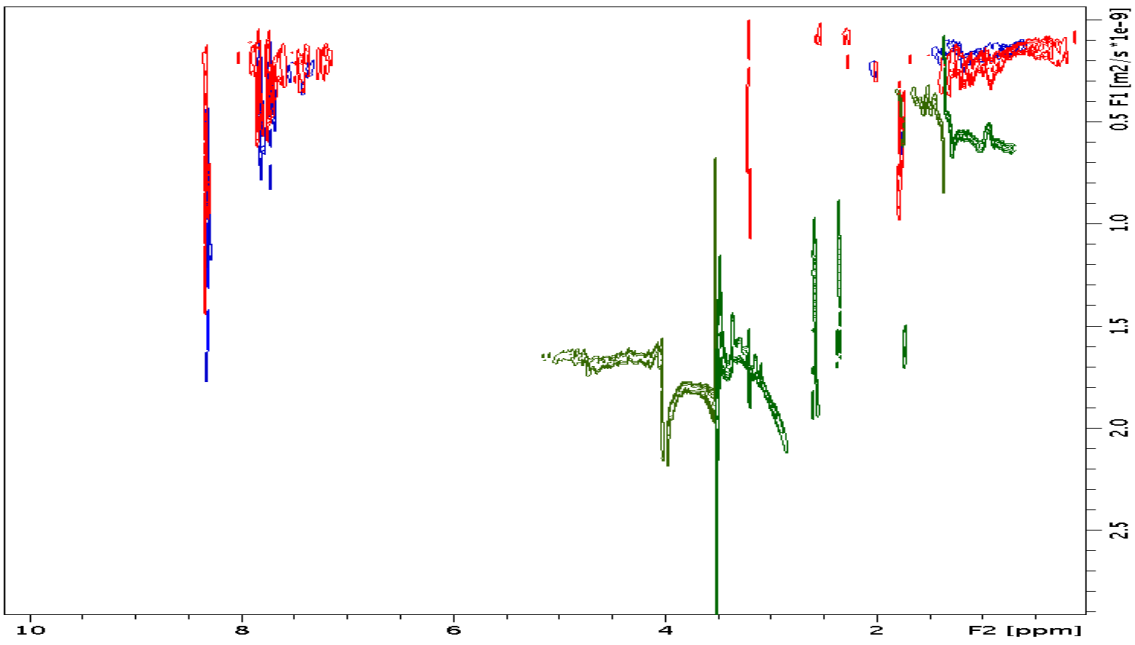

Figure 7. DOSY spectrum of HA_0, HA_1, and L_0, for Pahokee Peat

Additionally, the diffusivity is decreased when L_0 interacts with HA_1, causing HA_0 to be smaller than the major component of HA_1 which constitutes ~ 80% of the final assembled material.

Leonardite

The D and R_H values for Leonardite listed in Tables 8 and 9 indicate that L_0 is 67% smaller than HA_2 and 47% smaller than L_1. Figure 8 shows that interactions occurring between Leonardite L_1, and HA_2 create a L_0 composite smaller in size as indicated by the larger D value (individual spectra of Leonardite L_1, HA_2 and L_0 are located in the Appendix, Figures A.6, A.7 and A.8, respectively). Again, there is an up-field shift from the C=C bond region to the ester and ether range, however, the saturated aliphatic components also give a strong resonance. The decrease in size is possibly the result of extensive hydrophobic interactions due to the increase of alkyl functional groups, and π-π interactions between the unsaturated and saturated aliphatic components of L_1 and HA_2, which increases the diffusivity of L_0.

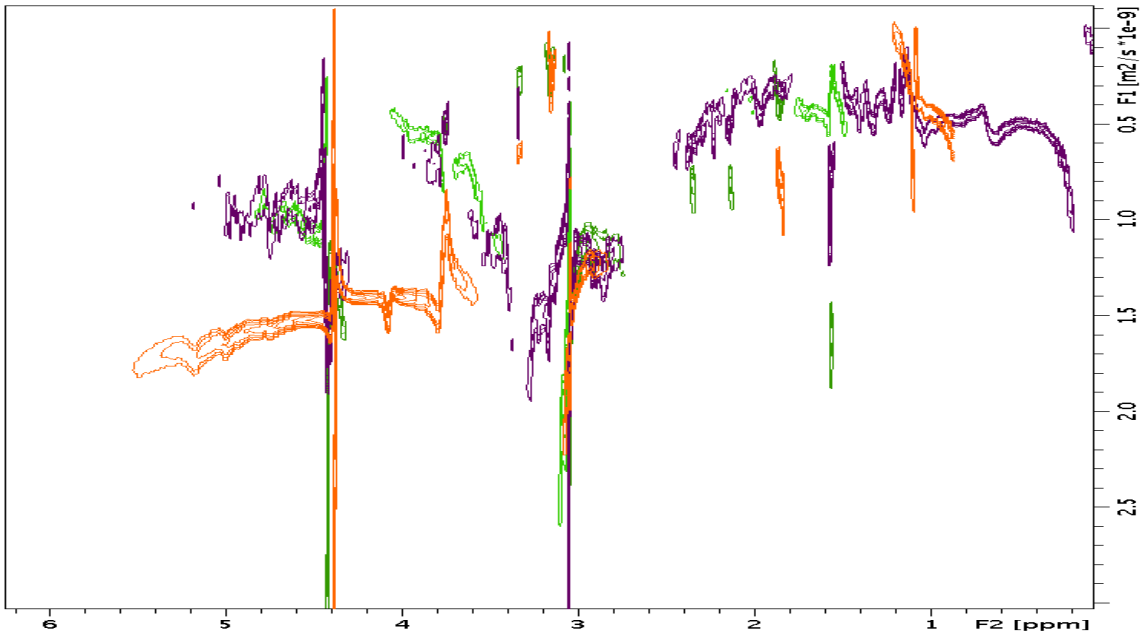

Figure 8. DOSY spectrum of L_0, HA_2, and L_1 for Leonardite

The HA_1 shown in Figure 9 ($D = 2.204 \pm 0.067 \times 10^{-10}$ $m^2 \cdot s^{-1}$) and L_0 ($D = 16.88 \pm 0.050 \times 10^{-10}$ $m^2 \cdot s^{-1}$) interact to form HA_0 which is 50% smaller ($D = 4.334 \pm 0.095 \times 10^{-10}$ $m^2 \cdot s^{-1}$) than the HA_1 which comprises 70% of the assembled material. This suggests that the interactions of HA_1 and the much smaller L_0 is creating inter-molecular cross-linkages which pull the components closer together than the individual components resulting in a size decrease. (Individual spectra of Leonardite HA_1 and HA_0, are located in the Appendix, Figures A.9, and A.10, respectively).

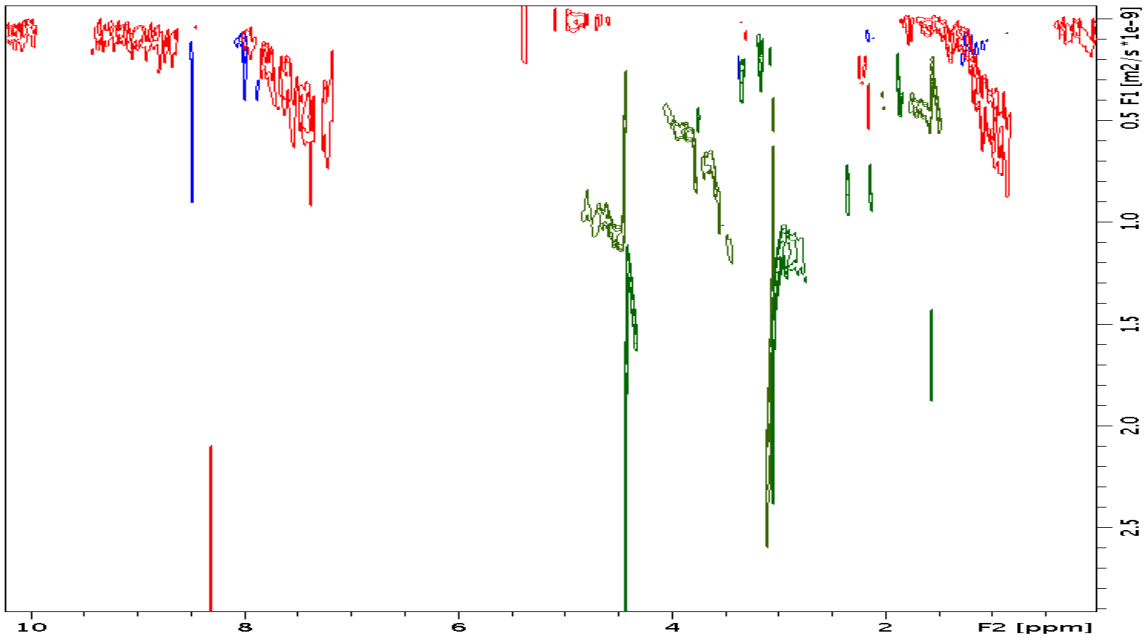

Figure 9. DOSY spectrum of HA_0, HA_1, and L_0 for Leonardite

Elliott Silt Loam Soil

The Elliott Silt Loam soil L_0 shown in Figure 10 has a D value (Table 8; D = 2.091 ± 0.017 x 10^{-10} $m^2 \cdot s^{-1}$) which demonstrates that it is 166%, and 90% larger than the HA_2 in (D = 125.8 ± 0.078 x 10^{-10} $m^2 \cdot s^{-1}$) and L_1 (D = 19.71 ± 0.019 x 10^{-10} $m^2 \cdot s^{-1}$) components, respectively. (Individual spectra of Elliott Silt Loam L_0, HA_2, and L_1, are located in the Appendix, Figures A.11, A.12 and A.13, respectively).

The DOSY spectrum of L_0 closely resembles that of its HA_2 component. As with Leonardite, interactions between HA_2 and L_1 cause an up-field shift from the C=C bond region to the ester and ether range, and the aliphatic components also give a strong resonance in the DOSY spectrum.

The D value for L_0 listed in Table 8 indicates it is much larger that the components from which it is comprised, suggesting aggregation may occur to form a highly-branched configuration that drastically decreases the diffusivity of the composite.

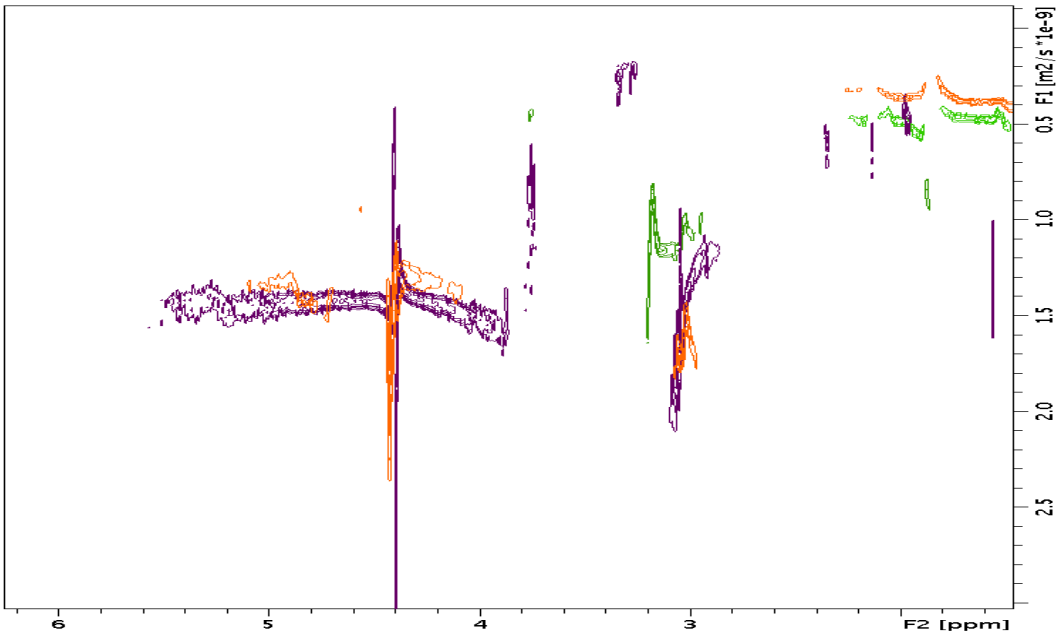

Figure 10. DOSY spectrum of L_0, HA_2, and L_1 for Elliott Silt Loam soil

According to data in Tables 8 and 9 interactions between L_0 and the non-amphiphilic HA_1 give rise to an HA_0 ($D = 1.998 \pm 0.002 \times 10^{-10}$ $m^2 \cdot s^{-1}$) displayed in

Figure 11 very similar in size to L_0, and only slightly smaller than HA_1 in Figure 20 ($D = 1.617 \pm 0.062 \times 10^{-10}$ $m^2 \cdot s^{-1}$) which constitutes ~90% of the total assembly. However, there is a substantial decrease in the L_0 component resonances after associating with HA_1.

This along with the similarity in size between HA_1 and the HA_0 assembly could indicate the L_0 component is incorporating itself into the organized HA_1 components through hydrophobic, and π-π interactions leaving the diffusivity of the final HA_0 assembly to be only slightly larger than the HA_1 component. Yet, a narrowing of chemical shift resonance bands indicates a decrease in heterogeneity of the aromatic, saturated and unsaturated aliphatic compounds as represented in the comparison DOSY spectrum for HA_0 and HA_1. (Individual spectra of Elliott Silt Loam HA_0, and HA_1, are located in the Appendix, Figures A.14 and A.15, respectively).

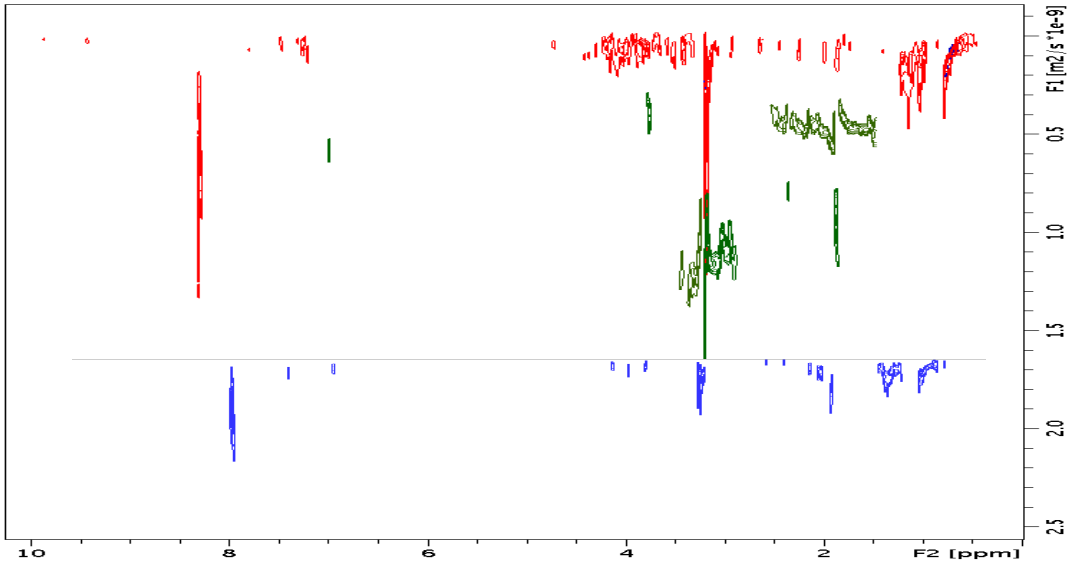

Figure 11. DOSY spectrum of HA_0, HA_1, and L_0 for Elliott Silt Loam soil (The intensity of the HA_1 spectrum obscures HA_0 so it is shown as an insert, x-axis is to scale, y-axis is from 0-2 x 10^{-9})

Methylated Samples

The HA_0 and L_0 components of the three materials studied were methylated using diazomethane which has been shown to disrupt hydrogen bonding of carboxyl and hydroxyl groups by converting them to methyl esters.[104,81] Comparison of the D values (Table 8) of authentic HA_0 to the methylated HA_0 for the materials studied indicates methylation of HA_0 makes a substantial difference in the size of HA_0 of the Elliott Silt Loam and Pahokee Peat samples with a decrease in overall size of HA_0 by ~70% for both materials. The size difference between the methylated HA_0 and authentic HA_0 for Leonardite is only slight and essentially within the experimental error of the size measurement. As expected, methylation causes an up-field shift in the ^1H NMR resonance of HA_0 for all materials, which correlates to an increase in aliphatic components are displayed in Figures 12, 13 and 14 for Leonardite, Elliott Silt Loam, and Pahokee Peat, respectively.

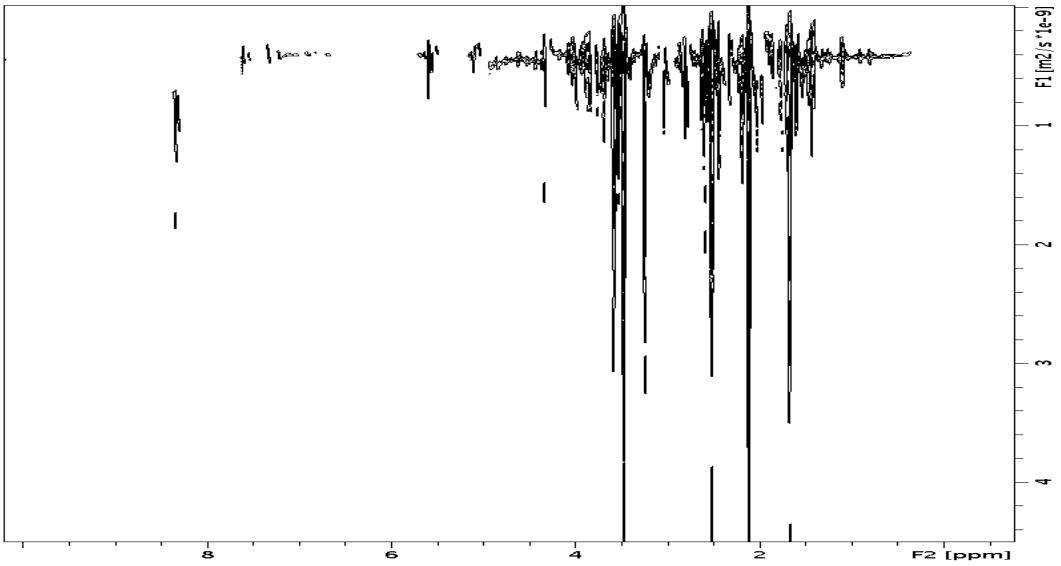

Figure 12. DOSY spectrum of methylated Leonardite HA_0

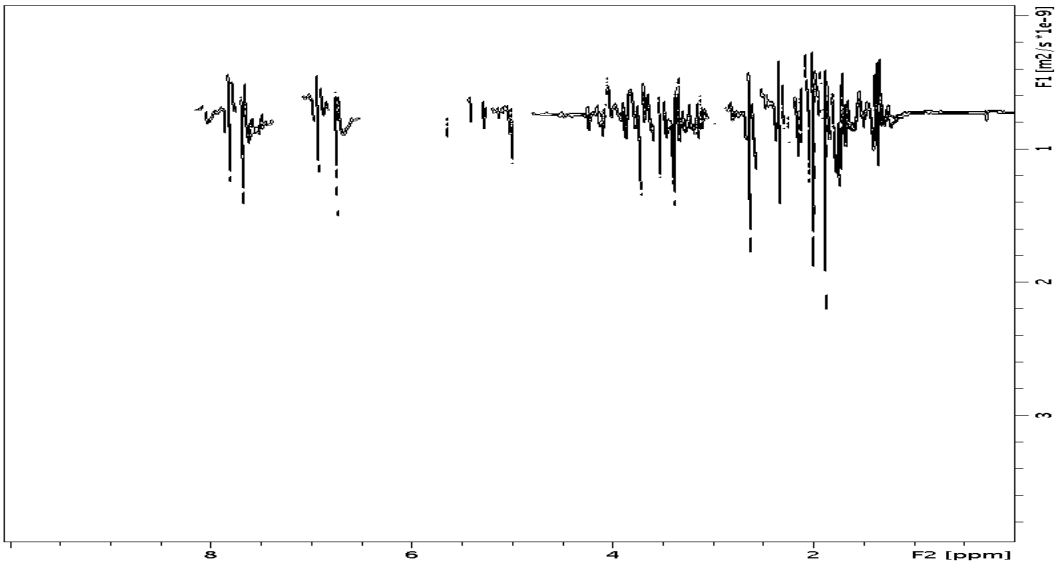

Figure 13. DOSY spectrum of methylated Elliott Silt Loam HA_0

The large decrease in overall size in HA_0 for Elliott Silt Loam and Pahokee Peat may be attributed to the larger number of functional groups susceptible to methylation than Leonardite.[74]

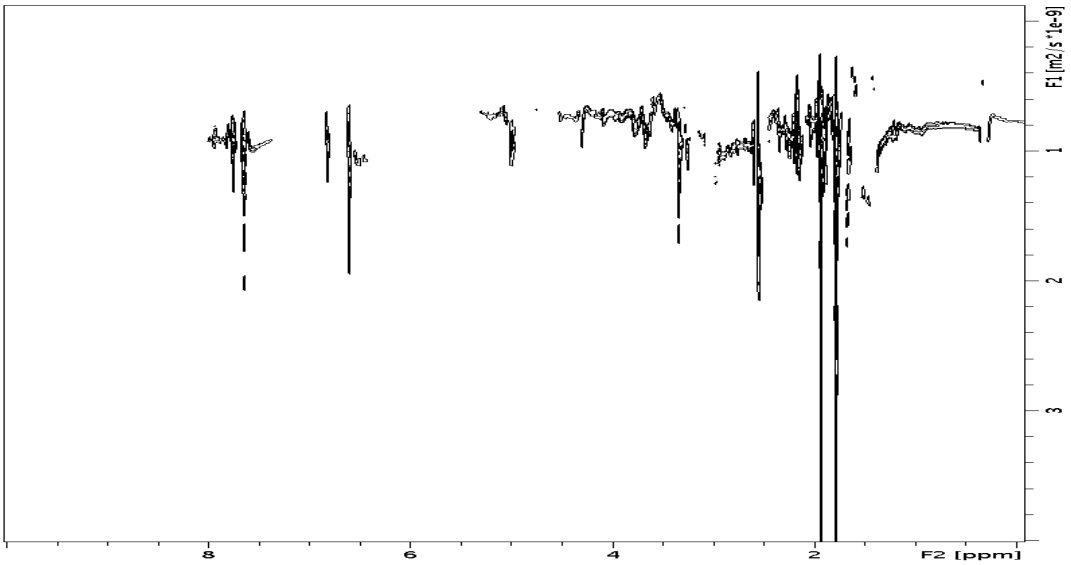

Figure 14. DOSY spectrum of methylated Pahokee Peat HA_0

Given the inverse relationship of D to particle size, the increase in the D values of HA_0, indicates that the components of HA_1 and L_0 create a HA_0 assembly that is not simply the sum of its component parts, but is the result of chemical interactions. The differences in both the D and R_H values as well as changes seen in the DOSY spectra for the L_0 and HA_1 components when compared to HA_0 indicate an increase in heterogeneity as self-assembly progresses. Comparison DOSY spectra of authentic and methylated L_0 components of Leonardite, Elliott Silt Loam and Pahokee Peat are shown in Figures 15, 16 and 17, respectively.

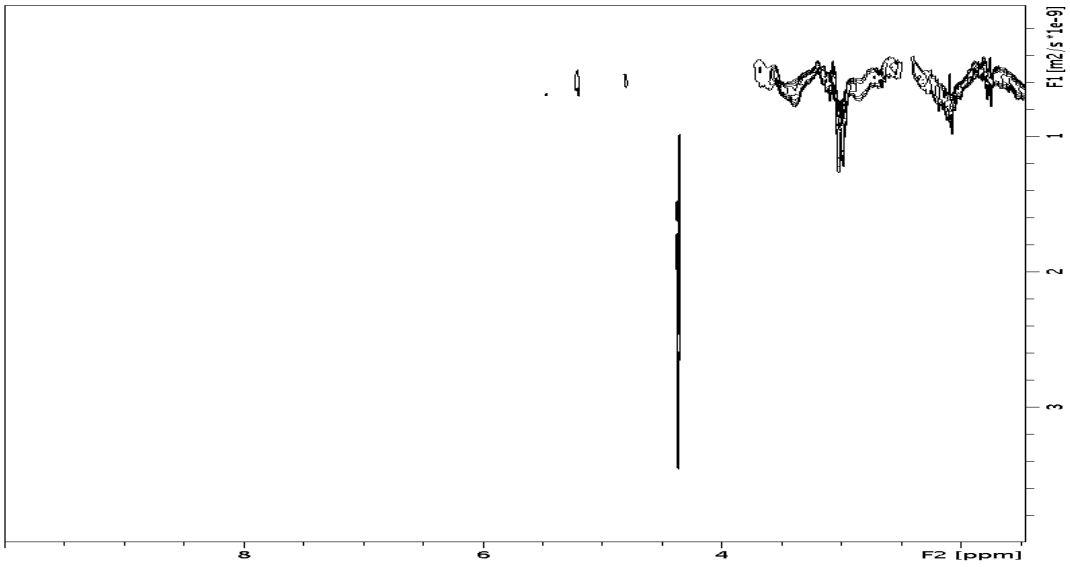

Figure 15. DOSY spectrum of methylated Leonardite L_0

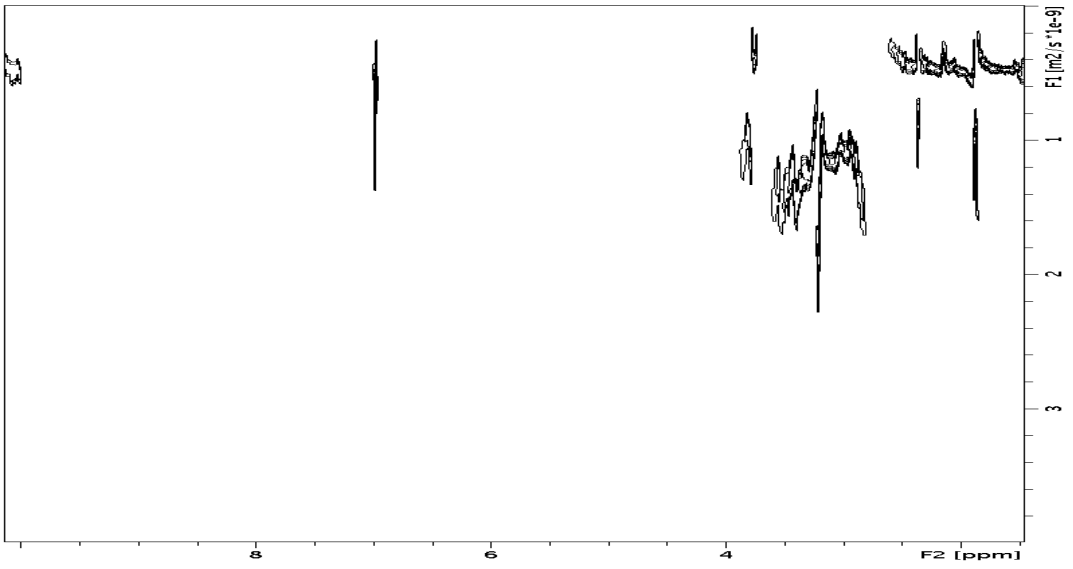

Figure 16. DOSY spectrum of methylated Elliott Silt Loam L_0

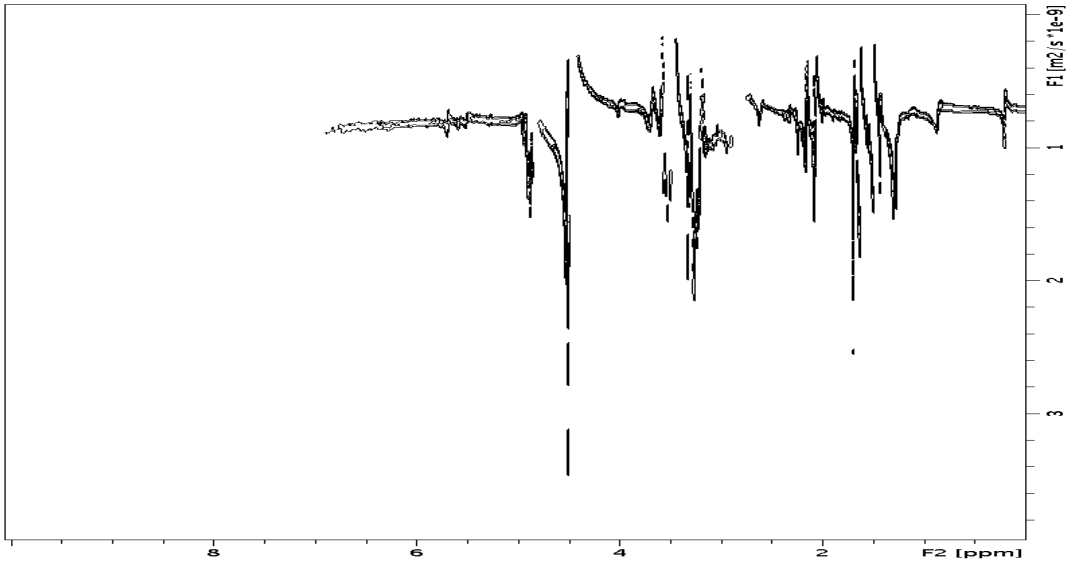

Figure 17. DOSY spectrum of methylated Pahokee Peat L_0

4.4 CONCLUSIONS

The diffusivities of the lower-level components of HA_0 (i.e., HA_2 and L_1) varied widely which indicates a large disparity of molecular sizes between material types for L_1 and HA_2 which self-assemble to form the composite L_0. Conversely, the chemical shift data for the lower-level components are quite similar with the only striking difference seen in the poly-dispersity in the 3.8 - 5 ppm region of the HA_2 component of the Elliott Silt Loam soil in comparison to the other two material types.

The D values of the final HA_0 and HA_1 component, which is the major component of HA_0 (with the exception of Leonardite HA_0) fall between 1.6 - 2.6 x 10^{-10} $m^2 \cdot s^{-1}$. This indicates that although these materials consist of small molecules that vary in size from one material to another their DOSY spectra suggest that they are still chemically very similar.

The D values for the HA_1 components for all materials studied are lower than the final HA_0 assembly. Larger D values of components indicates smaller size relative to other components contained within the assembly. This inverse relationship between diffusion coefficients and molecular size indicates that the interactions occurring between HA_1 and the L_0 composite to create the HA_0 assembly are short ranged interactions (i.e. van der Waals, π-π, and hydrogen bonding) which is smaller than the corresponding HA_1 component. The calculated R_H values also support this conclusion. These data indicate that the self-assembly process of HA_0 is not simply the aggregation of smaller molecules to create a larger particle, but involves chemical interactions between components to create an assembly that is chemically and architecturally dissimilar than the fractionated components from which it is comprised. This study suggests that once the initial onset of self-assembly begins the components of NOM, regardless of material type, create assemblies with similar size, chemical characteristics and architecture.

CHAPTER 5

CHARACTERIZATION OF FRACTIONATED NATURAL ORGANIC MATTER USING SMALL-ANGLE NEUTRON SCATTERING

5.1 INTRODUCTION

Natural organic matter, like the much older asphaltenes, are known to be complex mixtures of fractal aggregates and exhibit power law scattering. Therefore, it is difficult to assume a specific model that can be used to fit the scattering data. Because of their fractal nature, determination of the fractal dimension (***D***) for all components must occur early in the data analysis process. (The bold "**D**" refers to fractal dimension while the normal font "D" is used for diffusion coefficient). The power-law exponent (PLE) of the slope of a plot of *I(q)* versus *q* conveniently allows for the calculation of the ***D*** value for that particle. The R_H values are then used to calculate S/V ratios to ascertain a general shape for the particles of interest. A spherical shape was assumed for the S/V calculations so S/V values were determined by using the surface and volume of a sphere

$$\frac{4\pi {R_H}^2}{\frac{4}{3}\left(\pi {R_H}^3\right)} = 3/R_H \qquad (12)$$

where R_H is the hydrodynamic radius determined by PFG-NMR in Chapter 4. The ability of NOM to reassemble was investigated by Chilom[88] who used Differential Scanning Calorimetry (DSC) to determine the heat capacity (C_p) values of both recombined and

emulsified NOM samples to show that the emulsification process successfully reassembled fractionated NOM. This investigation uses SANS to study authentic, recombined, and emulsified samples of NOM to investigate changes in particle aggregation as it affects the fractal dimension during the emulsification process. In an effort to ascertain information to access how the assembly of NOM occurs, the data collected from SANS in combination with previously calculated R_H values are used to determine the general shape of the particles of the components of all materials studied.

Small angle scattering of x-rays and neutrons is a widely used technique to determine size, shape and internal structure of particles ranging in size from a few nanometers to a few hundreds of angstroms.[105,106,107] Small Angle Neutron Scattering (SANS) detects the momentum transfer (or scattering angle and phase shift) of the incident neutrons after interacting with materials. Usually information obtained during a scattering experiment of NOM found where the scattering angles satisfy the relationship[108]

$$0.1 \leq ql \qquad (9)$$

where (l) is the diameter of the scattering particle, and the scattering vector (q) is defined by Equation 2. The interaction between the neutron and the particles in a sample results in a momentum transfer which contains information about nanoscale structure in the sample. SANS data can provide information regarding the spatial variations in scattering length density in a sample, and there is a direct correlation in dilute solutions between the particle shape and its scattering data.

However, if concentrations increase the assumption of the average distance between particles to be essentially larger than their dimensions is no longer valid,[109] and consequently, in addition to *intra*-particle scattering, *inter*-particle scattering arising from larger-range correlations must be taken into consideration.[110, 111,112] The intra-particle scattering is expressed as the form factor P(*q*), where *q* is the scattering length vector. The inter-particle scattering is expressed as the structure factor S(*q*), which describes the interacting system and depends on the relative locations of individual particles. SANS measurements give the scattering intensity as a function of the scattering vector (equivalent to the momentum transfer) which carries particle structure and interaction information. The scattering intensity, *(I)*, as a function of the scattering vector, *q*, is used to estimate the size and shape of the scattering material in the sample.[109] The expression for a two component system is

$$I(q)=\Phi(1-\Phi)\Delta^2 V_p P(q)S(q) \quad (10)$$

where Φ is the volume fraction of the scattering particles, $\Delta\rho^2$ is the scattering contrast, V_p is the particle volume, *P(q)* is the form factor (describing particle shape, size and polydispersity), and *S(q)* is the structure factor (describing interactions between particles). However, the materials studied herein were dried films and are not believed to be singular particles, but aggregates containing either single or multiple components of the fractionated whole HA_0 as seen in Chapter 2.2 Figure 2. In addition, the heterogeneity of NOM makes using a model tailored for a particular particle shape difficult when fitting the scattering data.

A model independent analysis, which relies upon surface-to-volume (S/V) ratios has been used successfully to determine the approximate shape of asphaltene aggregates[69] and is used for the samples in this study. While S/V values can provide information regarding the approximate shape of aggregates they provide no information regarding aggregate size. Therefore, diffusion coefficient values calculated from Diffusion Ordered Spectroscopy (DOSY) spectra from a previous study[113] were used to calculate the hydrodynamic radius (R_H) for authentic components of NOM. The R_H is indicative of the apparent size of the dynamic hydrated/solvated particle, and is defined as the radius of an equivalent hard sphere diffusing at the same rate as the molecule under observation which was determined using the Stokes-Einstein equation,

$$D = \frac{kT}{6\pi n R_H} \qquad (11)$$

where k is the Boltzman constant, T is the temperature in Kelvin, η is the solvent viscosity, and D is the diffusion coefficient.

Fractal Dimension (D)

Mandelbrot[114] suggested that classical Euclidian classical geometry did not adequately describe the irregular surfaces, shapes with uneven edges and rough corners seen in the natural world. Fractals are described as shapes that are detailed at all levels of scale with the most striking characteristic being their self-similarity.[114] The fractal dimension (***D***) characterizes a self-similar material's space filling capacity,[115] and is obtained when Equation 9 is satisfied.[116,117] The fractal dimension also determines if a particle is a

surface fractal or a mass fractal, the physical differences between these types of fractals is illustrated in Figure 18. Surface fractals (Figure 18a) are particles that essentially have a space filled interior but a rough surface. In contrast, mass fractals (Figure 18b) not only have rough surfaces the irregularity exits throughout the entire particle.

A mass fractal ***D*** value between 1-2 would represent an architecture is similar to a slice of Swiss cheese with a value of 2 being a planar smooth surface. Conversely, surface fractal ***D*** values between 2-3 would represent an architecture similar to a sponge with a value of

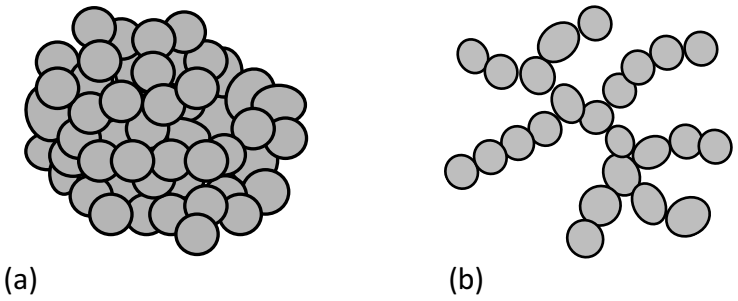

Figure 18. Illustration of a (a) Surface fractal, and (b) Mass fractal

3 being a smooth-surfaced, completely space-filling object. As previously mentioned the ***D*** value is determined using the power-law exponent and can be determined from SANS data by the slope of a Log/Log plot of *I(q)* versus *q* with a constant baseline applied during the fitting of all scattering data. If a sample is a mass fractal, then the fractal dimension is the absolute value of the power-law

$$I(q) \propto q^{-Dm} \qquad (13)$$

exponent and $\boldsymbol{D} < 3$.[116] If a sample is a surface fractal the fractal dimension is described by

$$I(q) \propto q^{6-D} \qquad (14)$$

where the power law exponent has a value that satisfies $3 < (6 - \boldsymbol{D}) \leq 4$.[116] It has been previously determined that NOM exists as surface fractals in the solid state[118] and mass fractals in solution.[119]

Fractal dimension values in the range of 1.7-1.8 are reported for systems that exhibit quickly occurring Diffusion-Limited Aggregation (DLA) while Reaction-Limited Aggregation (RLA) systems have $\boldsymbol{D}$ values of 2.2 and above.[120] The observed differences being that DLA occurs between particles upon collision, and produces open structures as seen in the lower $\boldsymbol{D}$ value. RLA requires more collisions to occur before reaction ensues allowing the particles to penetrate deeper into other particles producing higher $\boldsymbol{D}$ values meaning denser aggregates as a result. It is assumed in RLA that there is a repulsive barrier that must be overcome before contact can be made between particles and/or clusters before aggregation may occur.

5.2 MATERIALS AND METHODS

All samples were initially prepared as 1g/L stock solutions. HA_0 and HA_1 were dissolved in a D_2O:H_2O mixture (50:50, v:v) and pH is adjusted to 9 with sodium deuteroxide (NaOD). HA_2, L_0 and L_1 are dissolved in benzene (D_6:methanol-D_4 (C_6D_6:CD_3OD) (3:1 v/v)). Experimentally determined hydrogen:deuterium (H:D) ratios for HA_2, L_1 and L_0

were 50:50 and 85:15, respectively. In an attempt to increase scattering intensity of samples select samples were labeled with 5% deuterated 4-phenylbutyric acid (PBA), or 5% deuterated palmitic acid (PAD) and are listed in Table 10. PBA and PAD are chosen for their general structural similarities to HA_2 and L_1, respectively. Dissolved samples are sonicated for one hour then mixed constantly for 48 hours. All stock solutions are then filtered using a Whatman® GFM 45µm filter to remove any remaining particles. The samples are then mixed to create the samples outlined in Table 10. Mixing of samples was dependent upon the natural abundance of the fractions for each material in the environment as determined by mass balance ratios calculated during the extraction process described in Chapter 2.2. After mixing for natural abundance emulsions for each sample were created by mixing one mL of sample with three mL of acidic H_2O, and two mL of benzene:methanol azeoptrope (3:1 v:v). Emulsion samples were then vortexed for one minute and allowed to sit for 24 hours. The pH of all samples were adjusted and maintained at ~ 5 then authentic and emulsion samples were layered onto one-inch quartz disks and dried. Thin layer thicknesses of the samples are shown in Table 3 in Section 2.5.2 were calculated using

$$\frac{m}{A/\rho} \qquad (15)$$

where m is the amount of material deposited on the disk (mg), A is the area of the material deposit (mm^2), and ρ is the density of the solvating liquid ($mg \cdot mm^{-3}$). The density used to calculate film thicknesses is the mean ρ value for H_2O and D_2O (50:50, v:v) for HA_0, HA_1, and HA_2, and Benzene:methanol (3:1, v:v), for L_0 and L_1.

Table 10. Neutron scattering sample mixtures

Authentic					
Leonardite		**Elliott Silt Loam**		**Pahokee Peat**	
HA_0	LHA_0	HA_0	EHA_0	HA_0	PHA_0
L_0	LL_0	L_0	EL_0	L_0	PL_0
HA_1	LHA_1	HA_1	EHA_1	HA_1	PHA_1
HA_2	LHA_2	HA_2	EHA_2	HA_2	PHA_2
L_1	LL_1	L_1	EL_1	L_1	PL_1
$HA_1 + L_0$	LHA_{02}	$HA_1 + L_0$	EHA_{02}	$HA_1 + L_0$	PHA_{02}
$HA_2 + L_1 + HA_1$	LHA_{03}	$HA_2 + L_1 + HA_1$	EHA_{03}	$HA_2 + L_1 + HA_1$	PHA_{03}
$HA_2 + L_1$	LL_{02}	$HA_2 + L_1$	EL_{02}	$HA_2 + L_1$	PL_{02}
Labeled					
$L_1 + HA_2$ + PBA*	LL_{012B}	$L_1 + HA_2$ + PBA*	EL_{012B}	$L_1 + HA_2$ + PBA*	PL_{012B}
$L_1 + HA_2$ + PAD**	LL_{012A}	$L_1 + HA_2$ + PAD**	EL_{012A}	$L_1 + HA_2$ + PAD**	PL_{012A}
HA_1+L_0+PBA*	LHA_{010B}	HA_1+L_0+PBA*	EHA_{010B}	HA_1+L_0+PBA*	PHA_{010B}
HA_1+L_0+PAD**	LHA_{010A}	HA_1+L_0+PAD**	EHA_{010A}	HA_1+L_0+PAD**	PHA_{010A}

* Deuterated 4-Phenylbutyric acid; ** Deuterated Palmitic acid

5.2.1 SMALL-ANGLE NEUTRON SCATTERING (SANS)

SANS experiments were conducted using the EQ-SANS at Oak Ridge National Laboratory (ORNL) Spallation Neutron Source (SNS) using 60 Hz operation. Sample to detector distance was 4 meters using varying wavelength bands collectively to cover a q range of 0.003 $Å^{-1} < q < 0.4$ $Å^{-1}$.

5.3 RESULTS AND DISCUSSION

Leonardite

As shown in Figure 19 authentic HA_0 shows higher scattering intensity than any of the corresponding recombined or emulsified samples. Because the scattering intensity is proportional to the summation of cross sections of all aggregates the decrease in intensity seems to indicate that single particles not contributing to aggregate formation increase in the emulsions and recombined samples.

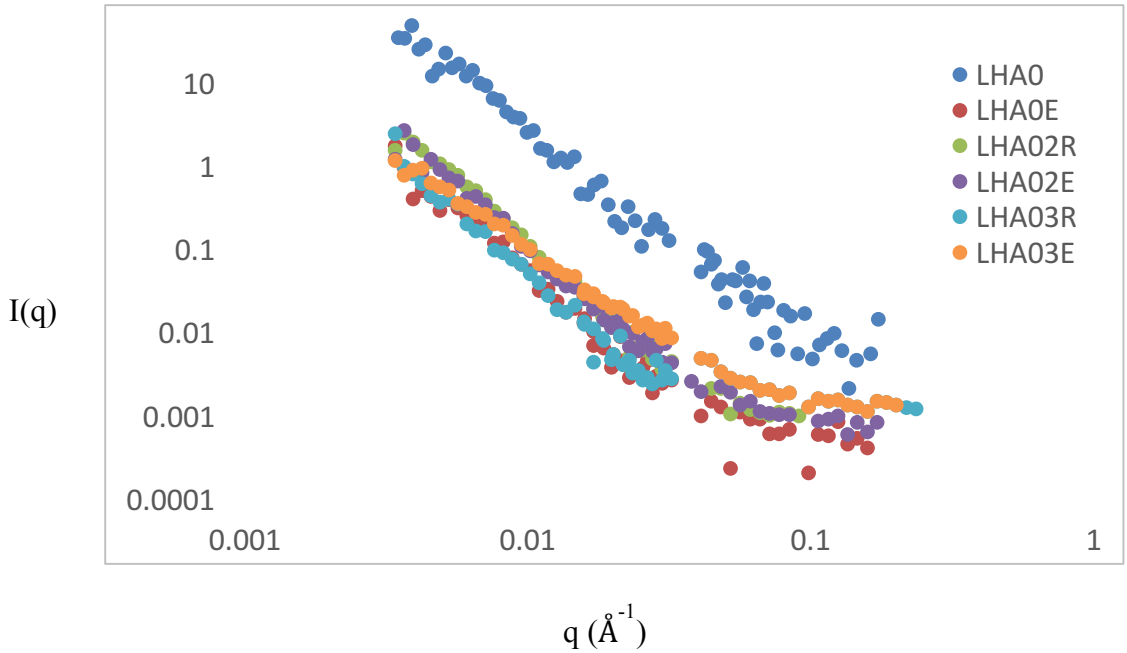

Figure 19. Scattering comparison plot authentic, emulsified, and recombined Leonardite HA_0

This is more clearly seen in Figure 20 which compares the emulsified unfractionated LH_{A0} (LHA_{0E}) to the authentic and PBA (LHA_{010BE}) and PAD (LHA_{010AE}) labeled

samples. It is apparent that neither the emulsification process or labeling with PBA or PAD were successful in either creating assemblies similar to the authentic material, or enhancing the scattering intensity of the aromatic (PBA labeled) or aliphatic (PAD labeled) components.

Comparable to LHA_0 neither the emulsion nor the labeling process appear to affect the scattering intensity of the L_0 composite as seen in Figure 21. Also similar to LHA_0 the LHA_1 (Figure 22) and LHA_2 (Figure 23) the L_0 components show a decrease in scattering intensity with emulsification. Not seen in scattering plots before the LH_{A2} and LL_1 components (Figures 23 and 24) show the presence of inelastic scattering apparent by the change in slope seen at high *q* in their respective plots. This inelastic scattering is an instrument artifact due to incoherent scattering caused by the thermalization of hydrogen neutrons,[121] indicating a larger amount of hydrogen within these specific samples when compared with most other components studied.

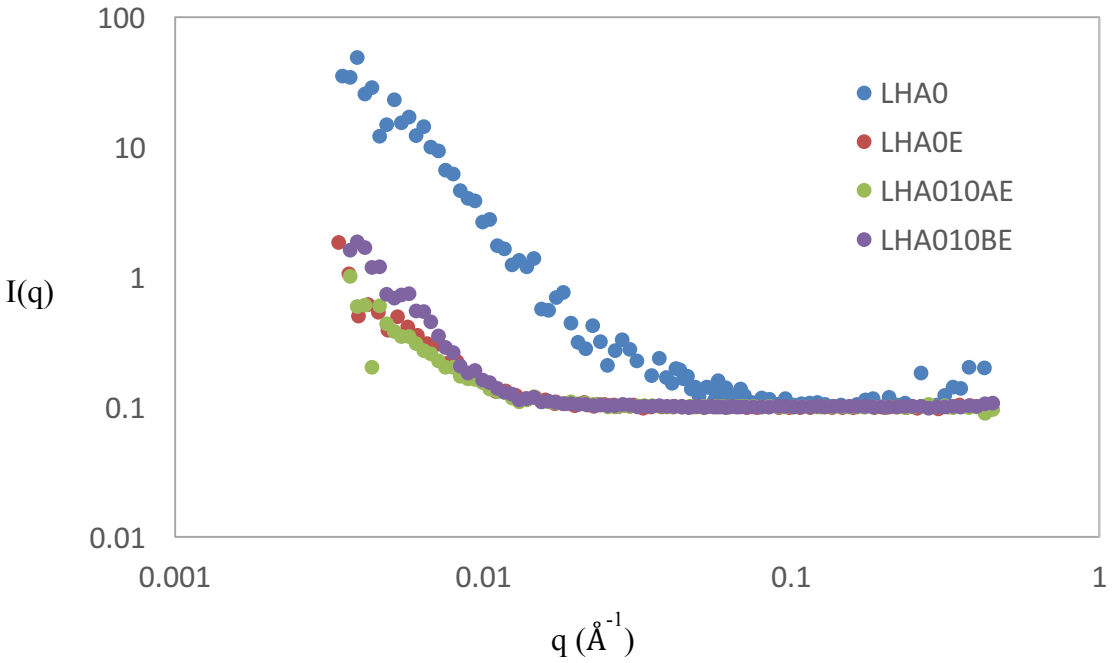

Figure 20. Scattering comparison plot authentic, PAD and PBA labeled Leonardite HA_0

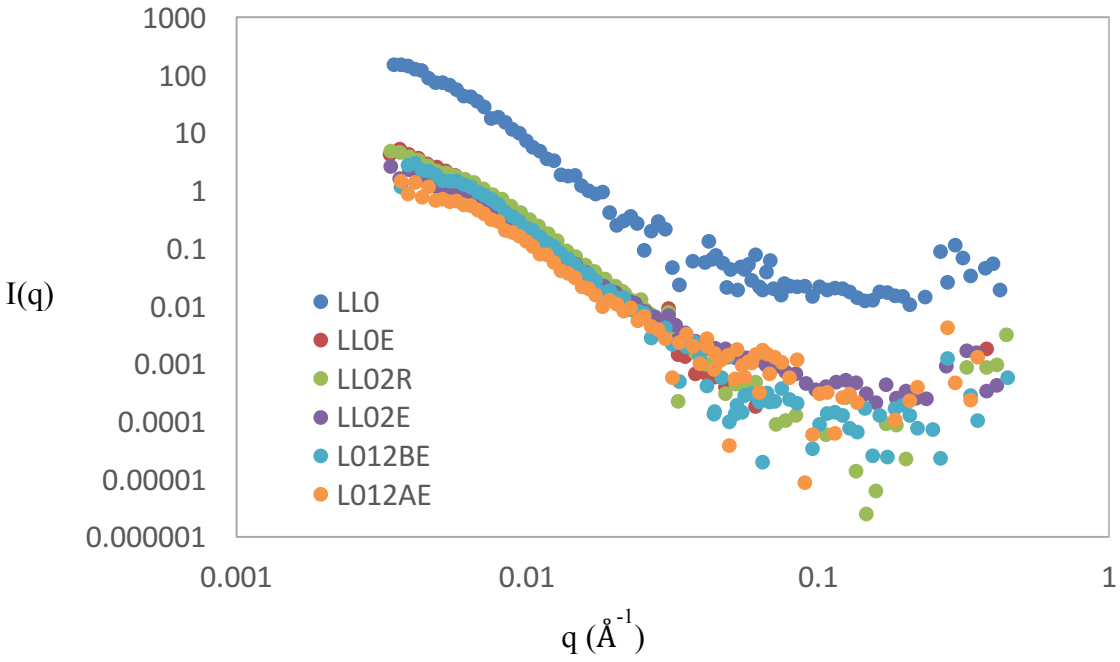

Figure 21. Scattering comparison plot authentic, PAD and PBA labeled Leonardite L_0

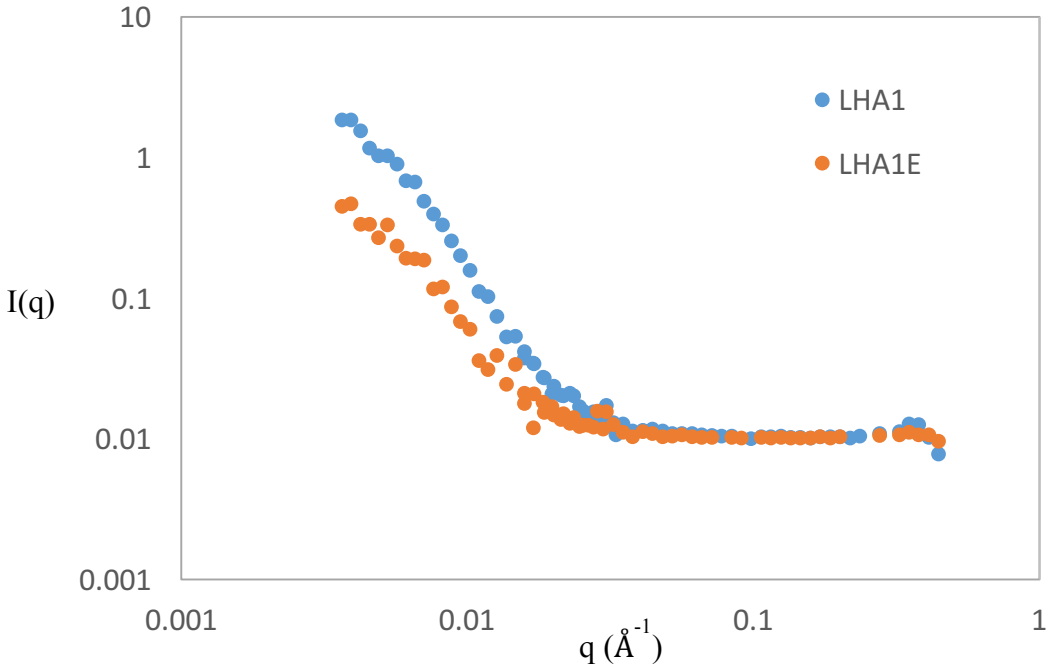

Figure 22. Scattering comparison plot authentic, emulsified Leonardite HA_1

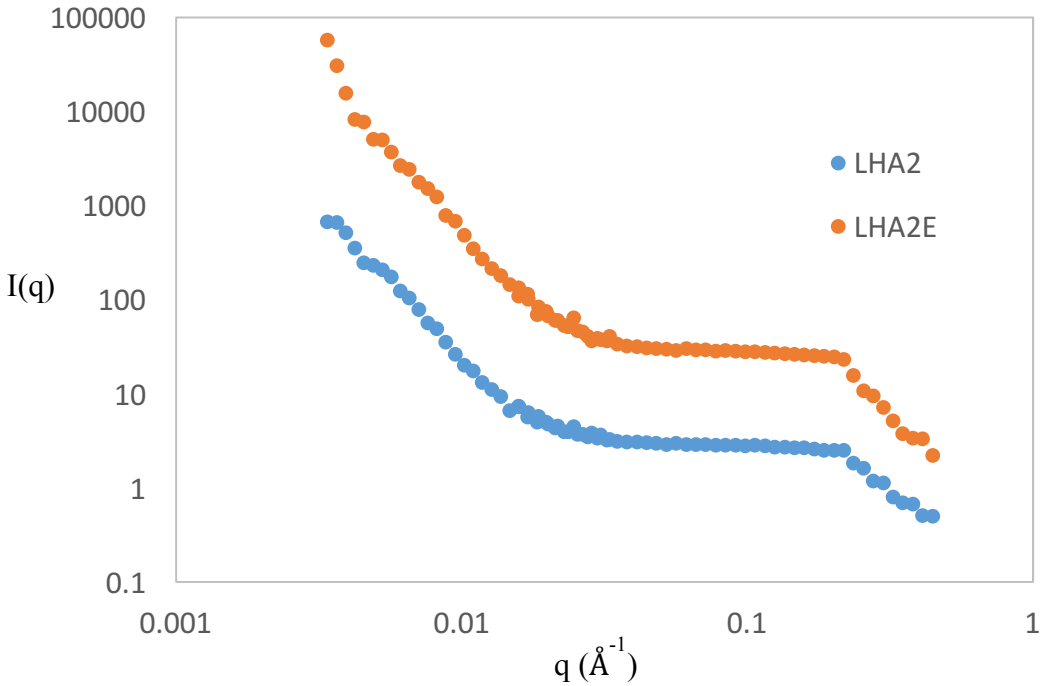

Figure 23. Scattering comparison plot authentic, emulsified Leonardite HA_2

Unlike all other Leonardite components emulsification drives much more aggregation of LL_{1E}, and also seems to create a more organized assemblies as indicated by the enhance smoothness of the plot in Figure 33. The emulsification process appears to increase the ability of this lipid-like component to aggregate when compared with the authentic LL_1 sample. This enhanced aggregation may be additional hydrogen bonding and the hydrophobic effect due to acidic H_2O used in the emulsification process.

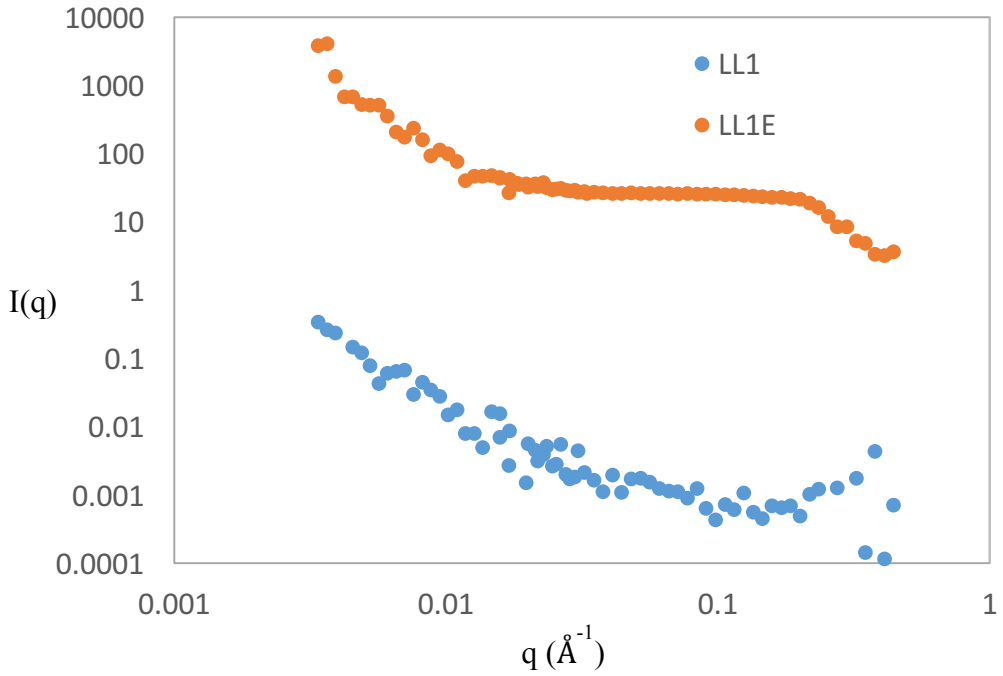

Figure 24. Scattering comparison plot authentic, emulsified Leonardite L_1

Elliott Silt Loam

The Elliott Silt Loam HA_0 plot seen in Figure 25 shows no significant difference when comparing the authentic, emulsified, and recombined sample intensities. However, it is

notable that the Elliott Silt Loam recombined samples show higher intensities than the authentic or emulsified samples. This is unusual because these samples have been fractionated and then simply mixed together in natural abundance ratios as described in Materials and Methods. Due to previous work by Chilom,[88] it was expected that the emulsion samples would have higher scattering intensities than the recombined samples for all materials studied.

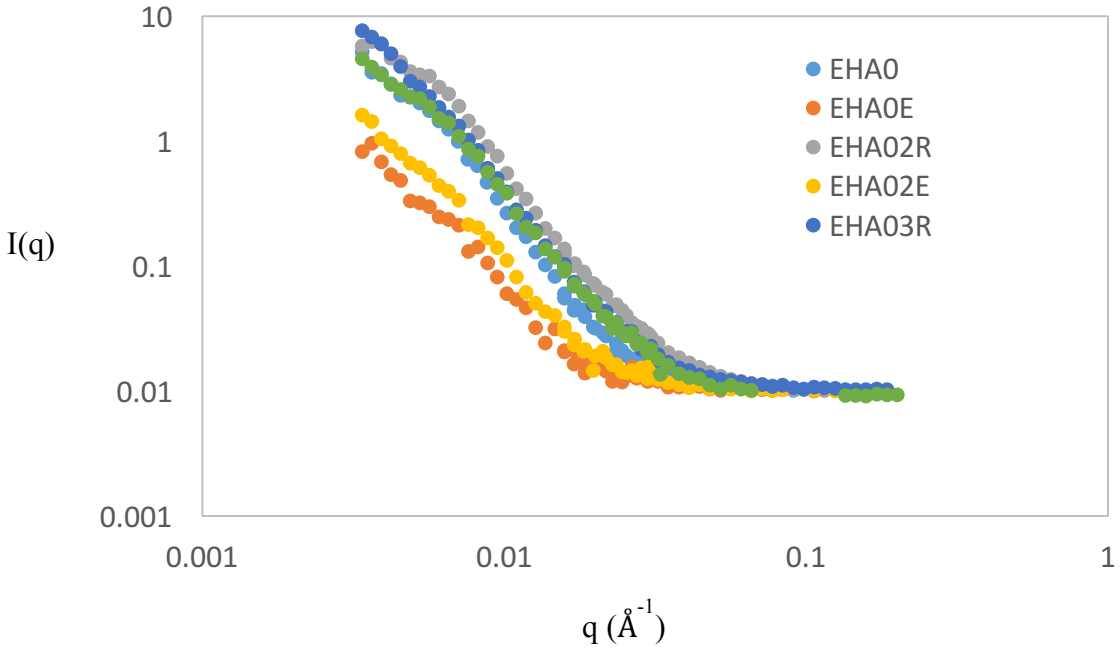

Figure 25. Scattering comparison plot authentic, emulsified, and recombined Elliott Silt Loam HA_0

In Figure 26 the PBA labeled sample (EHA_{001BE}) shows a scattering intensity that is the same as the authentic EHA_0, while the PAD labeled sample (EHA_{010AE}) has a decrease in intensity. These results are indicative to the labeling process being effective in the Elliott

Silt Loam material. Meaning that authentic EH_{A0} is highly aromatic so it would be appropriate for the PBA labeled sample to mirror the authentic EH_{A0}. Conversely the PAD labeled samples has a decreased intensity due to the aliphatic components of the EHA_0 sample are ~2.3% of the total organic carbon.

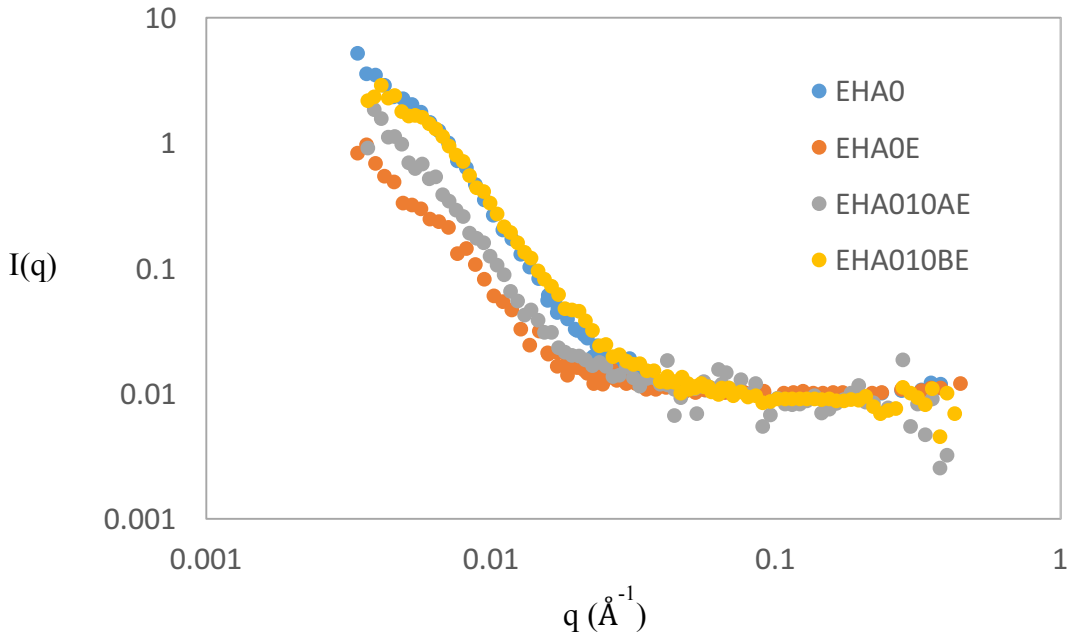

Figure 26. Scattering comparison plot authentic, PAD and PBA labeled Elliott Silt Loam HA_0

Authentic, emulsified and recombined EL_0 scattering intensities are relatively the same indicating the emulsification and recombination processes created composites similar to the authentic L_0. As shown in Figure 27, labeling the aromatics and aliphatics with PBA and PAD, respectively enhance the scattering intensity of these carbon types beyond that of the authentic sample. Another striking feature is the aliphatic enhancement intensity is the same as the aromatic intensity. This is surprising because the EL_0 composites are

composed of ~ 70% HA_2 and ~ 30% L_1, so the assumption would be the EL_{012BE} would have an intensity similar to EL_0, while EL_{012AE} would be lower.

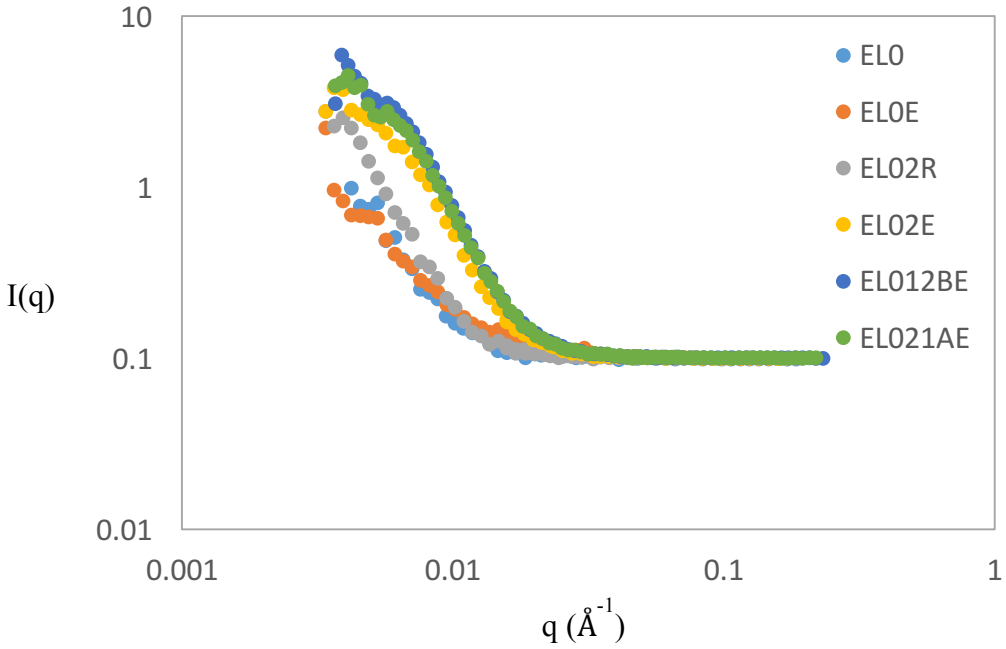

Figure 27. Scattering comparison plot authentic, emulsified, recombined and labeled Elliott Silt Loam L_0

Although different responses are seen from the EHA_0 assembly and the EL_0 composite to the emulsion, recombination and labeling processes it is clear that these processes have an effect on the aggregation of these samples.

Unlike the analogous samples of Leonardite it can be seen in Figures 28 and 29 the emulsification process does increase the scattering intensity of both EHA_1 and EHA_2. However, a similarity is seen between these samples and LL_1 and LHA_2 with evidence of an instrumentation artifact due to the thermalization of hydrogen as indicated by the change of slope at higher *q* values.

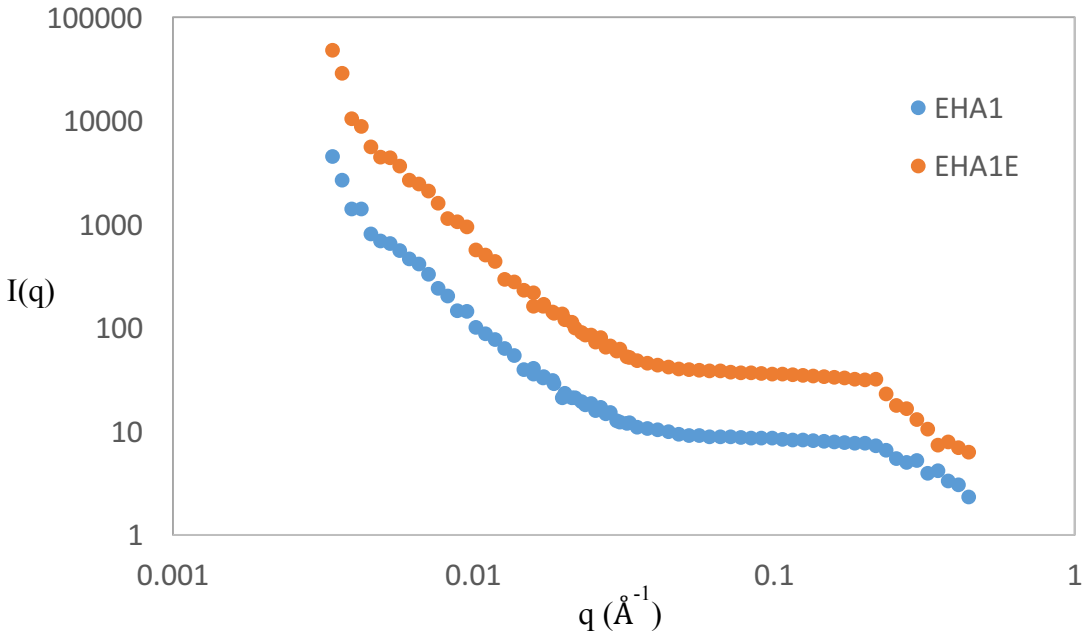

Figure 28. Scattering comparison plot authentic, and emulsified Elliott Silt Loam HA_1

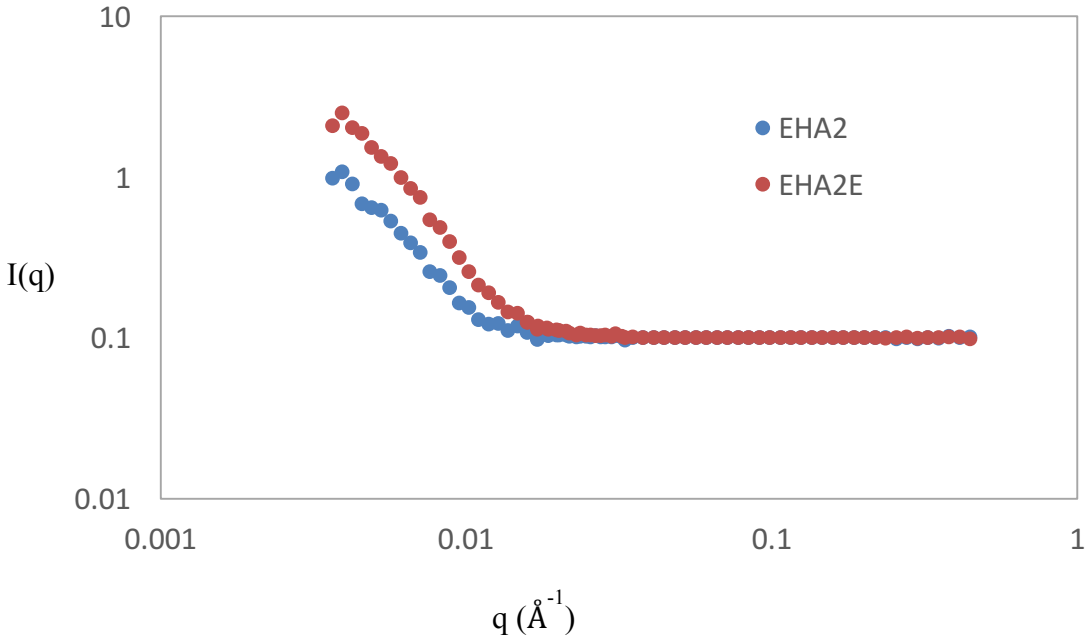

Figure 29. Scattering comparison plot authentic, emulsified Elliott Silt Loam HA_2

The plot of EL_1 (Figure 30) shows extremely weak scattering relative to other samples studied and shows no definitive differences between the authentic EL_1 and the emulsified EL_{1E}. Therefore, no assertions to how the emulsification may or may not have affected this sample can be made.

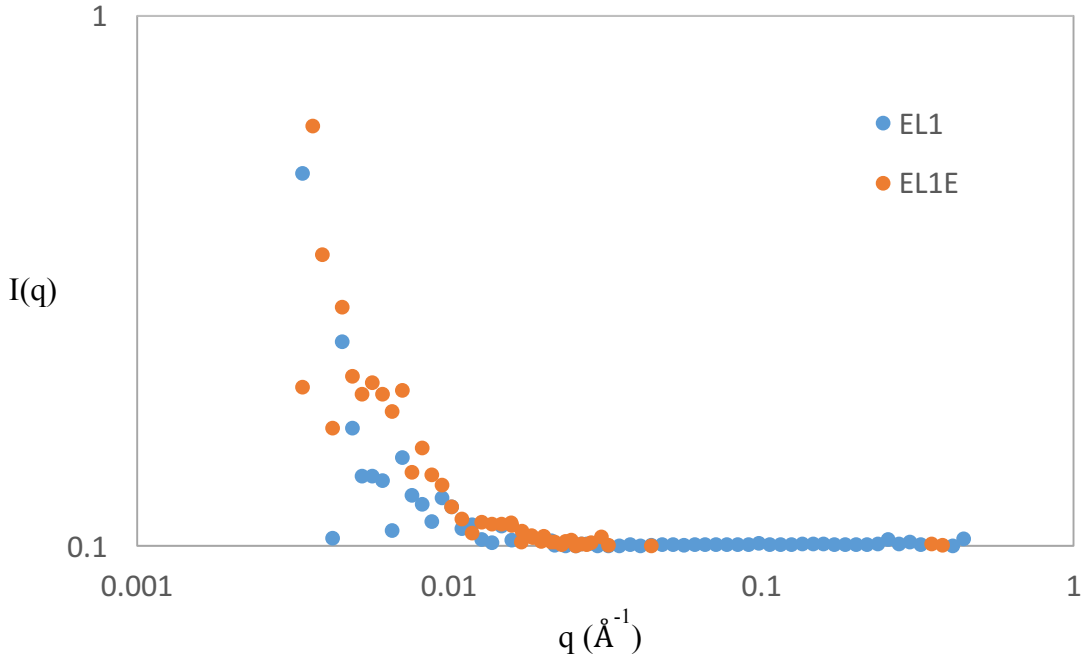

Figure 30. Scattering comparison plot authentic, and emulsified Elliott Silt Loam L_1

Pahokee Peat

The Pahokee Peat HA_0 plot seen in Figure 31 shows no significant difference when comparing the authentic, emulsified, and recombined sample intensities. There is only a slight decrease in intensity between the PHA_0 and the other samples indicating that single

particles not contributing to aggregate formation increase in the emulsions and recombined samples for this material. As with Leonardite this is further demonstrated in Figure 32 which compares the emulsified unfractionated PHA_{A0} (PHA_{0E}) to the authentic and PBA (PHA_{010BE}) and PAD (PHA_{010AE}) labeled samples. It is apparent that neither the emulsification process or labeling with PBA or PAD were successful in either creating assemblies similar to the authentic material, or enhancing the scattering intensity of the aromatic (PBA labeled) or aliphatic (PAD labeled) components. Similar to the labeled Elliott Silt Loam HA_0 aliphatic and aromatic enhancement intensity does not correlate to the actual sample composition of ~ 65% HA_2 and ~ 35% L_1. Unlike the L_0 composites of the other two materials the emulsification process did slightly enhance the scattering intensity of the authentic PL_0 as shown in Figure 33. However, the recombined and labeled samples scattering intensity is relatively the same as the authentic sample so the labeling process for this material appears to be ineffective.

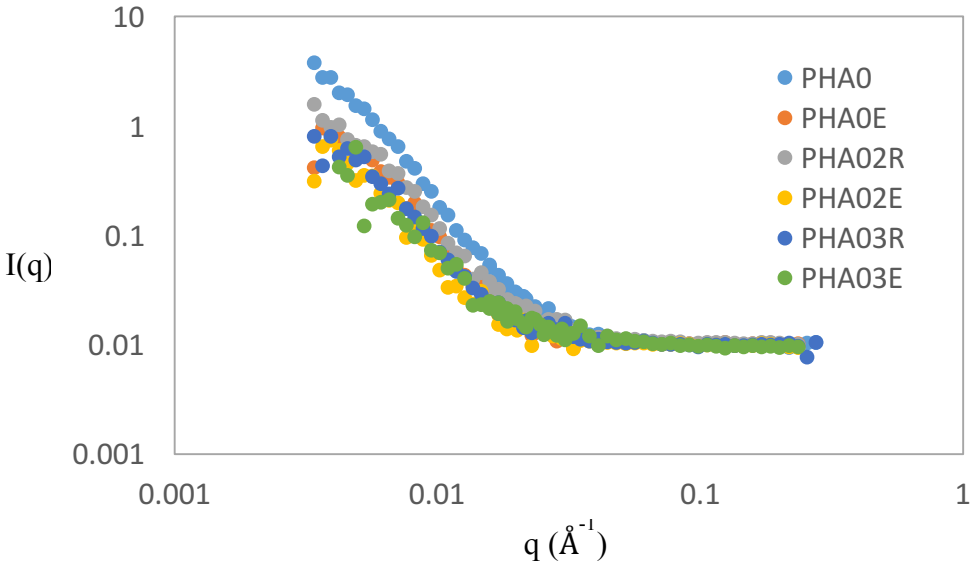

Figure 31. Scattering comparison plot authentic, emulsified, and recombined

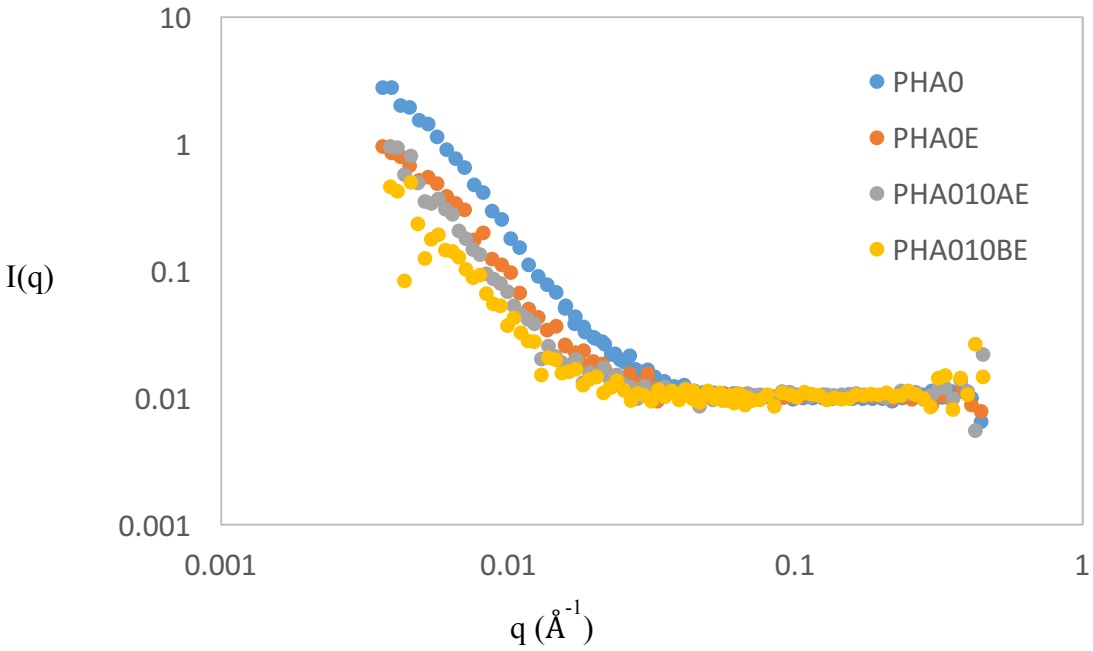

Figure 32. Scattering comparison plot authentic, PAD and PBA labeled Pahokee Peat HA_0

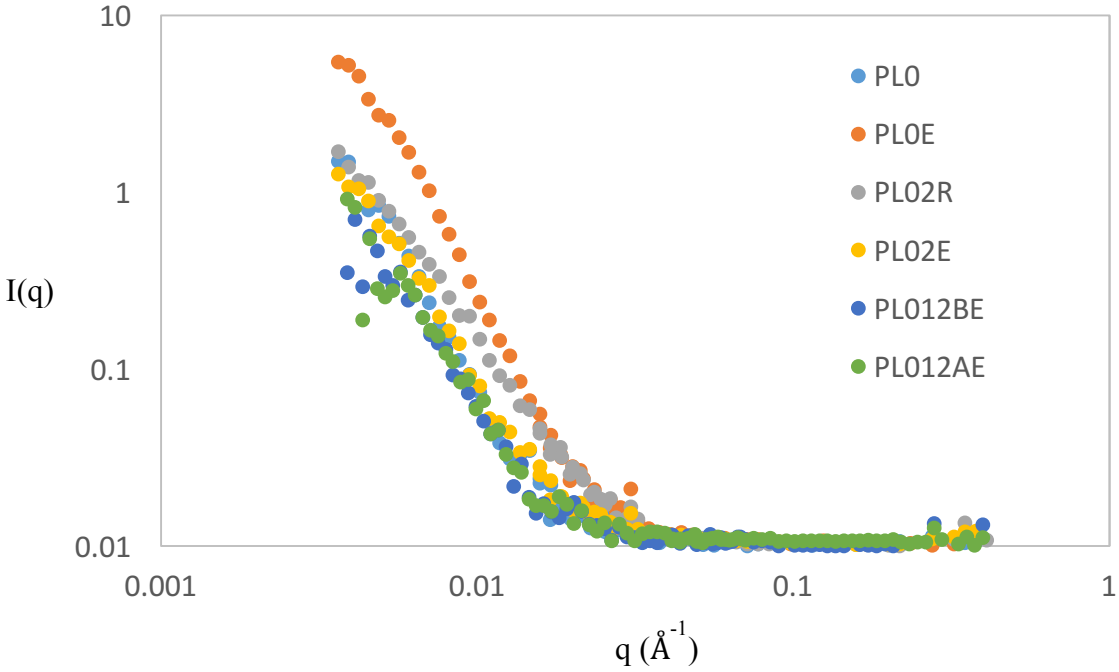

Figure 33. Scattering comparison plot authentic, PAD and PBA labeled Pahokee Peat L_0

Similar to Leonardite the Pahokee Peat HA_1 component shows a decrease in scattering intensity after emulsification (Figure 34). However, like all the components studied the shape of the scattering curves remain the same no matter what process is used on the samples. As with the Elliott Silt Loam the emulsified Pahokee Peat HA_2 component shown in Figure 35 shows a slight increase in scattering intensity until *q* reaches ~ 0.013 ($Å^{-1}$). Also the PL_1 (Figure 36) component just like EL_1 shows no definitive differences between the authentic PL_1 and the emulsified PL_{1E}. So again no assertions to how the emulsification process may or may not have affected this sample can be made.

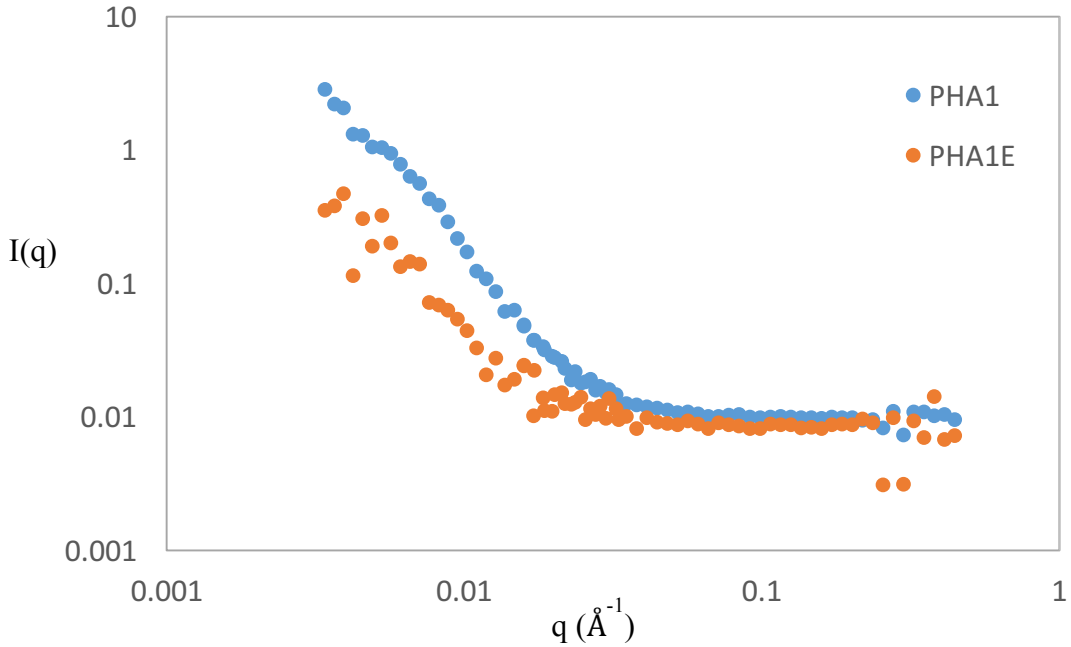

Figure 34. Scattering comparison plot authentic, emulsified Pahokee Peat HA_1

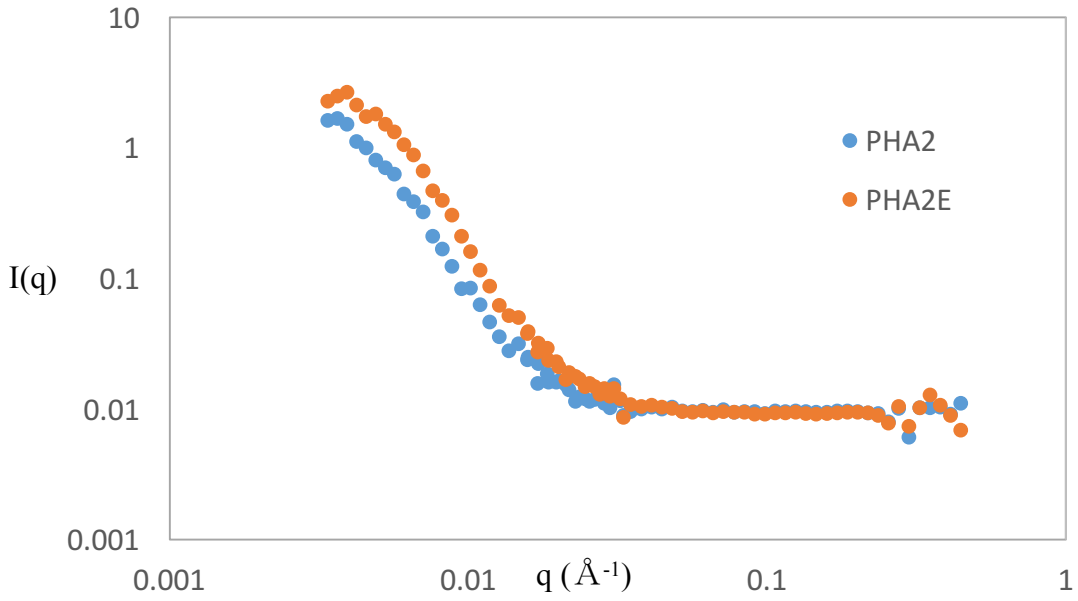

Figure 35. Scattering comparison plot authentic, emulsified Pahokee Peat HA_2

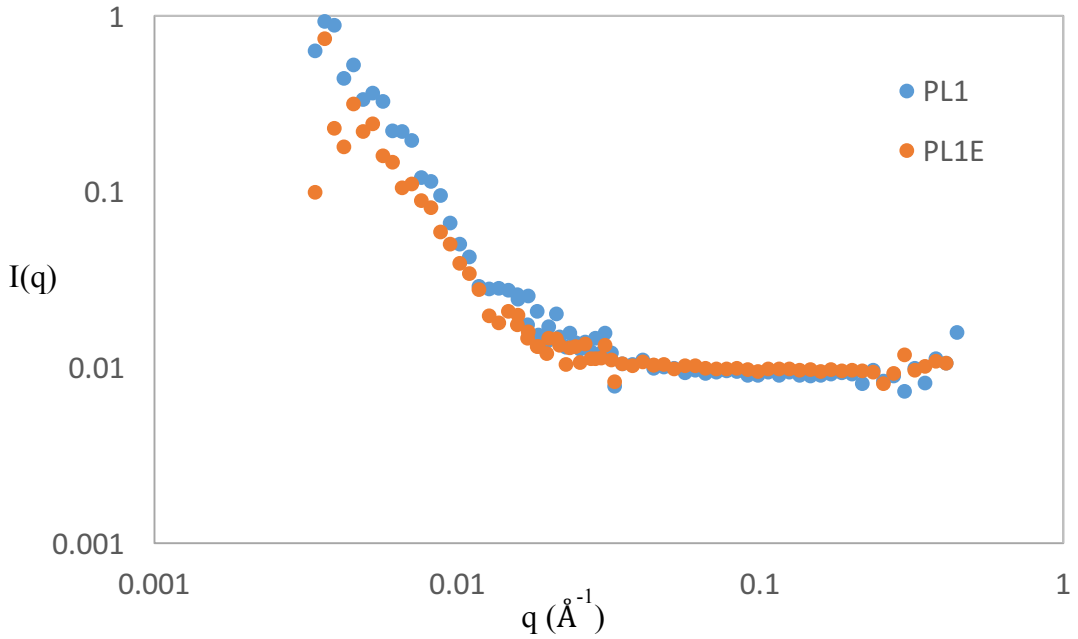

Figure 36. Scattering comparison plot authentic, and emulsified Pahokee Peat L_1

Fractal Dimension Determination

Figure 37 is the determination of the fractal dimension of PHA_0 and is a representative plot for all components studied. The experimentally determined ***D*** values are listed in Table 11 for authentic components and Table 12 for emulsified, recombined and labeled components.

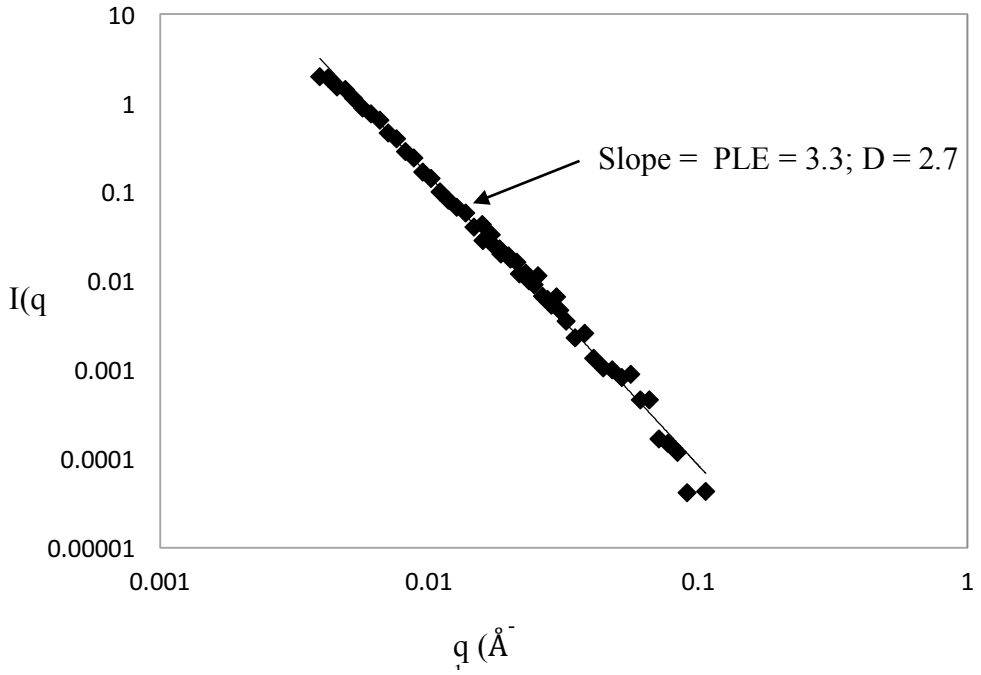

Figure 37. Scattering profile PHA_0

Shape Determination (Surface-to-volume ratios (S/V)

Surface to volume ratios have been used to determine the approximate shape and relative size for all components. Due to the inverse relationship of S/V ratios a decrease in size increases the surface-to-volume ratio. The value of the S/V ratio also are indicative of particle shape. Meaning that a S/V of 0.3 indicates a flat particle shape, whereas the

values of 0.1 and 0.06 correlate to spheres and disk shapes, respectively.[69] Table 11 lists the S/V values calculated for the authentic components using Equation 11. The S/V values range from 0.03 – 0.28 which also indicates the presence of disk-like structures, sphere-like aggregates, and particles that approach the flat shape value of 0.3.

As shown in Table 11 the distortion is more prominent in the lower level components which suggests that of HA_2 and L_1, and in the case of Elliott Silt Loam and possible Pahokee Peat the L_0 composites, are more elongated disks to flat in shape than the more spherical to disk-like upper level components of all materials HA_1, HA_0, and Leonardite L_0. The large differences in S/V values seen in Table 11 may be attributed to polydispersity of the particles in solution and that the diffusion of the largest particles may be anisotropic. More specifically it can be assumed that the particles are asymmetric given their aforementioned heterogeneous nature. Van Saarloos[122] suggested although aggregates that are heterogeneous will be oriented randomly around the scattering vector, $\boldsymbol{q}$, it may be possible that the initial decay seen in the scattering intensities is dominated by those aggregates whose D values are large along the direction of $\boldsymbol{q}$, which in turn will make the R_H value in that direction small. The opposite affect can also be assumed. If the D values along the direction of $\boldsymbol{q}$ are small due to a system containing mostly larger asymmetric aggregates like HA_1 and HA_0 their respective R_H values will be large, meaning that the corresponding S/V values will be large.

Table 11. – Experimentally determined Power-law exponenets (PLE) Fractal dimension (D), Hydrodynamic Radii (R_H) and Surface-to-volume ratio's (S/V) and associated shape assessments for authentic materials studied. Absolute uncertainty associated with each power-law exponent is ± 0.1.

Leonardite	PLE	**D**	**R_H (Å)****	**S/V****	**Shape**
HA_0	2.7	2.7*	49	0.06	Disk
HA_1	3.1	2.9	95	0.03	Disk
L_0	3.7	2.3	12	0.08	Disk
HA_2	3.2	2.8	38	0.24	Elongated sphere to flat
L_1	1.6	1.6*	27	0.13	Sphere
Elliott Silt Loam					
HA_0	3.4	2.6	105	0.03	Disk
HA_1	2.7	2.7*	130	0.02	Disk
L_0	3.0	3.0	101	0.18	Sphere
HA_2	3.3	2.7	11	0.03	Disk
L_1	2.5	2.5*	11	0.28	Elongated sphere to flat
Pahokee Peat					
HA_0	3.3	2.7	81	0.04	Disk
HA_1	3.1	2.9	81	0.04	Disk
L_0	3.0	3.0	24	0.14	Sphere
HA_2	3.6	2.4	21	0.13	Sphere
L_1	2.9	2.9*	48	0.06	Disk

* Indicates a mass fractal

** The R_H and S/V ratio values listed were calculated using Diffusion Coefficients determined by Pulsed Field Gradient NMR.

Authentic NOM Samples

As seen in Tables 11 the majority of NOM samples are surface fractals as represented in Figure 18a having power-law exponents that satisfy Eq. 14. In contrast, the L_1 components of all three materials have D values ranging from 1.6-2.9 that satisfy Eq. 13. Indicating that this lower level component has a more open arrangement as shown in

Figure 18b. Previously studied humic substances have demonstrated mass fractal characteristics in solution and surface fractal character in the solid state.[118]

Table 12. Experimentally determined Power-law exponenets (PLE) and Fractal Dimension (D) values for emulsified, recombined and labled components of NOM. Absolute uncertainty associated with each power-law exponent is ± 0.1.

	Leonardite		Elliott Silt Loam		Pahokee Peat	
Sample	**PLE**	**D**	**PLE**	**D**	**PLE**	**D**
HA_{0E}	3.1	2.9	2.8	2.8*	2.8	2.8*
HA_{02R}	3.5	2.5	3.1	2.9	2.6	2.6*
HA_{02E}	3.2	2.8	3.1	2.9	2.9	2.9*
HA_{03R}	2.3	2.3*	3.0	3.0	2.9	2.9*
HA_{03E}	3.2	2.8	3.3	2.7	2.6	2.6*
HA_{010BE}	3.3	2.7	3.2	2.8	2.4	2.4*
HA_{010AE}	2.7	2.7*	2.1	2.1*	2.8	2.8*
HA_{1E}	2.8	2.8*	2.8	2.8*	3.1	2.9
HA_{2E}	3.2	2.8	3.3	2.7	3.8	2.2
L_{0E}	3.8	2.2	2.5	2.5*	3.2	2.8
L_{02R}	3.7	2.3	3.4	2.6	3.0	3.0
L_{02E}	3.1	2.9	3.5	2.5	2.6	2.6*
L_{012BE}	3.2	2.8	3.1	2.9	2.5	2.5*
L_{012AE}	2.8	2.8*	2.9	2.9*	2.3	2.3*
L_{1E}	2.4	2.4*	2.5	2.5*	2.8	2.8*

* Indicates a mass fractal

However, the previous ***D*** values have been obtained for the unfractionated whole humic acid. It has been determined that L_1 is highly aliphatic,[77] therefore it is plausible that once fractionated this component has a fractal dimension very different form the original assembly. With the exception of Leonardite L_1 (***D*** = 1.6) all authentic components have ***D*** values which indicate RLA is the more prominent method of aggregation for NOM, meaning an increase in concentration will increase the possibility for aggregation due to more particle collisions. This would agree with data obtained by Guetzloff & Rice[57]

which determined that NOM forms micelles at increased concentrations. The Leonardite L_1 components ***D*** value indicates it has far more mass fractal like character than any other component studied and it has a S/V value (0.13) that indicates it is spherical. These findings suggest that unlike the other components fractionated Leonardite L_1 may aggregate by Diffusion-Limited aggregation (DLA)[123] Meaning that aggregation for this component occurs primarily due to Brownian motion. This type of random walk motion prevents particles of the component from penetrating deep into the interior of a cluster due to collisions that occur with the growing arms of the aggregate, resulting in a very open architecture.[124]

Similar to asphaltenes and resins, [125,126] NOM exists as mass fractals in solution and surface fractals in the solid form with shapes that range from somewhat flat disk-like (polydisperse spherical[127]) particles to more compact spherical[128] aggregates whose assembly is improved by an increase concentration in solution. A change in pH has also been shown to influence RLA and hence, the ***D*** values of NOM. It has been shown that changing the pH of a solution of NOM from 3-7 changes the obtained value of ***D***.[108] An increase in pH from 3-5 increases the ***D*** value suggesting a more space filling particle, however further increases in pH from 5-7 causes the ***D*** value to decrease.[119] Because the samples studied here were maintained at a pH of 5 prior to drying onto quartz disks the data obtained in this study would agree with this previous finding. It has been said that at pH 5 there are still negatively charged functional groups which attribute to the repulsive barrier that must be overcome for RLA to occur.[129]

Emulsified, Recombined and Labeled Samples

The descriptions of the emulsified, recombined and labeled samples are listed in Table 10. These samples were developed to examine if the emulsification process previously developed[88] affects the reassembly of the fractionated component of NOM. Although the addition of PBA and PAD only increased the scattering intensity of Elliott Silt Loam L_0 composite, the labeling of both HA_0 and L_0 with PAD (HA_{010AE} and L_{012AE}) did seem to highlight the aliphatic nature of the L_1 components giving D values in the mass fractal region similar to those of the both the authentic and emulsified unlabeled L_1 components. In addition, the emulsified samples of HA_0 and L_0 labeled with PBA (HA_{010BE} and L_{012BE}) also seemed to highlight the amphiphilic nature of HA_2 giving D values very similar to the authentic and emulsified samples for Leonardite and Elliott Silt loam materials. This same similarity was seen between the emulsified and the authentic Pahokee Peat L_0 samples, however the D values of the PBA emulsified labeled and authentic Pahokee Peat samples showed no similarity.

5.4 CONCLUSIONS

Comparisons of scattering intensities were inconsistent between material types and were not greatly affected by the emulsification, recombination or labeling processes for the majority of components studied, the only exceptions to this were the emulsification of LL_1 and LH_{A2}. Fractal dimension values seen in the majority of authentic NOM components indicate they are surface fractals with the exception of the L_1 component

which was determined to be a mass fractal for all materials studied. This was also the case for the emulsified components of Leonardite and Elliott Silt Loam, but this trend was not seen in the Pahokee Peat samples that when emulsified formed more loosely associated assemblies than the authentic material. This difference may be due to Pahokee peat having a higher percentage of carboxylic acids in its total organic carbon profile than either Leonardite or Elliott Silt Loam (18%, 8% and 10%, respectively – See Table 5 in Chapter 3). This may contribute to the disruption of its authentic organization due to the acidic H_2O used during the final step of the emulsification process. Carboxylic acids can hydrogen bond, and contain both a hydrogen bond acceptor and a donor. Therefore, it is possible to form highly stable dimers between carboxylic acids which would then create an assembly more loosely associated than the authentic HA_0. If this is indeed the case, it occurs in Leonardite and Elliott Silt Loam as well, just not to the extent that it affects Pahokee Peat. In addition, the obtained fractal dimension values for the emulsified, recombined, and authentic components indicate that NOM self-assembles via a reaction limited aggregation process that takes place more slowly than diffusion limited aggregation due to the need to overcome an energy barrier present which has been said previously to be associated with de-protonated carboxylate groups at pH ~ 5. This also agrees with the findings of Perdue [130] who quantified the acidic functional groups of NOM through direct acid/base titration using the typical deprotonation reactions for carboxylic acids. Furthermore, the R_H values calculated from the diffusion coefficients obtained using Pulsed Field Gradient NMR indicate that the lower level components of

NOM are smaller relative to HA_1 and HA_0 with the HA_1 component consistently being the largest for all material types studied. The fractal dimension values, surface-to-volume-ratios, and hydrodynamic radii determined experimentally indicate the components of NOM are a mixture of polydisperse spheres to somewhat flat particles. More specifically the lower level components of NOM may be further described as oblate/prolate ellipsoids or flat particles, while the upper level components consistently demonstrated a much larger more disk-like shape.

CHAPTER 6

MODELS OF THE ARCHITECTURE OF NATURAL ORGANIC MATTER

6.1 INTRODUCTION

As discussed in Chapter 1.4, historically there have been basically two types of models proposed regarding the architecture of NOM. The polymer models suggests that humus comprises products created from secondary synthesis reactions that alter the original organization of the plant material that are believed to be polymeric species with chemical characteristics distinctly different from the starting material[36]. These models also assumed that humus were heterogeneous mixtures of high molecular weight polymers.[9] Therefore, giving mixtures of highly cross-linked polymers of differing molecular weights. This led to the belief in the possibility that the organization of the three humic substances (humin, humic acid, and fulvic acid) could be generalized by a structural diagram of covalently bonded functional groups similar to the represented chemical structure of lignin.

The molecular aggregate models claim that NOM is a complex mixture resulting from the degradation of plant material and microbial remnants. The solubility differences seen in the different components of NOM would then be the result of varying molecular weight and charge densities. The molecular aggregate models stem from the inclusion of partially degraded products of plant polymers held together by non-covalent bonds.[37,38]

However, the architecture of NOM cannot be fully explored without the inclusion of the architectural model for asphaltenes as discussed in Chapter 1.4.

The numerous similarities between NOM and asphaltenes and resins make it feasible that these two systems may be architecturally similar. Both materials (1) Comprise components that are operationally defined by their differing solubility's in solution. (2) Are known to self-assemble in the environment. (3) Contain amphiphilic components which form micelles with increasing concentration. (4) Are defined as surface and mass fractals having similar fractal dimension values. (5) Have been determined to have shapes that vary from disk-like particles to spherical shaped aggregates. In addition, to the aforementioned similarities these materials appear to be analogous geologically, given that NOM is a precursor to coal and asphaltenes and resins are precursors to petroleum.

6.2 EXPERIMENTAL RESULTS SUMMARY

The components of NOM obtained from three material types have been characterized in this investigation by ^{13}C solid state NMR, PFG NMR, and SANS. The results and the corresponding interpretations are shown in Table 13 and are discussed in the following sub-sections in an attempt to propose a model for the architecture of NOM.

Table 13. Summary of Experimental Results Related to Size, Shape and Architecture

NOM component	*Hydrodynamic Radius range	*Surface:Volume Ratio (***S/V***)	Fractal Dimension (***D***) Range
HA_0	48 - 105 Slightly smaller than HA_1	0.03 -0.06 Disks	2.6 -2.7 Slightly to highly space filling
HA_1	81 - 130 Largest component	0.02 – 0.04 Disks	2.7 – 2.9 Slightly to highly space filling
L_0	12 - 100 Size dependent upon material type	0.08 – 0.18 Spherical to slightly distorted spheres	2.3 – 3.0 Loosely associated to highly space filling
HA_2	10 - 38 Size dependent upon material type	0.03 – 0.24 Distorted spheres to flat	2.4 – 2.8 Slightly to highly space filling
L_1	10 - 47 Size dependent upon material type	0.06 – 0.28 Distorted spheres to flat	1.6 -2.9 Loosely associated mass fractals

*Hydrodynamic radii and S/V ratios are only determined for authentic NOM samples

Due to the hierarchical nature of NOM the proposed model for NOM to be discussed herein will begin with the lowest level components (L_1 and HA_2), that create the intermediate composite component (L_0), continue with the upper level components (L_0 and HA_1) to finally conclude with the NOM assembly of HA_0.

The Architecture of L_1

Tables 13 summarizes the data collected for the L_1 component related to size and shape, respectively for all the materials studied and it can be concluded that the general shapes are distorted spheres or disks to flat with sizes that vary widely dependent upon material

type. The fractal dimension values indicate in general this component are loosely associated mass fractals. Because L_1 is primarily aliphatic (See Figures 3(e), 4(e), and 5(e)) it may be assumed that the shape may be dependent upon the number of aliphatic chain-like configurations that comprise the L_1 components for different material types. Table 11 shows the S/V ratio of Leonardite L_1 to be 0.13 indicating a slightly distorted spherical shape, a truly spherical molecule has a S/V value of 0.1, whereas a disk shaped (oblate/prolate spheres) molecule has a value of 0.06. In contrast with Leonardite L_1 the S/V values of Elliott Silt Loam and Pahokee Peat are 0.28 and 0.06, respectively, indicating a somewhat flat shape for Elliott Silt Loam and disk for Pahokee Peat. The architecture of these components can by compared with the behavior of some dendrimers, where a minimum number of chain-like structures assemble and create disk-like assemblies. The addition of supplementary chains of approximately the same length creates assemblies that are more spherical. Figure 38(a) demonstrates how L_1 may exist as an oblate or prolate sphere due to the interactions of aliphatic chains, and Figure 38(b) is a representation of a component with additional aliphatic chains creating molecule that is more flat than in Figure 38(a). This representation is simply an indication of the highly aliphatic nature of L_1 and the shape(s) as indicated by SANS data and by no means is an assumption of complete saturation of the carbon chains. Although L_1 is highly aliphatic there is still a small resonance seen in the aromatic and carboxylate regions in Figures 3 (e), 4(e) and 5(e) which gives this possibility of hydrogen bonding and π-π interactions with HA_2 to form the L_0 composite.

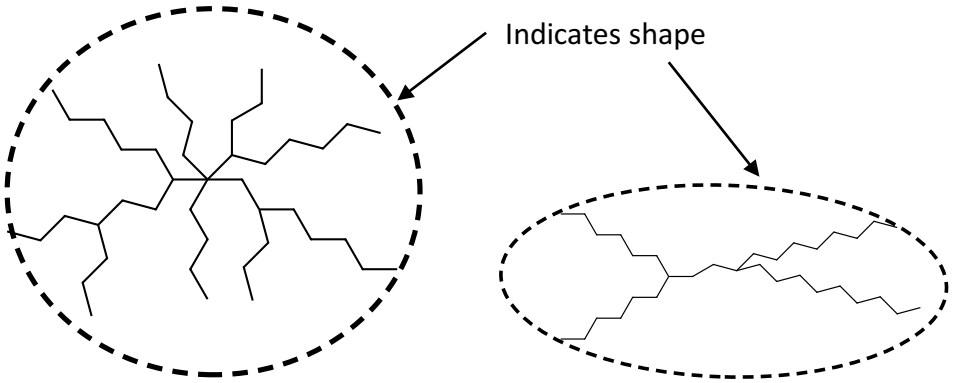

(a) (b)

Figure 38. Proposed architecture of L_1

The Architecture of HA_2

Table 11 shows S/V values for Leonardite, Elliott Silt Loam and Pahokee Peat HA_2's to be 0.24, 0.03, and 0.13 respectively. As with L_1 the data in Table 13 for HA_2 concludes that the general shapes are oblate/prolate spheres or actual spheres with sizes that vary widely dependent upon material type. The fractal dimension values listed in Table 13 indicate in general this component are surface fractals that are slightly to highly space filling dependent again upon material type. The proposed architecture for the HA_2 component is shown in Figure 39. Because HA_2 is an amphiphile (See Figures 3(c), 4(c), and 5(c)) containing carboxylic acids aromatics and aliphatic components, and has demonstrated amphiphilic behavior in surface tension studies[39] structural possibilities include aromatics with polar groups in association with aliphatic components containing both polar and non-polar regions within the molecule.

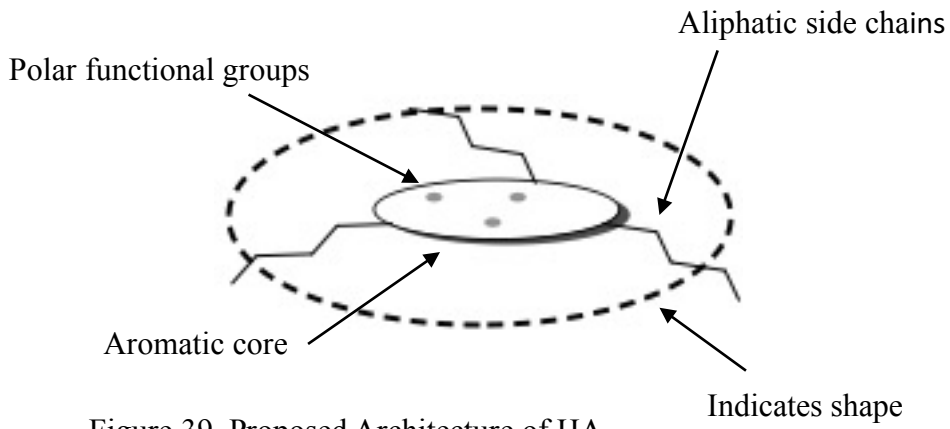

Figure 39. Proposed Architecture of HA_2

The Architecture of L_0

The composite L_0 created through the interaction of HA_2 and L_1 is a surface fractal for all materials studied, having PLE values great than 3 which give D values of 2.3, 3.0, and 3.0 for Leonardite, Elliott Silt Loam and Pahokee Peat, respectively. Indicating that this composite has a space filling architecture with a rough surface. As with L_1 and HA_2 the data in Table 13 for L_0 conclude that the general shapes are distorted spheres or actual spheres with sizes that vary widely dependent upon material type. Table 11 shows S/V values for Leonardite, Elliott Silt Loam and Pahokee Peat L_0's to be 0.08, 0.18, and 0.14 respectively, signifying Leonardite to be a disk, while Pahokee Peat and Elliott Silt Loam are only slightly distorted from an actual sphere. The data indicate polydispersity with the corresponding components between materials, as well as within the materials themselves, which is to be expected with a heterogeneous mixture. Figure 40 is a

representation of the possible architecture occurring from the self-assembly of HA_2 and L_1. The aliphatic chains of L_1 serve to link together the HA_2 molecules forming an assembly with ^{13}C solid state NMR chemical shifts similar to HA_2, (See Figures 3(d), 4(d), and 5(d)) albeit with a stronger resonance in the ether and ester regions. With the natural abundance of HA_2:L_1 being (70:30), (70:30), and (65:35) for Leonardite, Elliott Silt Loam, and Pahokee Peat, respectively the similarity in ^{13}C solid-state spectra is not surprising. Given that Leonardite L_0 is a surface fractal like HA_2, however Leonardite with a ***D*** value of 2.3 has a much rougher and more planar surface that Elliott Silt Loam and Pahokee Peat (***D's = 3.0)***. As seen in Figure 3(d) Leonardite's resonance in the chemical shift region of carbohydrates (50 -108 ppm) is significantly lower than the corresponding carbohydrate regions of Elliot Silt Loam and Pahokee peat (Figures 4(d) and 5(d).

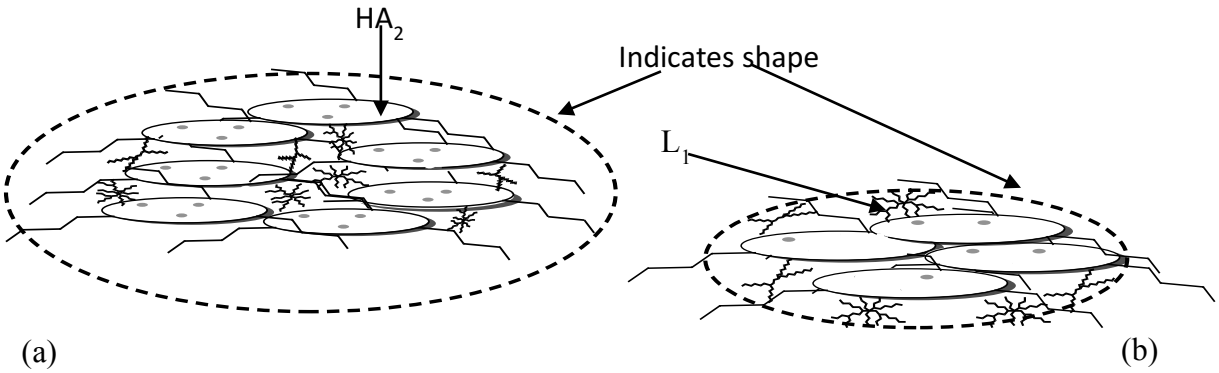

Figure 40. Proposed architecture of L_0 (a) Elliott Silt Loam and Pahokee Peat (b) Leonardite

The Architecture of HA_1

The proposed architecture for HA_1 is shown in Figure 41. The non-amphiphilic component of NOM is highly aromatic with a smaller resonances seen in the aliphatic and carboxylate regions as shown in Figures 3(b), 4(b), and 5(b). This component is the largest of all the components for all the materials studied as indicated by the hydrodynamic radius, and diffusion coefficients listed in Table 13. Unlike the lower level components, the data in Table 13 for HA_1 conclude that the general shapes are spherical to only slightly distorted spheres with sizes that are similar across all material types. Table 11 shows S/V values for Leonardite, Elliott Silt Loam and Pahokee Peat HA_1's to be 0.03, 0.02, and 0.04 respectively, signifying that HA_1's for all materials studied have disk-like shapes.

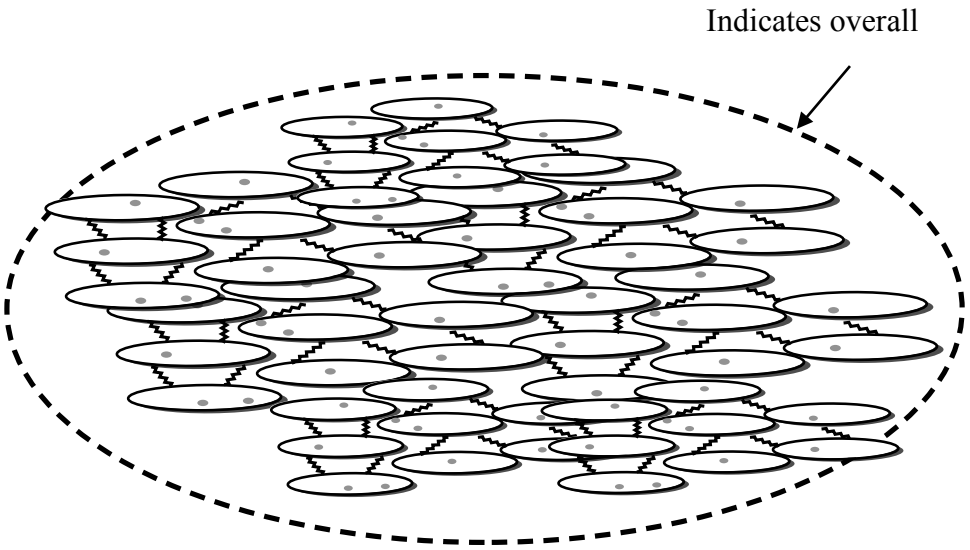

Figure 41. Proposed Architecture of

The Architecture of HA_0

The final assembled HA_0's are spherical to only slightly distorted, slightly to highly space filling disks, with sizes that are similar across all material types as shown by the data in Table 13. This component is the consistently somewhat smaller than HA_1 for all the materials studied as indicated by hydrodynamic radius, and diffusion coefficients listed in Table 13. Table 11 shows S/V values for Leonardite, Elliott Silt Loam and Pahokee Peat HA_0's to be 0.06, 0.03, and 0.04 respectively, signifying a disk like shape for the final assembly for all materials studied.

Like HA_2, HA_0 is surface active (See Figures 3(a), 4(a), and 5(a)) containing carboxylic acids aromatics and aliphatic components, and has demonstrated amphiphilic behavior in surface tension studies.[39] Therefore, the structural possibilities include aromatics with polar groups in association with aliphatic components containing both polar and non-polar regions within the molecule. Figure 42 is a proposed representation of the self-assembled architecture of HA_0 for the materials. Given the smaller relative size of HA_0 to HA_1 is can be assumed that the L_0 incorporates itself into the configuration of HA_1 causing the final assembly to draw the aromatic components closer together through van der Waals interactions, π-π interactions, and additional hydrogen bonding. Although the HA_1:L_0 ratios are 70:30, 90:10, and 80:20 for Leonardite, Elliott Silt Loam, and Pahokee

Peat, respectively this reduction in size occurs for all materials investigated herein. Albeit the reduction in size does vary dependent upon material type with Leonardite showing a 50 % reduction, Elliott Silt Loam a 20% reduction and only a 5% reduction for Pahokee Peat.

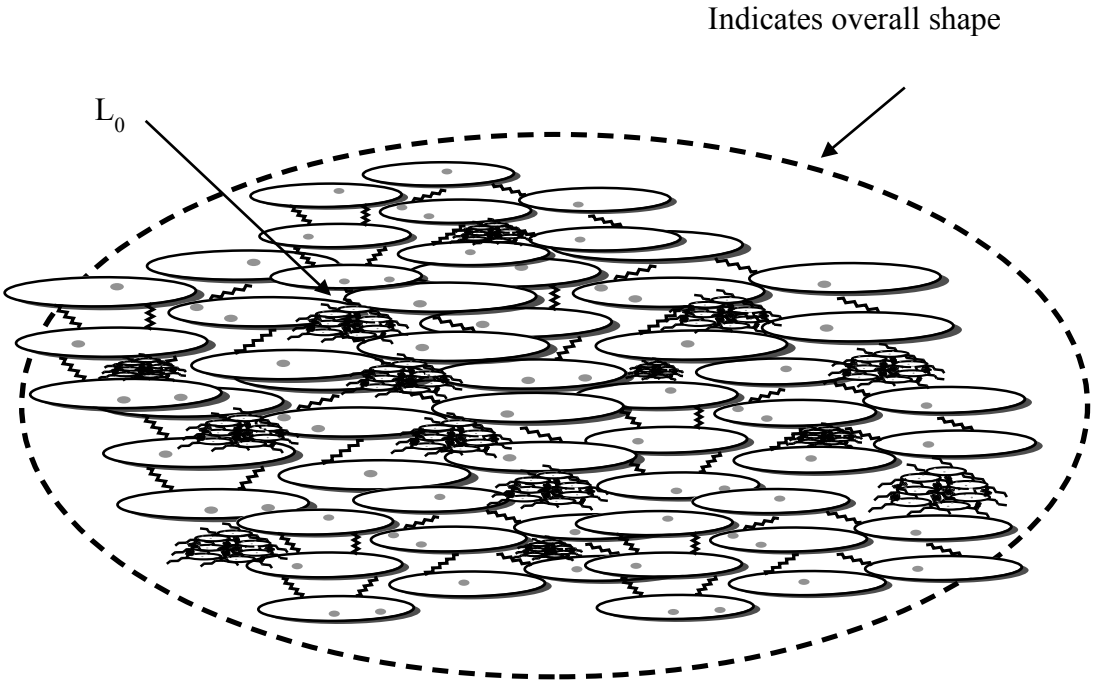

Figure 42. Proposed architecture of HA_0

6.3 Proposed Architecture of NOM

Although there are many differences between the values of the previously discussed size and shape parameters of the lower level components among the material types, the upper level components have similar values (surface-to-volume, hydrodynamic radii, diffusion coefficients, and fractal dimension) for the final assembly of HA_0. It is important to

recognize the differences in carbon content between the material types which in this investigation range from a soft coal containing ~ 70% organic carbon, a peat soil with organic carbon content ~50%, and a typical agriculture soil which has only ~ 4% organic carbon. This vast difference in carbon content does not seem to affect the general characteristics of NOM or how it self-assembles in the environment.

As discussed in Chapter 1.4 the Modified Yen model[70] focuses on an asphaltenes architecture consisting of a single, moderately large polyaromatic hydrocarbon ring system with peripheral alkanes which forms nanoaggregates with aggregations numbers of approximately six. The interior consists of a single disordered stack surrounded with peripheral alkanes. These nanoaggregates then form clusters with aggregations numbers of approximately eight. Although the number of aggregates are unknown for the self-assembly of NOM the Modified Yen Model[70] closely resembles the molecular aggregate model proposed by Wershaw.[43] Both of these systems contain a hierarchy of components that aggregate to form a composite or nanoaggregate which then interacts with another component to form the final assembly, and have been shown to form micelles in solution.[55,57] Furthermore, Wershaw proposed that higher level components of NOM consist of aggregates of amphiphiles with acidic functionality intrinsically stabilized by non-covalent weak forces such as dispersive hydrophobic interactions and hydrogen bonds.[44,45] As displayed in Figure 43 it is the combination of these two ideas that is proposed for the self-assembled architecture of NOM herein.

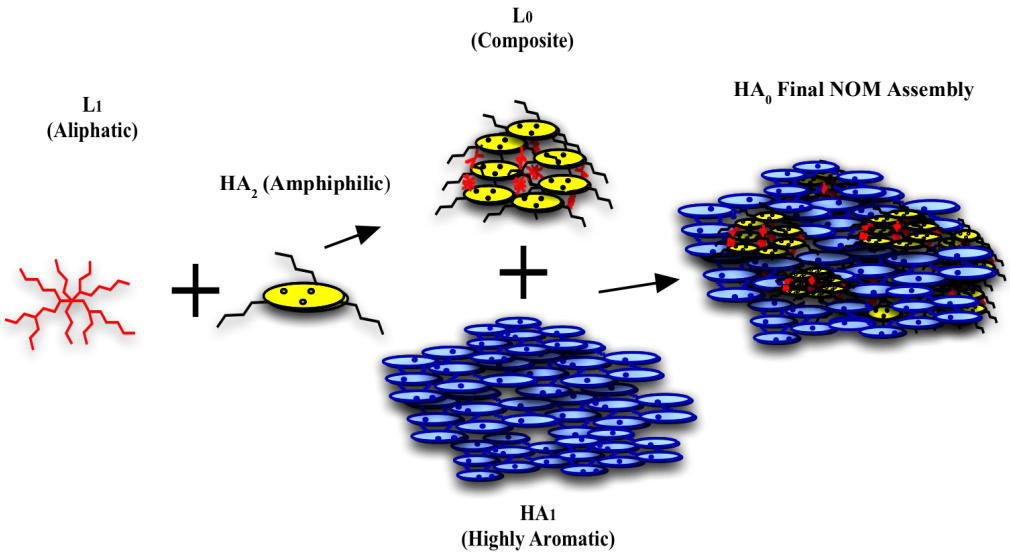

Figure 43. Self-Assembly of NOM components

Natural organic matter and bitumen are naturally occurring materials created through the geochemical processes of the Earth. Both also comprise components that are operational defined by their solubility characteristics. In addition, these materials form aggregates through self-assembly, therefore the conclusion that there are startling similarities between the self-assembly and architecture of NOM and asphaltenes and resins is not surprising. These similarities and the results obtained throughout this investigation lead to conclusion that the architecture of these two materials are comparable and can be generally represented by Figure 51.

6.4 Future Work

The ability to more closely examine the molecular aggregation of NOM is essential to understanding what may be possible to further enhance the sequestration of carbon in the soils of the Earth. Ultra-Small-Angle Neutron (USANS) scattering is commonly used to study hierarchical organization in both natural and artificial materials. The scattering profiles herein consistently have high scattering intensities at the lower limit of the ***q***-range studied. Suggesting the need to look at NOM at a smaller ***q***-angle to provide more accurate data regarding particle size and shape. USANS with a ***q*** range of 7×10^{-6} Å < q 5×10^{-3} Å is used in the study of aggregation in colloid dispersions, macroscale self-similarity of rock, the structure of colloidal crystals and alloys, and the self-assembling and supramolecular structure of polymers and polymer blends. Rather than in solution, NOM samples assessed by USANS should be powders to enhance signal intensity to enable more extensive data reduction and interpretation. In addition, an investigation using SANS with liquid NOM samples of varying pH would provide data regarding the type of aggregation (DLA or RLA) more likely to occur in the environment.

In an effort to enhance the model of NOM proposed here, Heteronuclear Single Quantum Coherence spectroscopy (HSQC) to examine unique protons attached to carbon wouldhelp establish more specific functional groups for the components of NOM. The organization of NOM can be identified and characterize with Heteronuclear Multiple

Bond Correlation Spectroscopy (HMBC) which provides information about carbons bonded to protons which are 2-3 bonds away.These experiments would provide valuable information which could be used to further specify a more detailed description of the self-assembled architecture of NOM.

APPENDIX

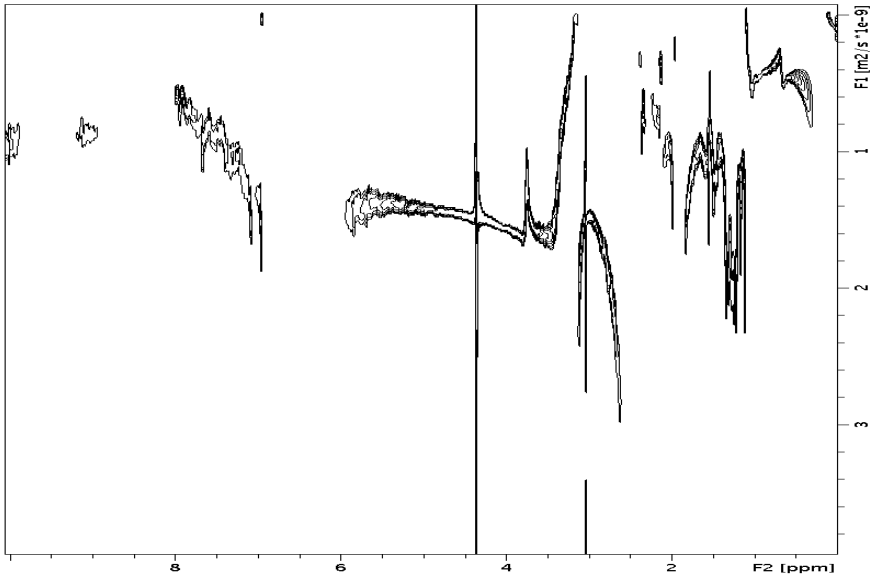

Figure A.1. DOSY spectrum of authentic Pahokee Peat HA_2

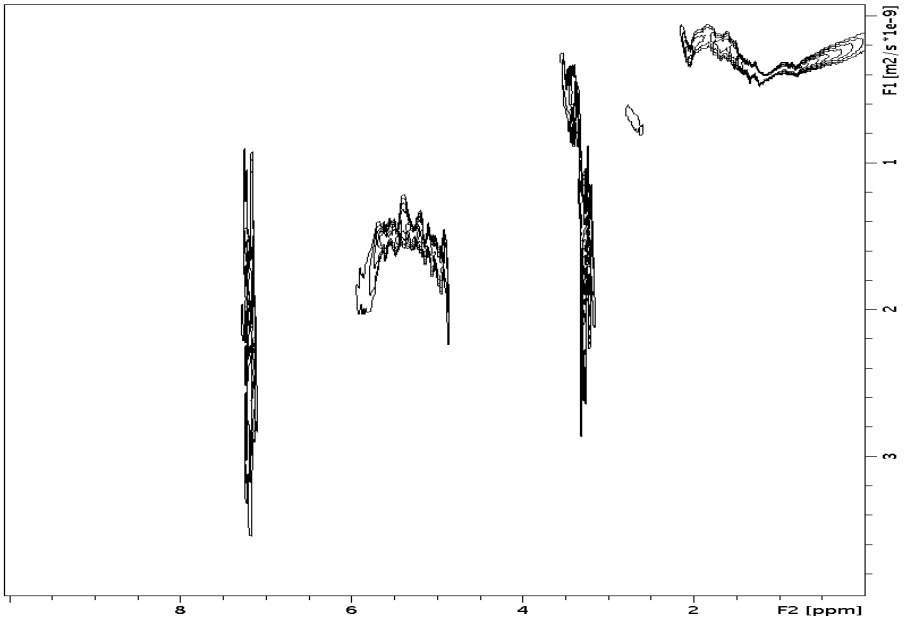

Figure A.2. DOSY spectrum of authentic Pahokee Peat L_1

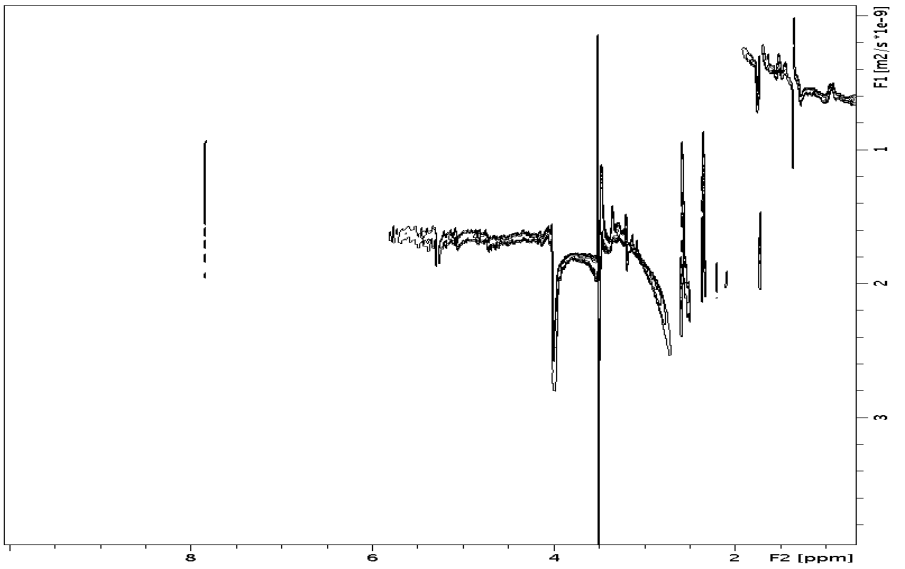

Figure A.3. DOSY spectrum of authentic Pahokee Peat L_0

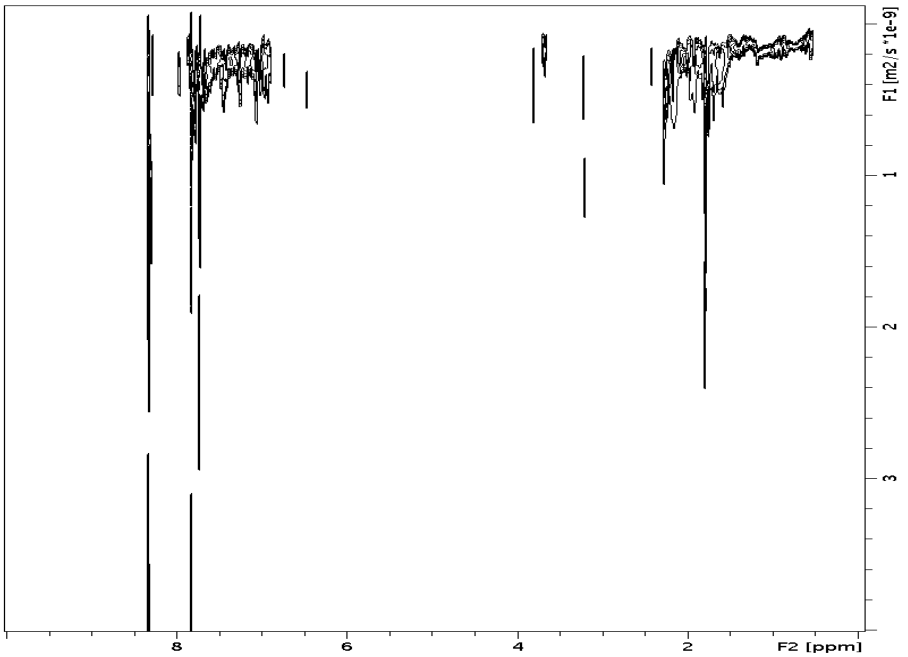

Figure A.4 . DOSY spectrum of authentic Pahokee Peat HA_0

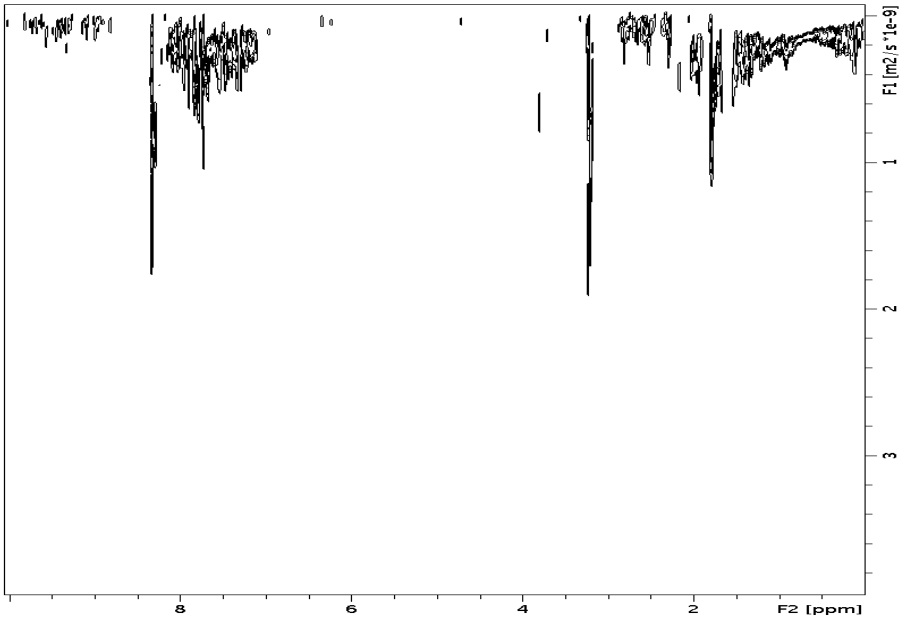

Figure A.5. DOSY spectrum of authentic Pahokee Peat HA_1

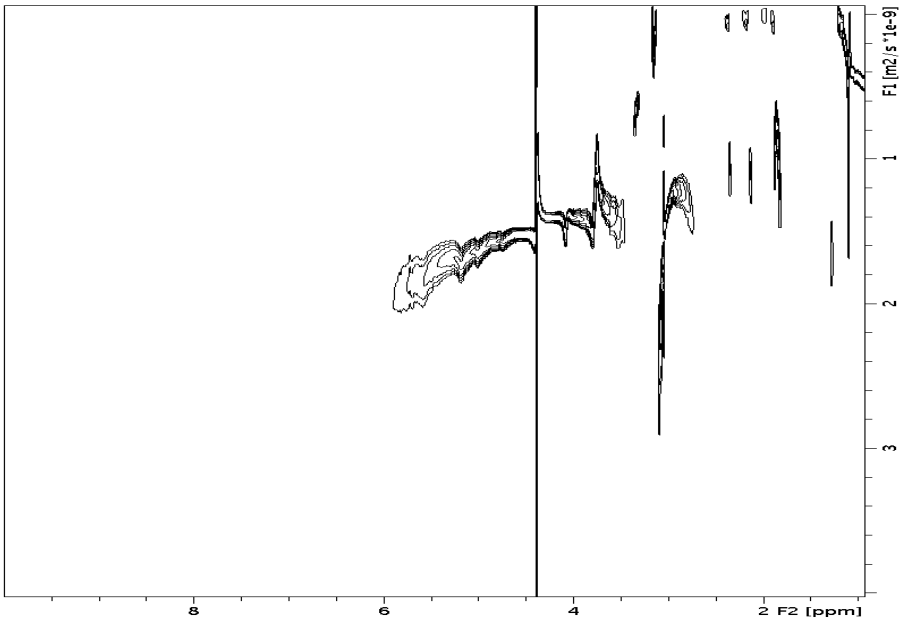

Figure A.6. DOSY Spectrum of authentic Leonardite L_1

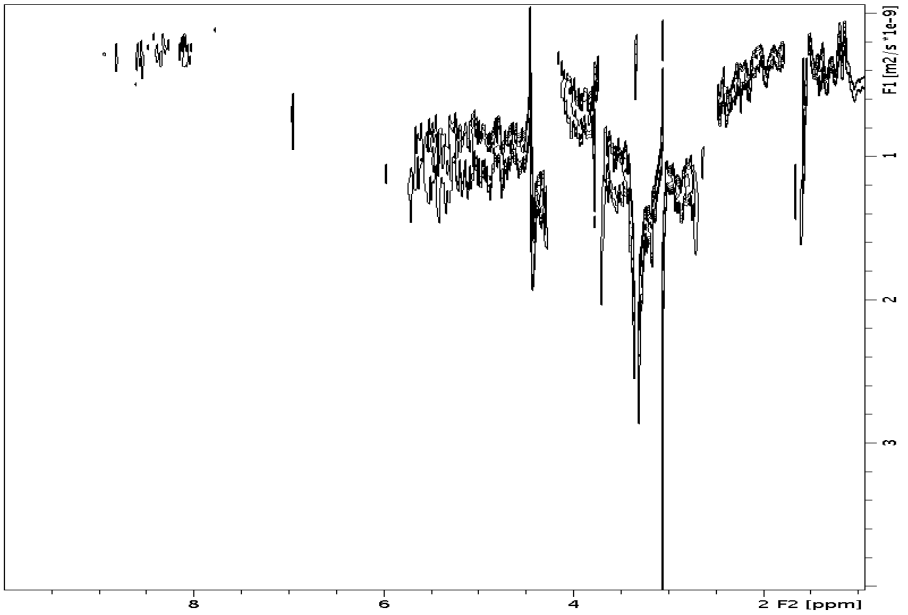

Figure A.7. DOSY spectrum of authentic Leonardite HA_2

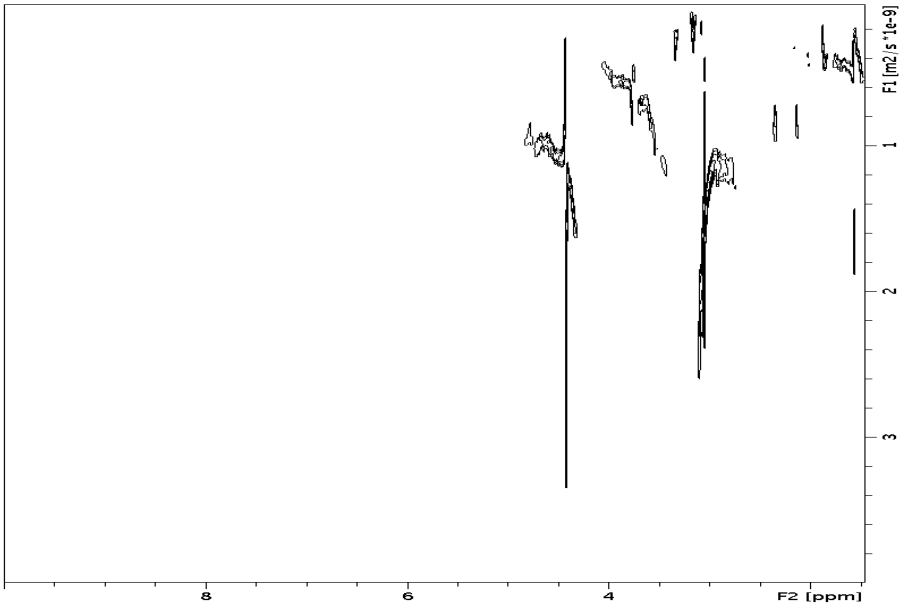

Figure A.8. DOSY spectrum of authentic Leonardite L_0

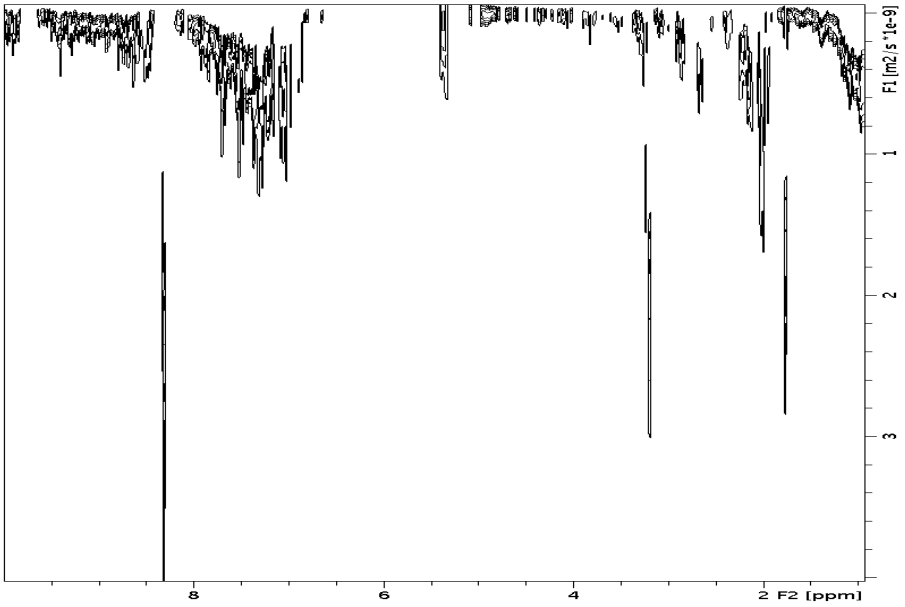

Figure A.9. DOSY spectrum of authentic Leonardite HA_1

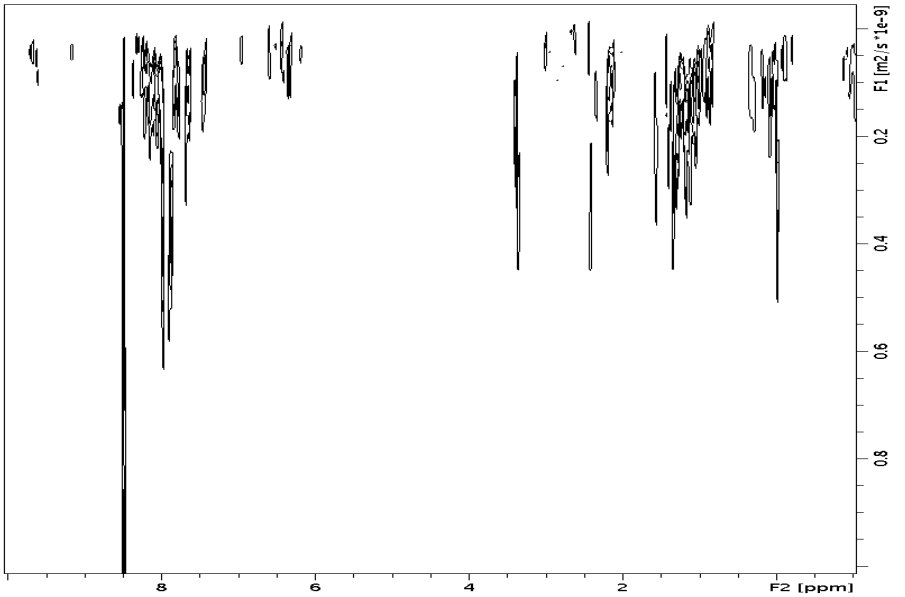

Figure A.10. DOSY spectrum of authentic Leonardite HA_0

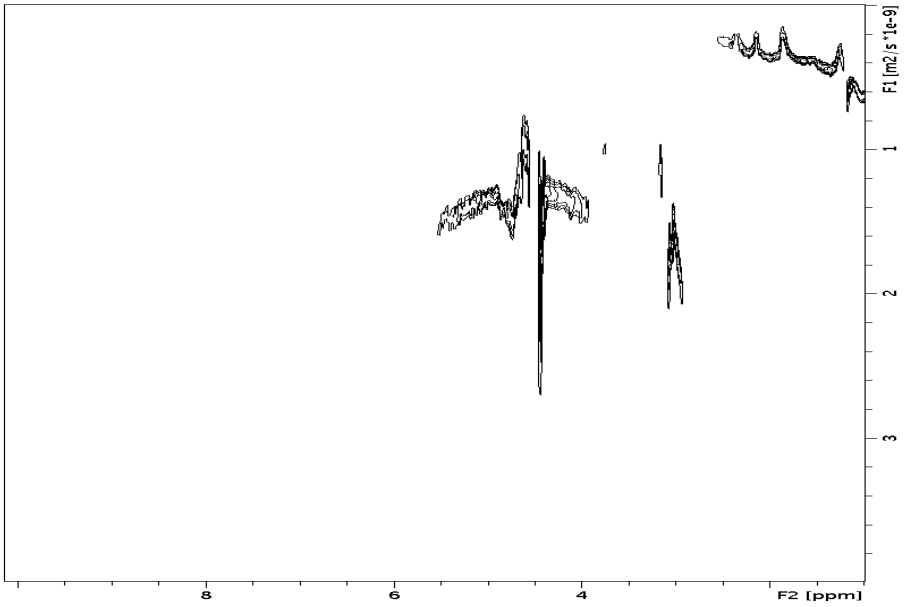

Figure A.11. DOSY spectrum of authentic Elliott Silt Loam L_1

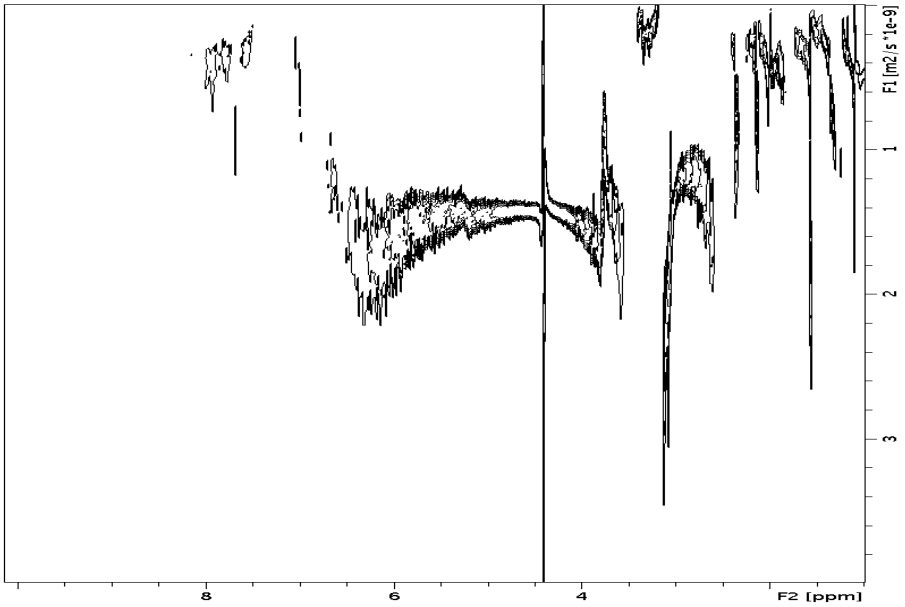

Figure A.12. DOSY spectrum of authentic Elliott Silt Loam HA_2

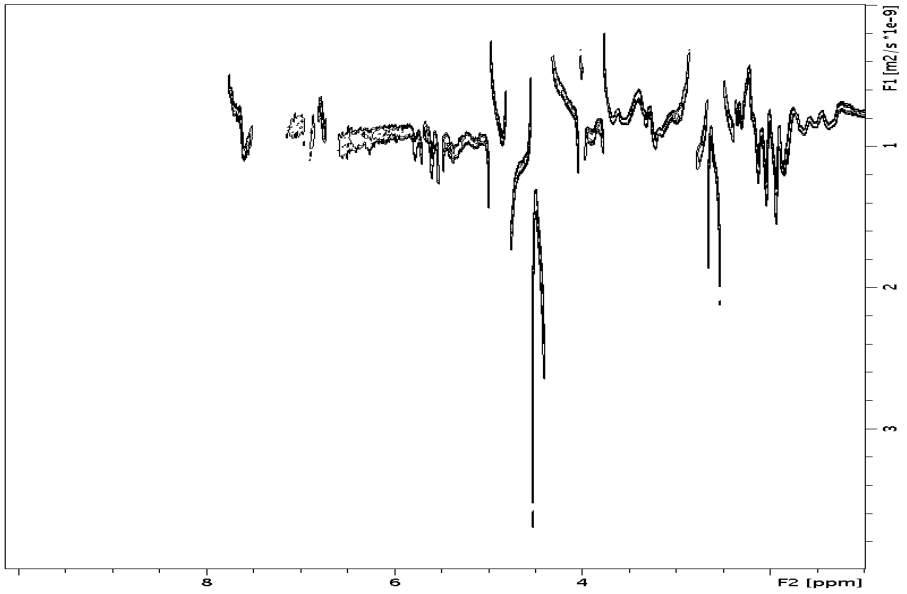

Figure A.13. DOSY spectrum of authentic Elliott Silt Loam L_0

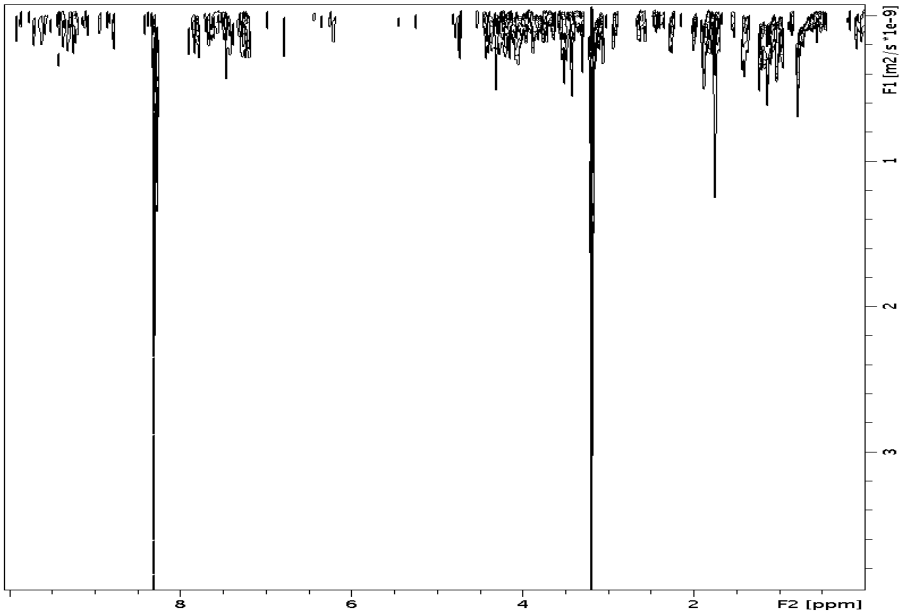

Figure A.14. DOSY spectrum of authentic Elliott Silt Loam HA_1

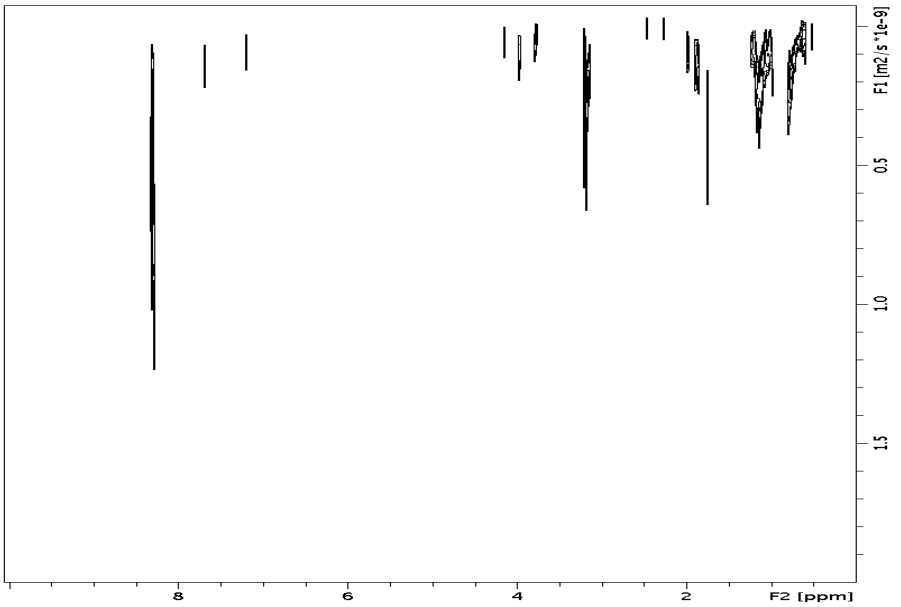

Figure A.15. DOSY spectrum of authentic Elliott Silt Loam HA_0

BIBLIOGRAPHY

1. Stevenson, F. J., *Humus Chemistry*. Wiley & Sons: New York, New York, 1982.

2. Cambardella, C. A. E., E.T., Particulate Soil Organic-Matter Changes Across a Grassland Cultivation Sequence. *Soil Sci. Soc. Am. J.* **1992,** *56*, 777-783.

3. Cambardella, C. A. E., E.T., Carbon and Nitrogen Dynamics of Soil Organic Matter Fractions From Cultivated grassland Soils. *Soil Sci. Soc. Am. J.* **1994,** *58*, 123-130.

4. Wershaw, R. L., The Study of Humic Substances - In Search of a Paradigm. In *Humic Substances - Versitle Components of Plants, Soils and Water*, Davies, G., Ed. Cambridge, Royal Society of Chemistry: 2000; pp 1-7.

5. Six, J., Guggenberger, G., Paustian, K., Haumaier, L., Elliott, E. T., Zech, W., Sources and Composition of Soil Organic Matter Fractions Between Soil Aggregates. *European Journal of Soil Science* **2001,** *52*, 607-618.

6. Sohi, S. P., Mahieu, N., Arah, J. R. M., Powlson, D. S., Madari, B., Gaunt, J.L, A Procedure for Isolating Soil Organic Matter Fractions Suitable for Modeling. *Soil Sci. Soc. Am. J.* **2001,** *65*, 1121-1128.

7. Killops, S. K., Vanessa, *Introduction to Organic Geochemistry*. Blackwell Publishing: Malden MA, 2005.

8. Aiken, G. R., McKnight, D.M., Wershaw, R.L., MacCarthy, P., An introduction to humic substances in soil, sediment, and water. In *Humic substances in soil, sediment, and water*, John Wiley & Sons: 1985.

9. Kononova, M. M., *Soil Organic Matter*. 2 ed.; Pergamon Press: Oxford, 1966.

10. Tissot, B. P.; Welte, D. H., Diagenesis, Catagenesis and Metagenesis of Organic Matter. In *Petroleum Formation and Occurrence: A New Approach to Oil and Gas Exploration*, Springer Berlin Heidelberg: Berlin, Heidelberg, 1978; pp 69-73.

11. Stockman, U., et al., The knowns, known unknowns and the unknowns of sequestration of soil organic carbon. *Agricultural, Ecosystems and Environment* **2013,** *164*, 80-99.

12. Schlesinger, W. H., *Biogeochemistry: An Analysis of Global Change*. Acedemic Press: Oxford, UK, 1997.

13. Lal, R., Carbon Sequestration. *Philisophical Transaction of the Royal Society B Biological Sciences* **2008,** *363*, 815-830.

14. Piccolo, A., Humus and soil conservation. In *Humic Substances in Terrestrial Ecosystems*, Piccolo, A., Ed. Elsevier: Amsterdam, 1996.

15. Woodwell, G. M., Whittaker, R.H., Reiners, W.A., Likens, G.E., Delwiche, C.C., Botkin, D.B., The biota and the world carbon budget. *Science* **1987,** *199*, 141-146.

16. Lal, R., Soil Carbon Sequestration Impacts on Global Climate Change and Food Security. *Science* **2004,** *304* (5677), 1623-1627.

17. Brady, N. C., *The soil around us. The nature and properties of soils*. MacMillian Publishing Company: New York, 1990.

18. Waksman, S. A., *Humus Origin, Chemical Composition, and Importance in Nature*. Williams and Wilkins: Baltimore, MD, 1936.

19. Climate Change: Vital Signs of the Planet: Evidence. http://climate.nasa.gov/evidence/.

20. Petit, J. R. e. a., Climate and atmospheric history of the past 420,000 years from the Vostok ice core, Antarctica. *Nature* **1999,** *399*, 429-436.

21. Dlugokencky, E., Tans, P. www.esrl.noaa.gov/gmd/ccgg/trends/ (accessed June 27, 2016).

22. Annual mean growth rate of CO2 at Mauna Loa, HI. (accessed June 27, 2016).

23. Climate Forcings and Global Warming. http://earthobservatory.nasa.gov/Features/EnergyBalance/page7.php.

24. Peixoto, J., Oort, A., Radiation Balance. In *Physics of Climate*, American Institutes of Physics Press: Woodbury, NY, 1992; pp 91-130.

25. http://www.cru.uea.ac.uk/cru/data/temperature (accessed June, 30 2016).

26. Allison, I., et al., The Copenhagen Diagnosis: Updating teh World onthe Latest Climate Science. Sydney, Australia, 2009; p 11.

27. Peterson, T. C., et al., State of the Climate in 2008. *Special Supplement to the BUlletin of the AMerican MeterorologicalSociety* **2009,** *90* (8), S17-S18.

28. Marshall, J., Plumb, R. A., The Global Energy Balance. In *Atmosphere, Ocean, and Climate Dynamics: An Introductory Text*, Elsevier Acedemic Press: Oxford, UK, 2008; pp 9-22.

29. http://www.pmel.noaa.gov/co2/story/What+is+Ocean+Acidification%3F (accessed June 30, 2016).

30. http://www.pmel.noaa.gov/co2/story/Ocean+Acidification.

31. Polyak, L. e. a., History of Sea Ice inthe Arctic. Survey, U. S. G., Ed. Past Climate Variability and Change in the Arctic and at High Latitudes, 2009.

32. Tapley, B. D., Bettadpur, S., Watkins, M., Reigber, C., The gravity rcovery and climate experimnet: Mission overview and early results. *Geophys. Res. Lett.* **2004,** *31* (9), L09607.

33. Latest glacier mass balance data. http://wgms.ch/latest-glacier-mass-balance-data/ (accessed June, 30 2016).

34. Church, J. A., White, N.J., A 20th Century acceleration in global sea level rise. *Geophys. Res. Lett.* **2006,** *33, L01602*.

35. Gleason, K. L., et al., A Revised U. S. CLimate Extremes Index. *J. Climate* **2008,** *21*, 2124-2137.

36. Stevenson, F. J., *Humus Chemistry. Genesis, Composition, Reactions*. 2nd ed.; Wiley: New York, 1994.

37. Wershaw, R. L., Membrane-micelle model for humus in soils and sediments and its relation to humification. Survey, U. S. G., Ed. Water-Supply Paper 2410, 1994; p 48.

38. Piccolo, A., The supramolecular structure of humic substances. *Soil Sci.* **2001,** *166*, 810-832.

39. Chilom, G., Baglieri, A., Johnson-Edler, C. A.,Rice, J. A., Hierarchical self-assembling properties of natural orgainc matter's components. *Org. Geochem* **2013,** *57*, 119-126.

40. Israelachvili, J. N., *Intermolecular and Surface Forces*. 2nd ed.; Academic Press: London, 1994.

41. Wershaw, R. L., Pickney, D. J., The fractionation of humic acids from natural water systems. *U.S. Geol. Survey Jour. research* **1973a,** *1* (3), 361-366.

42. Wershaw, R. L., Pickney, D. J., Determination of the association and diassociation of humic acid fractions by snall angle x-ray scattering. *U.S. Geol. Survey Jour. research* **1973b,** *1* (6), 701-709.

43. Wershaw, R. L., Chemical Structure of Humic Acids-Part 1. A Generalized Structural Model. *J. Research U.S. Geol. Survey* **1977,** *5* (5), 565-569.

44. Wershaw, R. L., A new model for humic materials and their interactions with hydrophobic chemicals in soil-water and sediment-water systems. *J. Contam. Hydrol.* **1986,** *1*, 29-45.

45. Wershaw, R. L., Model for humus in soils and sediments. *Environ. Sci. Technol.* **1993,** *27*, 814-816.

46. Tanford, C., *The Hydrophobic Effect: Formation of Micelles and Biological Membranes*. Wiley: New York, 1980.

47. Wershaw, R. L., Molecular Aggregation of Humic Substances. *Soil Sci.* **1999,** *164* (11), 803-813.

48. Morra, M. J. e. a., Fluorescence Quenching and Polarization Studies of Naphthalene and 1-Naphthol Interaction with Humic acid. *Soil Sci. Soc. Am. J.* **1990,** *54* (5), 1283-1289.

49. Aochi, Y. O. F., W. J., Role of Microstructural Properties in the Time-Dependent Sorption/Desorption Behavior of 1,2-Dichloromethane on Humic Substances. *Environ. Sci. Technol.* **1997,** *31* (9), 2520-2526.

50. Chien, Y.-Y., Kim, E.-G., Bleam, W. F., Paramagnetic Relaxation of Atrazine Solubilized by Humic Micellular Solution. *Environ. Sci. Technol.* **1997,** *31* (11), 3204-3208.

51. Kohl, S. D., Toscano, P.J., Hou, W., Rice, J.A., Soild State 19F NMR Investigation of Hexafluorobenzene Sorption to Soil Organic Matter. *Environ. Sci. Technol.* **2000,** *34* (1), 204-210.

52. Piccolo, A., Conte, P., Scheunert, I, Paci, M., Atrazine interactions with soil humic substances of different molecular structure. *J. Environ. Qual.* **1998,** *27*, 1324-1333.

53. Hu, W.-G., Moa, J.,Xing, B., Rohr, K.S., Poly(methylene) Crystallites in Humic Substances Detected by Nuclear Magnetic Resonance. *Environ. Sci. Technol.* **2000,** *43* (3), 530-534.

54. Witten, T., Structured fluids. *Physics Today* **1990,** *43* (7), 21-28.

55. Leibler, S., Of micelles and membranes. *Nature* **1990,** *348*, 586-587.

56. Fendler, J. H., Membrane memetic chemistry. *Chem. Eng. News* **1984,** *62* (1), 25-38.

57. Guetzloff, T. F., Rice, J. A., Does humic acid form a micelle? *Sci. Total Environ.* **1994,** *152*, 31-35.

58. Mazer, N. A., et al., Micellization, solubilization and microemulsion in aqueous biliary lipid sisyems. In *Solution behavior of surfactants - Theoretical and applied aspects*, Mittal, K. L. a. F., . E. J., Ed. Plenum Publishing: New York, 1982; Vol. 1, pp 595-610.

59. Small, D. M., The physical chemistry of cholanic acid. In *The bile acids-Chemistry, physiology, and metabolism*, Nair, P. P. a. K., D., Ed. Plenum Press: New York, 1971; Vol. 1, pp 49-356.

60. Rees, D. A., Welsh, E.J., Secondary and tertiary structure of polysaccarides in solutions and gels. *Angewandte Chemie International Edition in English* **1977,** *16*, 214-224.

61. Benoit, R. E., Starkey, R.L.,Basaraba, J., Effect of purified plan tannin on the decomposition of some organic compounds and plant materials. *Soil Sci.* **1968,** *105*, 153-158.

62. McManus, J. P., David, K.G.,Lilley, T.H., Haslam, E., The association of proteins with polyphenols. *Journal of the Chemical Society Chemical Communications* **1981,** (7), 309-311.

63. Hatcher, P. G., Faulon, J.-P., Wenzel, K.A., Cody, G.D., A structural model for lignin-derived vitrinite from high volatile bituminous coal (coalified wood). *Energy Fuels* **1992,** *6*, 813-820.

64. P.G, H., Dipolar dephasing 13C NMR studies of decomposed wood coalified xylem tissue: defunctioanlization of lignin structural units during coalification. *Energy Fuels* **1988,** *2*, 48-58.

65. Alexander, R., Kralert, P.G., Kinetics and mechanism of the thermal decpomposition of esters in sediments. *Org. Geochem* **1992,** *19*, 133-140.

66. Speight, J. G., *The chemistry and technology of petroleum*. Marcel Dekker: New York, 1980.

67. Speight, J. G., *Fuel Science and Technology Handbook*. Marcel Dekker: New Yok, 1990.

68. Yen, T. F., The role of asphaltenes in heavy crude and tar sands. In *The Future of Heavy Crude and Tar Sands*, Meyer, R. F., Steele, C.T, Ed. Mcgraw-Hill: New York, 1980; pp 174-197.

69. Sheu, E. Y., Self-Association of Asphaltenes: Structure and Molecular Packing. In *Structures and Dynamics of Asphaltenes*, Mullins, O. C., and Sheu, E.Y., Ed. Plenum Press: New York, 1998.

70. Mullins, O. C., The Modified Yen Model. *Energy Fuels* **2010,** *24*, 2179-2207.

71. Mullins, O. C., et al., Advances in Asphaltene Science and the Yen-Mullins Model. *Energy Fuels* **2012,** *26* (7), 3986-4003.

72. Dickie, J. P., Yen, T.F., Macrostructures of asphaltic fractions by various instrumental methods. *Anal. Chem.* **1967,** *39*, 1847-1852.

73. Yen, T. F., Asphaltic Materials. In *Encyclopedia of Polymer Science and Engineering*, 2nd ed.; Mark, H. S., Bikales, N.M.,Overberger, C.G., Menges, G., Ed. John Wiley and Sons: New York, 1989; pp 1-10.

74. International Humic Substances Society. http://www.humicsubstances.org/sources.html (accessed 9.24.15).

75. Thorn, K. A., Folan, Daniel W., MacCarthy, Patrick (accessed March 12, 2014).

76. International Humic Substances Society. www.humicsubstances.org (accessed March 12, 2014).

77. Chilom, G., Rice, J. A., Structural Organization of Humic Acid in the Solid State. *Langmuir* **2009,** *25* (16), 9012-9015.

78. Hawlicka, E., Self-Diffusion in multicomponent liquid systems. *Chem. Soc. Rev.* **1995,** *34*, 13743-13750.

79. Marshall, A. G., *Biophysical Chemistry: Principles, Techniques, and Applications*. Wiley: New York, NY, 1978.

80. Price, W. S., Pulsed-field gradient nuclear magnetic resonance as a tool for studying translational diffusion: Part 1 Basic theory. *Concepts in Magnetic Resonance* **1997,** *9* (5), 299-336.

81. Schnitzer, M., The methylation of humic substances. *Soil Sci.* **1974,** *117* (2), 94-102.

82. Kerssebaum, R., Salnikov, G, DOSY and Diffusion by NMR. Bruker BioSpin GmbH: Rheinstetten, Germany, 2002-2006; Vol. 2.0.

83. Spallation Neutron Source. http://neutrons.ornl.gov/sns (accessed 1.5.16).

84. Lujan Center at LANSCE. http://lansce.lanl.gov/lujan/index.shtml.

85. Hayter, J. B. P., J., Determination of Micelle Structure by Neutron Small-Angle Scattering. *Colloid Polym. Sci.* **1983,** *261*, 1022-1030.

86. Kotlarchyk, M. C., S.H., Analysis of Small-Angle Neutron Scattering Spectra from Polydisperse Interacting Colloids. *J. Chem. Phys.* **1983,** *79*, 2461-2469.

87. Hiemenz, P. C., *Principle of Colloid and Surface Chemistry*. Dekker: New York, 1977.

88. Chilom, G., Khalaf, M. R., Rice, J. A., Investigating the reassembly of self-assembled humic acid structures. 2016. Unpublished work.

89. Mao, J. D., Hu, W.G.,Schmidt-Rohr, K., Davies, G., Ghabbour, E.A., Xing, B.,, Quantitative characterization of humic substances by solid-state carbon-13 nuclear magnetic resonance. *Soil Science Society of America Journal* **2000,** *64*, 873-884.

90. Khalaf, M. M. R., Chilom, G., Rice, J. A. , Comparison of the effects of self-assembly and chemical composition on humic acid mineralization. *Soil Biol. & Biochem* **2014,** *73*, 96-105.

91. Dixon, A. M. L., C. K., Modified Pulsed-Field Gradient NMR Experiemnts for Improved Selectivity in the Measurement of Diffusion Coefficients in Complex Mixtures: Application to the Analysis of the Suwannee river Fulvic Acid. *Anal. Chem.* **1997,** *69*, 2122-2128.

92. Orfi, L., Lin, M., Larive, C.K., Measurement of SDS Micelle-Peptide Association Using 1H NMR Chemical Shift Analysis and Pulsed Field Gradient NMR Spectroscopy_Orfi 1998. *Anal. Chem.* **1998`,** *70*, 1339-1345.

93. Norinaga, K. W., V. J.; Takasugi, S.; Iino, M.; Matsukawa, S., Measurement of Self-Diffusion Coefficient of Asphaltene in Pyridine by Pulsed Field Gradient Spin-Echo 1H NMR. *Energy & Fuels* **2001,** *15*, 1317-1318.

94. Moon, J., Kim, S. H., Cho, J, Characterizations of natural organic matter as nano particle using flow field-flow fractionation. *Colliods and Surfaces A: Physicochem. Eng. Aspects* **2006,** *287*, 232-236.

95. Reid, P. M. e. a., Aggregation of humic substances in aqueous media as determined by light-scattering methods. *Soil Sci.* **1991,** *42*, 259-70.

96. Lead, J. R. W., K. J.;Balnois, E.; Cutak, B. J.; Larive, C.K.; Assemi, S.; Beckett, R., Determination of Diffusion Coefficients of Humic Substances by Fluorescence Correlation Spectroscopy: Role of Solution Conditions. *Environ. Sci. Technol.* **2000,** *34*, 3508-3513.

97. Simpson, A. J., Kingery, W. L., Hayes, M. H., Spraul, M., Humpfer, E., Dvortsak, P., Kerssbaum, R., Godejohann, M., Hofmann, M., Molecular structures and associations of humic substances in the terrestrial environment. *Naturwissenschaften* **2002,** *89* (2), 84-88.

98. Smejkalova, D., Piccolo, A., Aggregation and Disaggregation of Humic Supramolecular Assemblies by NMR Diffusion Ordered Spectroscopy (DOSY-NMR). *Environ. Sci. Technol.* **2008,** *42* (3), 699-706.

99. Simpson, A. J. e. a., Separation of Structural Components in Soil Organic Matter by Diffusion Ordered Spectroscopy. *Environ. Sci. Technol.* **2001,** *35* (22), 4421-25.

100. Lam, B. S., A. J., Direct 1H NMR spectroscopy of dissolved organic matter in natural waters. *Analyst* **2008,** *133*, 263-269.

101. Provencher, S. W., A Constrained Regularization Method For Inverting Data Represented by Linear Algebraic or Integral Equations. *Comput. Phys. Comm.* **1982a,** *27*, 213-227.

102. Provencher, S. W., CONTIN: A general Purpose Constrained Regularization Program for Inverting Noisy Linear Algebraic and Integral Equations. *Comput. Phys. Comm.* **1982b,** *27*, 229-242.

103. Morris, K. F., Cutak, B. J., Dixon, A. M., Larive, C. K., Analysis of Diffusion Coefficient Distributions in Humic and Fulvic Acids by Means of Diffusion Ordered NMR Spectroscopy. *Anal. Chem.* **1999,** *71*, 5315-5321.

104. Presser, A., Hufner, A., Trimethylsilydiazomethan - A Mild and Efficient Reagent for the Methylation of Carboxylic acids and Alcohols in Natural Products. *Monatshefte fur Chemie* **2004,** *135*, 1015-1022.

105. Guinier, A. F., G., *Small-Angle scattering of X-rays*. John Wiley: New York, 1955.

106. Glatter, O. K., O., *Small-Angle X-Ray Scattering*. Academic Press: London, 1982.

107. Feigin, L. A. S., G. I., *Structure Analysis by Small-Angle X-ray and Neutron Scattering*. Plenum: New York, 1987.

108. Rice, J. A., Applications of Fractals in the Study of Humic Materials. In *Biophysical Chemistry of Fractal Structures in Environmental Systems*, Senesi, N., Wilkinson, K.J., Ed. John Wiley & Sons: 2008; Vol. 11.

109. Sivia, D. S., *Elementary Scattering Theory*. 1st ed.; Oxford University Press Inc: New York, 2011.

110. D'Aguanno, B. K., R., *Light Scattering. Principles and Development*. University Press: Oxford, 1996.

111. Ailawadi, N. K., Equilibrium theories of simple liquids. *Phys. Rev.* **1980,** *57* (4), 241-306.

112. Hansen, J. P. M., I. R., *Theory of simple liquids*. Academic Press: London, 1990.

113. Johnson-Edler, C. A. R., J. A., Pulsed-Field Gradient NMR Determination of the Diffusion Coefficients of Natural Organic Matter (NOM).

114. Mandelbrot, B. B., *The Gractal Geometry of Nature*. W. H. Freeman and Company: New York, 1977.

115. Sagan, H., *Space-Filling Curves*. Springer-Verlag: Berlin, 1994.

116. Schmidt, P., Use of Scattering to Determine the Fractal Dimension. In *The Fractal Approach to Heterogeneous Chemistry*, D., A., Ed. John Wiley & Sons, Ltd.: Chichester, 1989; pp 67-79.

117. Martin, J. E., Hurd, A.J., Scattering and Fractals. *J. Appl. Crystallogr.* **1987,** *20*, 61-78.

118. Rice, J. A., Lin, J.S., Fractal Nature of Humic Materials. *Environ. Sci. Technol.* **1993,** *27*, 413-414.

119. Senesi, N., Rizzi, F.R., Dellino, P., Aquafredda, P., Fractal Humic Acids in Suspensions at Various Concentrations, Ionic Strenghts, and pH Values. *Colliods Surf., A* **1997,** *127*, 57-68.

120. van Santen, R. A., Neurock, M., *Molecular Heterogeneous Catalysis: A Computational Approach*. Wiley-VCH: Weinheim, 2006.

121. Do, C.; Heller, W. T.; Stanley, C.; Gallmeier, F. X.; Doucet, M.; Smith, G., Understanding inelastically scattered neutrons from water on a time-of-flight small-angle neutron scattering (SANS) instrument. *Nuclear Instruments and Methods in Physics Research A* **2014,** *737*, 42-46.

122. Van Saarloos, W., On the Hydrodynamic Raduis of Fractal Aggregates. *Physica* **1987,** *147A*, 280-296.

123. Witten, T. A.; Sander, L. M., Diffusion-Limited Aggregation, A Kinetic Critical Phenomenon. *Phys. Rev. Lett.* **1981,** *47* (19), 1400-1403.

124. Meakin, P.; Stanley, H. E.; Coniglio, A.; Witten, T. A., Surfaces, interfaces, and screening of fractal structures. *Phys. Rev. A* **1985,** *32* (4), 2364-2369.

125. Barre, L., Simon, S., Palermo, T., Solution Properties of Asphaltenes. *Energy Fuels* **2008,** *21* (5), 2809-2815.

126. Gawrys, K. L., Blankenship, G.A., Kilpatrick., P.K., Solvent Entrainment in and Flocculation of Asphaltic Aggregates Probed by Small-Angle Neutron Scattering. *Langmuir* **2006,** *22* (10), 4487-4497.

127. King, S. M., Expoloring how Organic Matter Controls Structural Transformations in Natural Aquatic Nanocolloidal Dispersions. *Environ. Sci. Technol.* **2012,** *46*, 6959-6967.

128. Pranzas, P. K., et al., Charaterisation of Structure and Aggregation Processes of Aquatic Humic Substances using Small-Angle Scatteirng and X-ray Microscopy. *Anal. Bioanal. Chem.* **2003,** *376*, 618-625.

129. Osterberg, R., Mortensen, K., Fractal Dimension of Humic Acids; A Small Angle Neutron Scattering Study. *Eur. Biophys. J.* **1992,** *21*, 163-167.

130. Perdue, E. M., Acidic Functional Groups in Humic Substances. In *Humic Substances in the Soil, Sediment, and Water*, John Wiley: New York, 1985.